Tuning of Block Copolymer Membrane Morphology through Water Induced Phase Inversion Technique

Dissertation by

Poornima Madhavan

In Partial Fulfillment of the Requirements

For the degree of

Doctor of Philosophy

King Abdullah University of Science and Technology

Thuwal, Kingdom of Saudi Arabia

EXAMINATION COMMITTEE APPROVALS FORM

The dissertation of Poornima Madhavan is approved by the examination committee

Committee Chairperson: Professor Suzana. P. Nunes
Committee Members: Professor Joao Crespo, Professor Klaus-Viktor Peinemann, Professor Pascal Saikaly

ABSTRACT

Tuning of Block Copolymer Membrane Morphology through Water Induced Phase Inversion Technique

Poornima Madhavan

Isoporous membranes are attractive for the regulation and detection of transport at the molecular level. A well-defined asymmetric membranes from diblock copolymers with an ordered nanoporous membrane morphologies were fabricated by the combination of block copolymer self-assembly and non-solvent-induced phase separation (NIPS) technique. This is a straightforward and fast one step procedure to develop integrally anisotropic ("asymmetric") membranes having isoporous top selective layer. Membranes prepared via this method exhibit an anisotropic cross section with a thin separation layer supported from underneath a macroporous support. These membrane poses cylindrical pore structure with ordered nanopores across the entire membrane surfaces with pore size in the range from 20 to 40 nm. Tuning the pore morphology of the block copolymer membranes before and after fabrication are of great interest.

In this thesis, we first investigated the pore morphology tuning of asymmetric block copolymer membrane by complexing with small organic molecules. We found that the occurrence of hydrogen-bond formation between PS-b-P4VP block copolymer and –OH/ –COOH functionalized organic molecules significantly tunes the pore morphology of asymmetric nanoporous membranes. In addition, we studied the complexation behavior of ionic liquids with PS-b-P4VP block copolymer in solutions and investigated their effect on final membrane morphology during the non-solvent induced phase separation process. We found that non-protic ionic liquids facilitate the formation of hexagonal nanoporous block copolymer structure, while protic ionic liquids led to a lamella-structured membrane.

Secondly, we demonstrated the catalytic activity of the gold nanoparticle-enhanced hollow fiber membranes by the reduction of nitrophenol. Also, we systematically investigated the pore morphology of isoporous PS-b-P4VP using 3D imaging technique.

Thirdly, we developed well-distributed silver nanoparticles on the surface and pore walls of PS-b-P4VP block copolymer membranes and then investigated the biocidal activity of the silver nanoparticles grown membranes.

Finally, a novel photoresponsive nanostructured triblock copolymer membranes were developed by phase inversion technique. In addition, the photoresponsive behavior on irradiation with light and their membrane flux and retention properties were studied.

ACKNOWLEDGEMENTS

I wish to express my deep sense of gratitude to my Ph.D supervisor and mentor, Prof. Dr. Suzana Nunes, Professor and Associate Dean, BESE Division, KAUST for her inspiring and excellent guidance from the initiation of this work till the end, and constant support and encouragement during my difficult times. The liberty given by her to reach the goals, made me confident in my approach towards the tasks undertaken. I have been very fortunate to have her as my guide.

I would like to express my sincere thanks to Prof. Dr. Klaus Viktor Peinemann, Professor, CBE Division, KAUST for his constructive suggestions and technical advices during my Ph.D studies.

I would like thank to Prof. Pascal Saikaly, EnSE Division, and Prof. Klaus Viktor Peinemann, KAUST for being a Ph.D committee member.

I thank Dr. Ali Reza Behzad, Scientist and Dr. Rachid Sougrat, Scientist, Advanced Nanofabrication Imaging and Characterization core lab, KAUST for their help in microscopic measurements. I would like to thank Dr. Roland Hilke and Mr. Pradeep Neelakanda, AMPM center, for providing hollow fiber block copolymer membranes for my thesis work. Also, I thank Prof. Peiying Hong, EnSE Division, KAUST for her support in characterizing the membranes for antibacterial studies.

I express my special thanks to my co-workers and collaborators of Nanostructured Polymeric Membranes Laboratory, KAUST for their wonderful support and cooperation.

I could not have completed this work without the encouragement and support of my family and I take this opportunity to express my heartfelt thanks to them.

TABLE OF CONTENTS

LIST OF ABBREVIATIONS

PS-b-P4VP	Poly(styrene-b-4-vinylpyridine)
BCP	Block copolymer
DMF	Dimethylformamide
THF	Tetrahydrafuran
DIOX	1,4 dioxane
Ru	Rutin
TPA	Terephthallic acid
DHBA	Dihydroxybenzyl alcohol
AM	Anthracene Methanol
Tris	1,3,5-Tris(4'carboxy[1,1'-biphenyl]-4-yl) benzene
MA	Mellitic acid
ATR-FTIR	Attenuated total reflectance fourier transform infrared spectroscopy
AFM	Atomic force microscopy
FESEM	Field Emission scanning electron microscopy
TEM	Transmission electron microscopy
IL	Ionic liquid
[B3MIM][BF4]	1-Butyl-3-methylimidazolium tetrafluoroborate ([B3MIM][BF4])
[EMIM][BF4]	1-Ethyl-3-methyl imidazolium tetrafluoroborate
[B4MPy][BF4]	1-Butyl-4-methylpyridinium tetrafluoroborate
[B3MPy][TFMS]	N-Butyl-3-methylpyridinium trifluoromethanesulfonate
[IM][TFSI]	Imidazolium bistrifluoro methane sulphonimide ([IM][TFSI])
[HMIM][HSO4]	1-methylimidazolium bisulfate
PS-b-PAnMMA-b-PMMA	poly(styrene-b-anthracene methyl methacrylate-b-methylmethacrylate)
DMAc	Dimethyl acetamide
ACN	Acetonitrile

LIST OF FIGURES

LIST OF TABLES

CHAPTER-1

Introduction

Membrane technology is a useful tool in a variety of applications, such as food industry, health sector, energy storage and sustainable water treatment.[1-3] Millions of people die every year from water related diseases especially children due to the lack of access to clean water.[4] Hence providing clean water is an ultimate necessity which require improvements in the water filtration systems. Membranes consisting of thin porous polymer films are frequently used in such water filtration systems.[5] Classes of porous polymer membranes exist based on pore size or the diameter of the pore, and these have a range of molecular weight cut-offs (MWCOs). However, the use of membranes could be even extended, by overcoming a few drawbacks. One of them is the broad pore size distribution of most currently commercially available membranes. The current state-of-the-art membranes face commercially attractive separation problems, when it comes to new technically challenging areas. Advances in design and fabrication of nanoporous membranes are expected to open up new opportunities for the development of membrane technology. Ultimately this will improve the current state of filtration systems.[6-8] Most porous block copolymer membranes are suitable for the range of ultrafiltration (UF).[9,10] UF needs highly selective and permeable membranes with fouling resistance. Membranes made from block copolymers could fulfill all these requirements with incomparable porosity and narrow pore size distribution and chemical properties that can solve the problems of fouling and mechanical instability.

Well-defined asymmetric membranes prepared from polystyrene-*b*-poly (4-vinylpyridine) (PS-b-P4VP) diblock copolymers with an ordered nanoporous membrane morphologies have been reported by Nunes et al.[11] These type of isoporous (same pore size) membranes are attractive for the regulation and detection of transport at the molecular level. The isoporous membranes were obtained by the combination of block copolymer self-assembly and phase inversion or non-solvent-induced phase separation (NIPS). This is a straightforward and fast one step procedure to develop integrally anisotropic ("asymmetric") membranes having isoporous top selective layer. Membranes prepared via this method usually exhibit an anisotropic cross section with a thin separation layer supported from underneath a macroporous support. The block copolymer membranes prepared by phase inversion poses cylindrical pore structure with ordered nanopores across the entire membrane surfaces with pore size in the range from 20 to 40 nm. Block copolymer is the main component for the fabrication of isoporous membranes, since it has ability to self-assemble in solutions and produce a large diversity of morphologies in the bulk membranes. Here, we studied two types of block copolymer such as PS-b-P4VP diblock and poly(styrene-*b*-anthracene methyl methacrylate-b-methylmethacrylate) (PS-b-PAnMMA-b-PMMA) triblock copolymer for isoporous membrane formation by phase inversion.

In this dissertation, first we outline the background of membranes, asymmetric membrane by phase inversion, self-assembly of block copolymers and isoporous block copolymer membranes *via* phase inversion technique. Then the dissertation objectives are categorized in to five themes. Theme 1 describes the tailoring of PS-b-P4VP block copolymer membrane pore morphology by complexation with small organic molecules in the membrane casting solution. We investigated the effect on final membrane morphology by

addition of –OH/ –COOH functionalized small organic molecules to the PS-b-P4VP block copolymer during phase inversion process. Similarly (Theme 2), we studied the effect of ionic liquids (ILs) as co-solvent in the membrane casting solution and their effect on final asymmetric membrane morphology. Protic and non protic ionic liquids were employed to study the interaction of PS-b-P4VP block copolymer with ionic liquids and final membrane morphology during the phase inversion process. Theme 3 describes the complexation behavior of isoporous PS-b-P4VP block copolymer membrane with gold metal salts. Gold complexed isoporous membranes were investigated for catalytic application. Also the PS-b-P4VP isoporous membrane has ability to complex with silver metal ions. Theme 4 describes the complexation behavior of PS-b-P4VP membrane with silver metal and investigates the antibacterial properties of isoporous metal membranes. In Theme 5 we utilized PS-b-PAnMMA-b-PMMA block copolymer for isoporous membrane formation by phase inversion technique. We studied the various morphologies obtained by the PS-b-PAnMMA-b-PMMA block copolymer during the phase inversion process and investigated their light responsive behavior.

1.1 Background

1.1.1 Definition of a membrane:

A synthetic membrane is a selective barrier, which separates two phases and restricts the transport of various chemical species in a rather specific manner.[3]

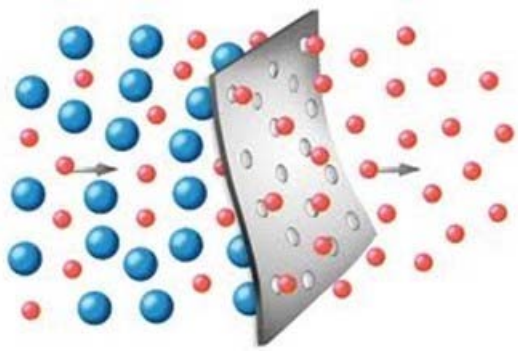

Figure 1. 1 Membrane separation process

1.1.2 Classification of membranes

Synthetic membranes are categorized into organic (liquid or polymer) and inorganic (metal or ceramic). In addition, membranes were also classified based on the morphology such as dense, porous and composite membranes. Porous membranes may be further classified into symmetric and asymmetric membranes. Symmetric membranes by definition are of uniform structure produced by either sintering or stretching, casting, phase inversion and etching or extrusion. The thickness of the symmetric membranes ranges from 10 to 200 μm. In asymmetric membranes, the top is either porous or dense skin with a thickness ranges from 0.1 to 1.0 μm supported by a macroporous sublayer with a thickness range from 50 to 150 μm. However, in composite membranes the top layer and the porous support layers are two different polymeric materials.[1,2,12]

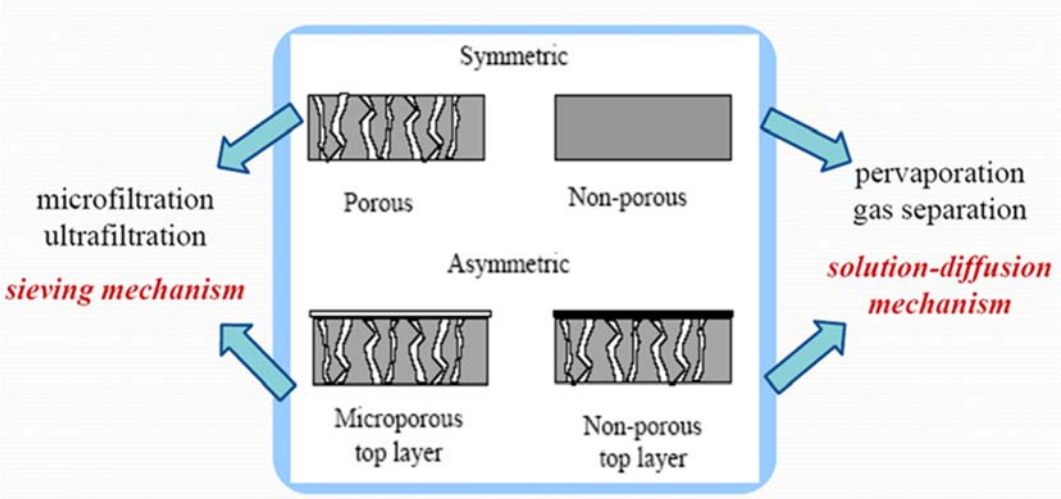

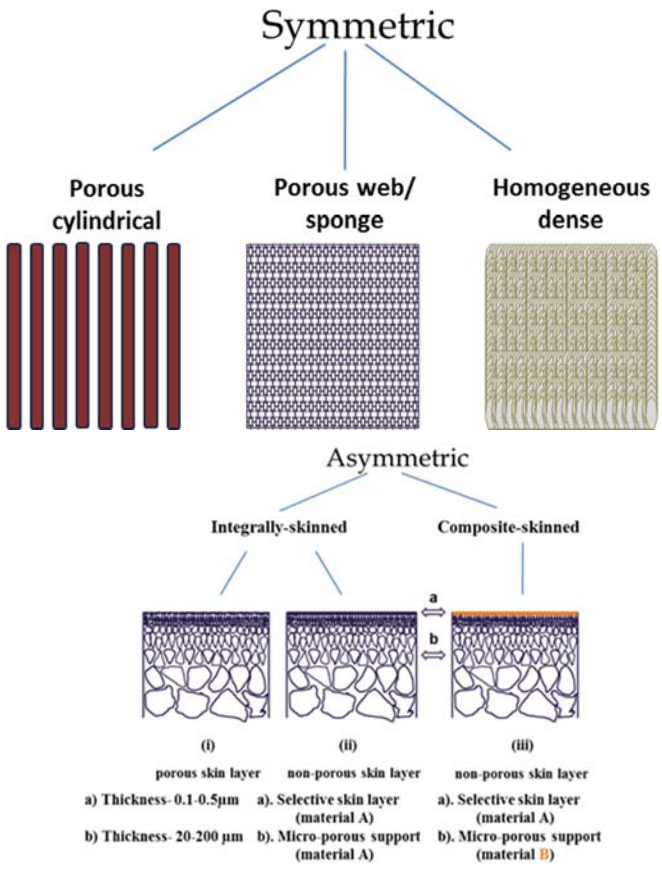

Figure 1.2 Types of polymeric membranes

1.1.3 Asymmetric membranes

Asymmetric membranes were first developed by Loeb et al., through non-solvent-induced phase separation (NIPS).[13] The introduction of asymmetric membranes by this method for reverse osmosis was a breakthrough in the field of membrane technology. Phase separation is employed to transform a polymer in a controlled manner from a liquid dispersion to a solid film.[14] Asymmetric membranes can be prepared by either dry or wet phase inversion process. The thin dense layer in the asymmetric membrane acts as a barrier against some undesired components while the porous support provides the desired mechanical stability thereby contributing to the increase of flux. Many asymmetric membranes have been developed by phase inversion process. Phase inversion is now a traditional method to obtain the asymmetric membranes. It is one of the ready techniques available to produce different kinds of morphologies. During the phase inversion process a polymer solution is transferred from a liquid to solid film. This phase separation is induced by temperature change (thermal precipitation) or by immersing the polymeric solution in a non-solvent bath, which is known as wet process (immersion precipitation) or by exposing the polymeric solution to atmosphere, which is known as dry process. Many commercially available polymer membranes are prepared by the immersion precipitation method (Figure 1.4).[12,14,15]

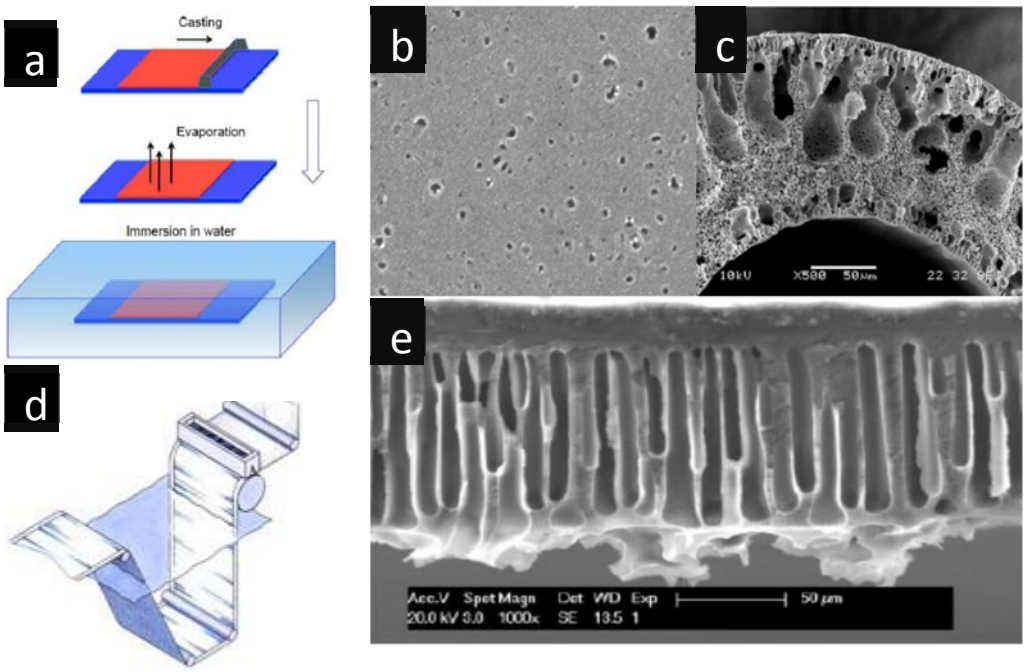

Figure 1.3 (a) Non solvent induced phase inversion process; (b) top surface of polysulfone membrane; (c) crossection of hollow fiber; (d) membrane fabricating machine; (e) crossection of polysulfone membrane through phase inversion.

In the phase inversion method, initially a polymer was dissolved in suitable solvent which are miscible with water. Then the polymer solution was cast on a support and then immersed in a coagulation bath containing a non-solvent mainly water. The solution cast on support precipitate due to the exchange of solvent in the polymer solution and nonsolvent from the coagulation bath. During the process, the polymer rich phase creates porous matrix and the polymer poor phase forms pores. The key factors that influence membrane morphology during the phase inversion process are

- choice of polymer;
- choice of solvent and nonsolvent;
- composition of casting solution;

- composition of coagulation bath;
- evaporation time,
- temperature of cast solution and coagulation bath

The membrane morphology can be modified from an open porous structure to a dense non-porous membrane by varying one or more of these parameters. Through phase inversion method membranes can be made for different applications from microfiltration to reverse osmosis.

Table 1.1 Polymers used to prepare phase inversion membranes[12]

S. No	Polymers	Membrane applications
1	Polysulfone	MF, UF
2	Polyethersulfone	MF, UF
3	Polyvinylidenefluoride	MF, UF
4	Polyacrylonitrile	MF, UF
5	Cellulose acetate	MF, UF, NF, RO, GS
6	Polyimide	UF, GS
7	Polyamide	MF, UF NF, RO
8	Polyphenylene oxide	GS

Microfiltration (MF), ultrafiltration (UF), nanofiltration (NF), reverse osmosis (RO), gas separation (GS).

Many polymers are frequently used for membrane preparation by the phase inversion method. In particular, polymers such as polyether-sulfone and polysulfone are used as MF, UF membranes. Also these membranes were used as supports in the composite membranes fabrication for NF, RO and GS. Polymers such as polyether sulfone, polysulfone and cellulose acetate, polyimide polymers are robust and possesses very good film forming properties. Apart from these two polymers many other polymers are also used for

membrane fabrication by phase inversion method, which are listed in Table 1.1. So far homopolymers (Table 1.1) were mainly used for membrane preparation by phase inversion method. Membranes produced by this technique has typical tradeoff between flux and rejection, i.e., either highly porous (high flux with low solute rejections) or low porous (low flux with high solute rejections). However, membranes obtained by these techniques are in use for various applications from microfiltration to reverse osmosis or gas separations.

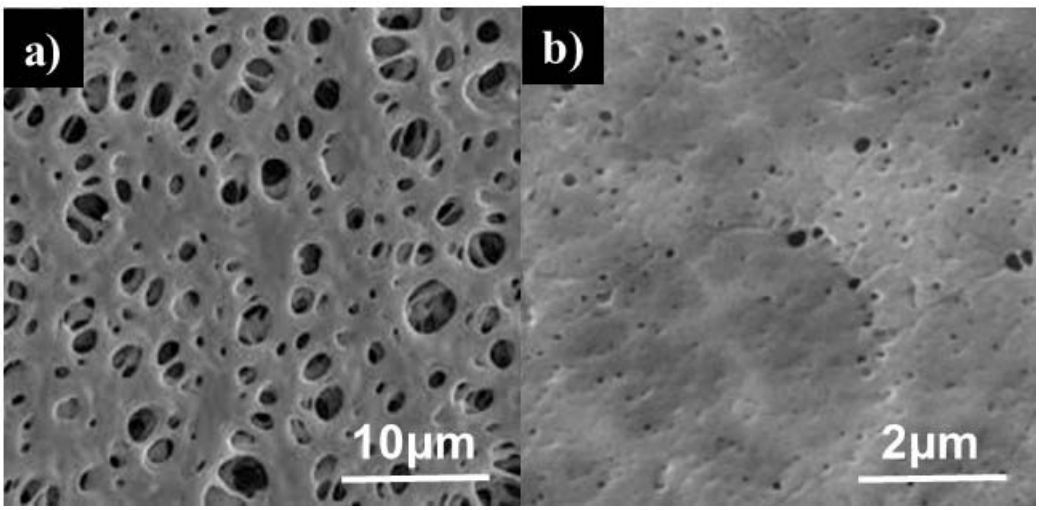

Figure 1.4 Polythersulfone (a) MF and (b) UF membrane

To obtain a sharp selectivity with enhanced flux, membranes with the same pore size and shape (isoporous) are of great interest for various applications, from being barriers for selective transport and separation of chemical/biological species. Recently, block copolymers (BCPs) have risen as a promising precursor for making isoporous membranes.[16-19] There are various strategies involved in developing isoporous membranes using block copolymers. In this dissertation, we focus on isoporous membranes developed by the combination of self-assembly of block copolymer and phase inversion method.

1.1.4 Self-assembly of block copolymers

Block copolymer consists of two or more different polymer blocks linked together with different physical or chemical properties. The blocks are chemically connected to each other in a fashion AAAA-BBBB-AAAA (A and B are different types of monomers). block copolymers are classified based on the arrangements and number of blocks connected to the backbone. For example block copolymers with two, three and more blocks are called as di-, tri- and multi- block copolymers.

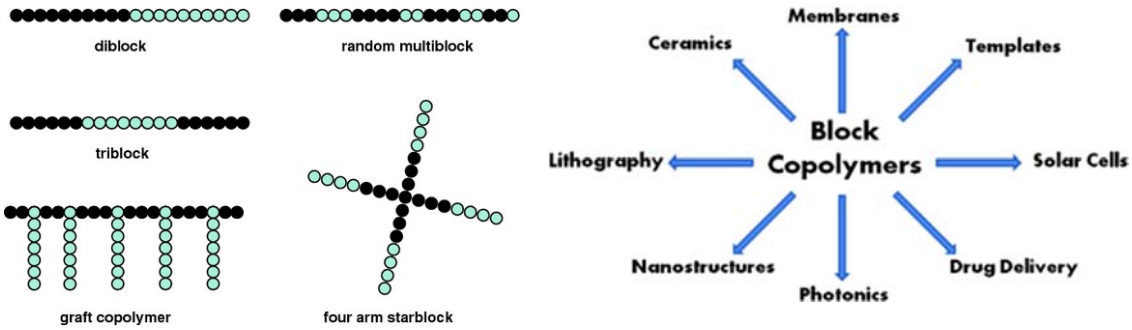

Figure 1.5 Types of block copolymers and their applications

Classification based on the arrangement includes the linear, end to end arrangement and the star arrangement in which one polymer is the base for multiple branches. As can be seen from the flow chart (Figure 1.5) block copolymers are versatile materials for preparing variety of things, in general for membrane development. The main advantage in preparing membranes with block copolymers is we can tune the structures of the membrane. This tuning of the structures is due to the self-assembly of the block copolymers. Block copolymers self-assemble into distinct structures due to the incompatibility between the two blocks. The competition between enthalpy and entropy leads to the microphase separation. Due to the microphase separation, block copolymer can display different nanoscale morphology, such as cylinders, spheres, lamellae and bicontinuous gyroid

phases. Self-assembly of block copolymers in bulk and solutions has been extensively studied for the last few decades.[20-22] In solution block copolymer can self-assemble and produce multiple morphologies.

1.1.5 Block copolymers in bulk

Self- assembly of block copolymers is a very broad and attractive area. For the past decades, block copolymer self-assembly in bulk has been extensively studied.[20-22] Self - assembly of block copolymers is a model example of bottom-up system. Block copolymers with two or more different chains of repeating segments linked together, segregate into distinct structures due to the incompatibility between the blocks. The competition between enthalpy and entropy leads to the microphase separation. The nature and shape of the microphase separated domain depends on the total degree of polymerization (N_A+N_B), the composition ($f=N_A/N$) and the Flory Huggins interaction parameter χAB (which is a measure of the incompatibility between the two blocks). Typically the dimensions of the segregated domains can be tuned from 5 to more than 100 nm by changing the molecular weight of the polymer. The χ parameter specifies the degree of incompatibility between A and B blocks, which drives the phase separation. With increasing f_A at a fixed χN above the ODT, the order to disorder transition starts from closely packed spheres (CPS), transforming through body centered cubic spheres(S), hexagonally packed cylinders (C) and bicontinous gyroids(G) to lamellae(L). As shown in the phase diagram (Figure 1.6) the blocks volume fractions and immiscibility control the morphology. The block copolymer morphologies can also be tuned through the addition of a selective solvent, in which the amphiphilic block copolymers form various micellar structures with one block dissolved and the other associated in a core protected interaction with the solvent. A large variety of

morphology has been reported in the literature.[23-25] A challenge is to stabilize the most interesting morphologies and make use of their characteristics for membrane manufacture. For that additives like complexing agents can be a successful approach. This is one of the objective of this thesis.

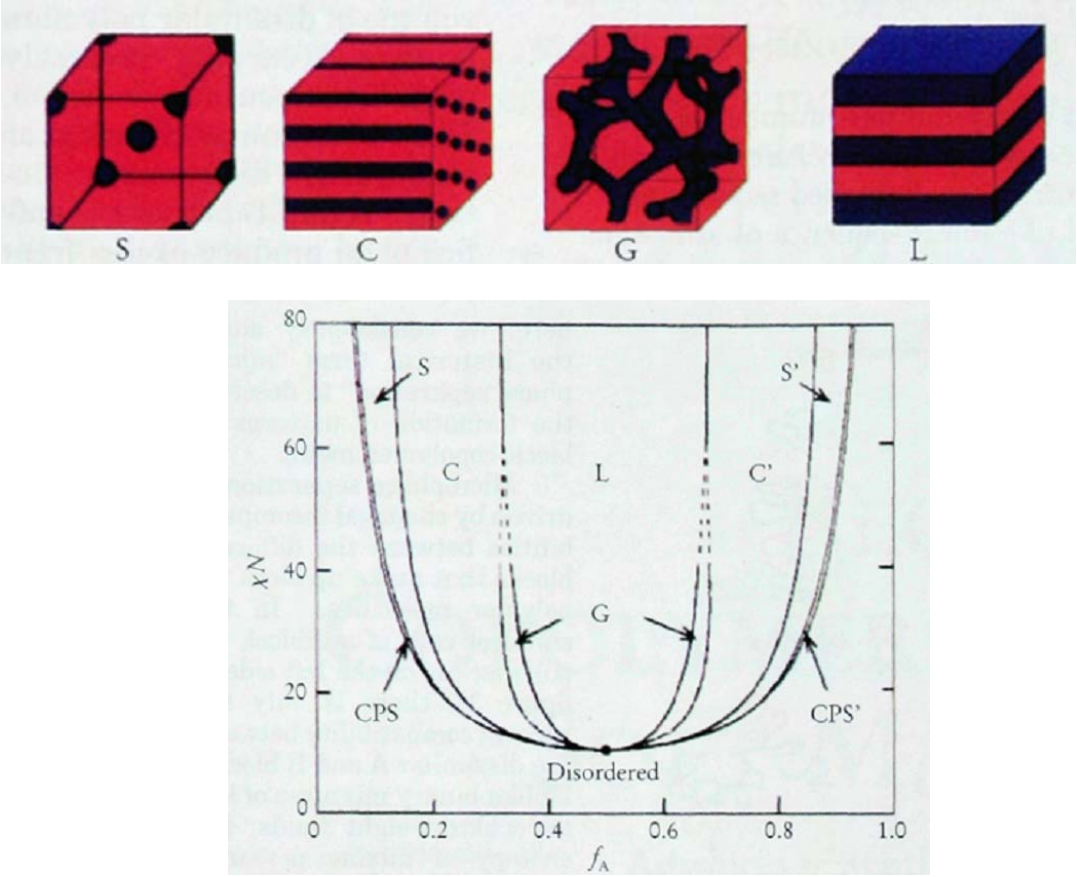

Figure 1.6 Morphologies of AB type block copolymerand phase diagram predicted by SCMF theory. Reprinted (adapted) with permission from (Bates et al. Physics Today, 1999, AIP Publishing LLC)[21]

1.1.6 Mechanism of morphological transitions

As discussed earlier the self-assembly in block copolymers is due to the competition between enthalpy and entropy of the two blocks, ie., the interfacial energy between the two

blocks(enthalpy contribution) and chain stretching (entropic contribution). As microphase separation takes place the two blocks separate from each other in such a way to minimize the interfacial area in order to lower the total interfacial energy.

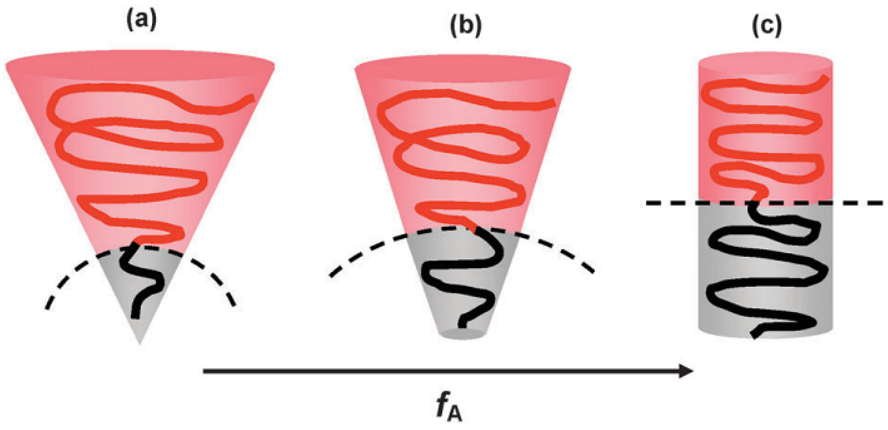

Figure 1.7 Schematic illustration of possible polymer chain conformations of AB diblocks

The mechanism which is followed for the morphological transitions is the well-known cone-column mechanism (Figure 1.7).[26] With two blocks the system will try to take the morphology which has the lowest interfacial area and increased configurational entropy and which is also energetically favorable. For example when the volume fraction of A block is smaller than the B block the system will prefer to take spherical conformation, with the B block in the form of coronas. As the volume fraction of one of the block increases it tends to take the structure which is energetically favorable hence the corona volume fraction decreases and less curved interfaces are formed thus leading to morphological transitions from sphere to cylinders to lamellae.

1.1.7 Block copolymers in solution

The presence of solvent in a block copolymer system increases the level of complexity compared to the bulk systems. In this case the χ parameter for the solvent S (good solvent

for both the blocks) and non-solvent N (for one of the block) should also be considered in addition to the χ parameter of the individual A and B blocks. The larger the number of parameters in the system, the more complex is the self-assembly process in this case.

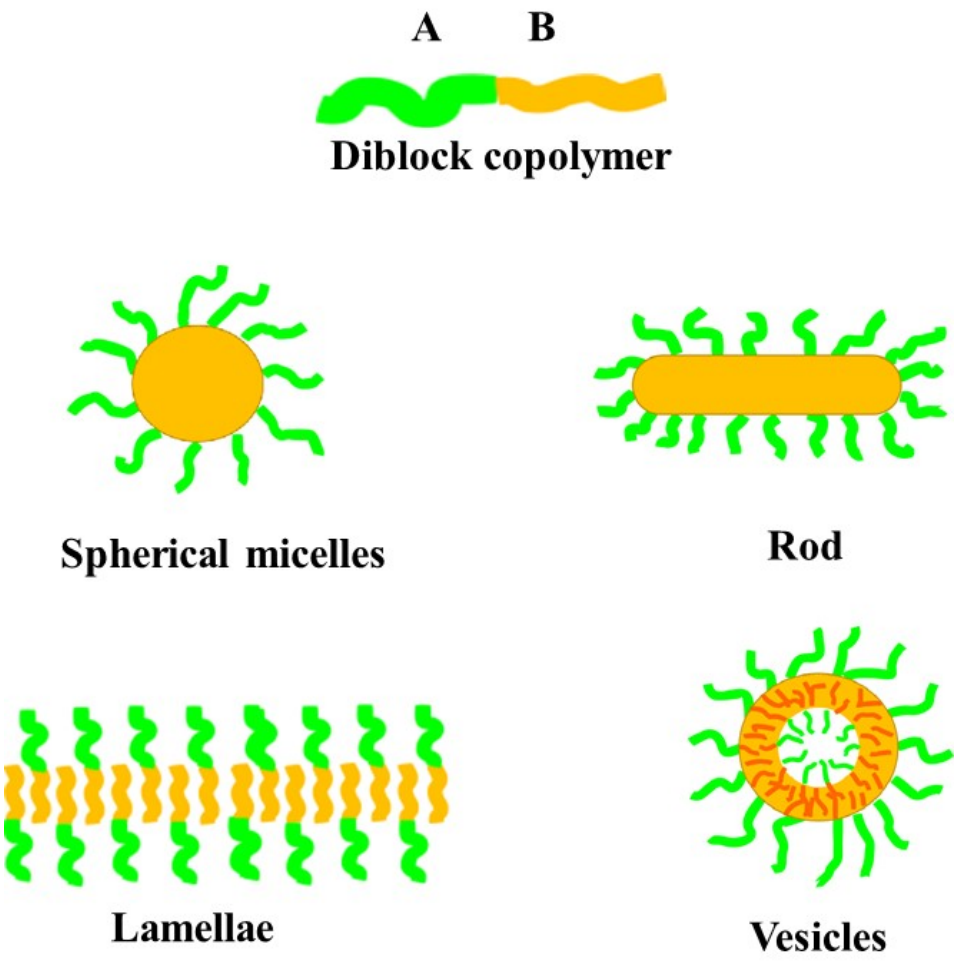

Figure 1.8 Various examples of crew cut morphologies ranging from spheres, to rods, small lamellae and vesicles.

The amphiphilic block copolymers are the mainly studied system in the recent years eg. PS-b-PAA or PS-b-PEO or PS-b-P4VP. In the mid 90's Eisenberg *et al.*[20] investigated the solution behavior of highly asymmetric amphiphilic diblock copolymers containing a long hydrophobic block (PS) and a short hydrophilic one (PAA, PEO) and forming supramolecular assemblies in water.[28] These systems generate various morphologies

depending on the length of each blocks. In cases where the hydrophobic blocks are much larger than the hydrophilic segments, the coronas are much smaller and lead to the formation of aggregates termed as crew-cut micelles. In contrast aggregates or spherical micelles in which the coronas are much longer it is termed as "star-like" aggregates. Interestingly different kinds of morphologies were observed for crew-cut aggregates as shown in Figure1.8. The variety of possible morphologies is from the influence of various factors. The main reason is the surface tension between the core and the solvent. The other two reasons are the stretching degree of the chains in the core and the repulsive interaction between the corona chains. For eg. In the case of PS-b-PEO a morphological transition from spherical to non-spherical occurs in water when the block length of PEO decreases. Hence when the soluble block (PEO in this case) is shorter the radius of the spherical core is increased even for a constant PS block. In that case the mutual repulsion is decreased between the PEO corona chains and finally the curvature of the core shell interface as well. The degree of stretching of PS core depends on the radius of the core. The radius of the core cannot increase dramatically as the entropy continuously decreases with the stretching of PS blocks. When this entropy is beyond a critical value, the system will not be stable anymore and hence it tends to adopt a different configuration or morphology. Hence different morphologies are observed in solutions due to the three main factors mentioned above.

1.1.8 Isoporous block copolymer membrane *via* phase inversion method

The block copolymer based strategies offers an affordable and flexible solution to prepare isoporous membranes with pore sizes down to sub-20 nm. Many innovative approaches based on block copolymers have been proposed to prepare nanoporous films by preferential

etching of one of the block domains with multiple manufacturing steps.[29-36] However to manufacture membranes in technical scale requires simple steps and high reproducibility. The current methods used to generate pores on the block copolymer films are selective removal of sacrificial domains or the extraction of an added homopolymer additive. Examples are the UV-etching of PMMA in thin-films of PEO-b-PMMA-b-PS block terpolymers, or by selective removal of PMMA homopolymer additive during the spin-casting of PS-b-PMMA diblock copolymer thin-films. In the previous case, the labile PMMA blocks are chemically etched away by irradiation of short-wavelength UV light plus a rinse with acetic acid or alkaline-catalyzed hydrolysis, respectively. These chemical etching processes carried out in solvents under harsh conditions are usually tedious and poor scalability for large scale applications. Since, these methods require multiple and complicated steps to develop highly ordered nanoporous membranes. As an alternative to destructive chemical routes to convert domains of the minor blocks into void spaces, Peinemann et al., proposed and demonstrated a straight forward and one step method for the preparation of nanoporous membrane using block copolymers.[37] Isoporous membranes were developed by combining self-assembly of block copolymers and phase inversion method. The nanopores are formed during phase inversion process, i.e., immersion of a concentrated block copolymer solution in a water bath (non-solvent). A well known non-ionic amphiphilic PS-b-P4VP block copolymer was first used to develop the isoporous membrane by this method and has been further explored by our group.[38-40] This straightforward and fast one step procedure can control both membrane morphology and barrier structure by tuning wide range of parameters. Membranes prepared via this technique usually exhibit an anisotropic cross section with a thin separation layer supported

from underneath by a macroporous support. Such asymmetric structures find their applications in pressure-driven processes like ultrafiltration, nanofiltration, or reverse osmosis. Figure 1.9 shows a well-defined asymmetric membranes from PS-b-P4VP diblock copolymers with a hexagonally arranged nanopores on the top layer. The isoporous morphology with pore diameter in the range from 20 to 40 nm and membrane poses 100 nm thin isoporous nanochannels underneath the spongy microporous support layer.

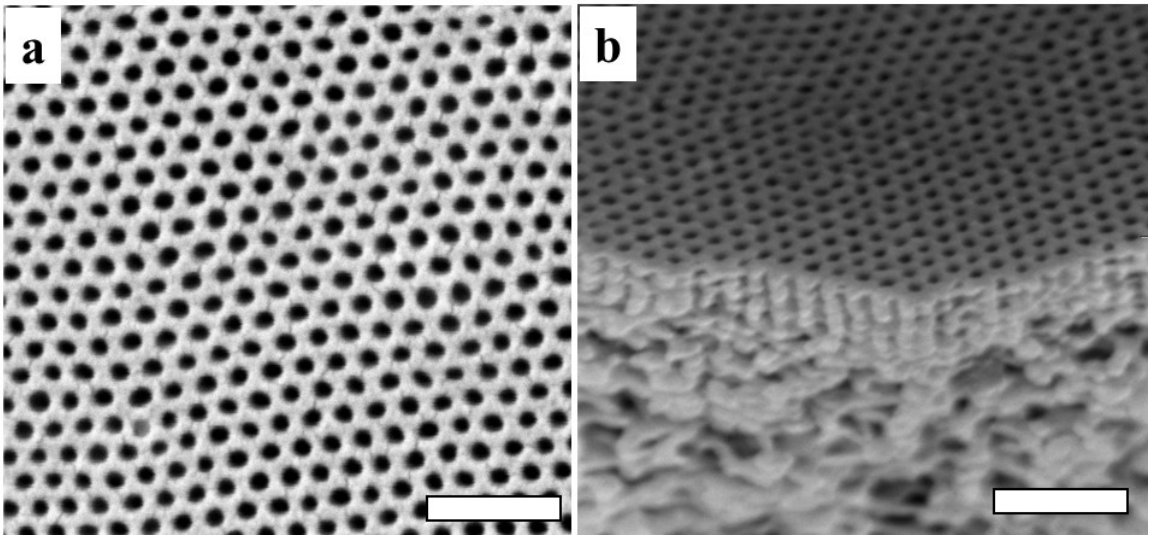

Figure 1.9 SEM micrographs of asymmetric membranes prepared from PS-b-P4VP diblock copolymers; (a) top separation layer (b) cross section with top view, the scale bar corresponds to 200nm(a) and 500 nm (b).[Peinemann et al, Nat. Mat. 2007][37]

Figure1.10 shows the asymmetric membrane formation by water induced phase inversion method. In the first step block copolymer solutions were dissolved in dimethylformamide and tetrahedrafuran solvent mixture for 24 h. After that the polymer soultions were cast on the glass plate and evaporated for 10 s to attain equilibrium morphology. Finally, the evaporated solution was immersed in water bath to generate pores and simultaneously freeze the polymer soltuion (phase inversion process) to form solid film.

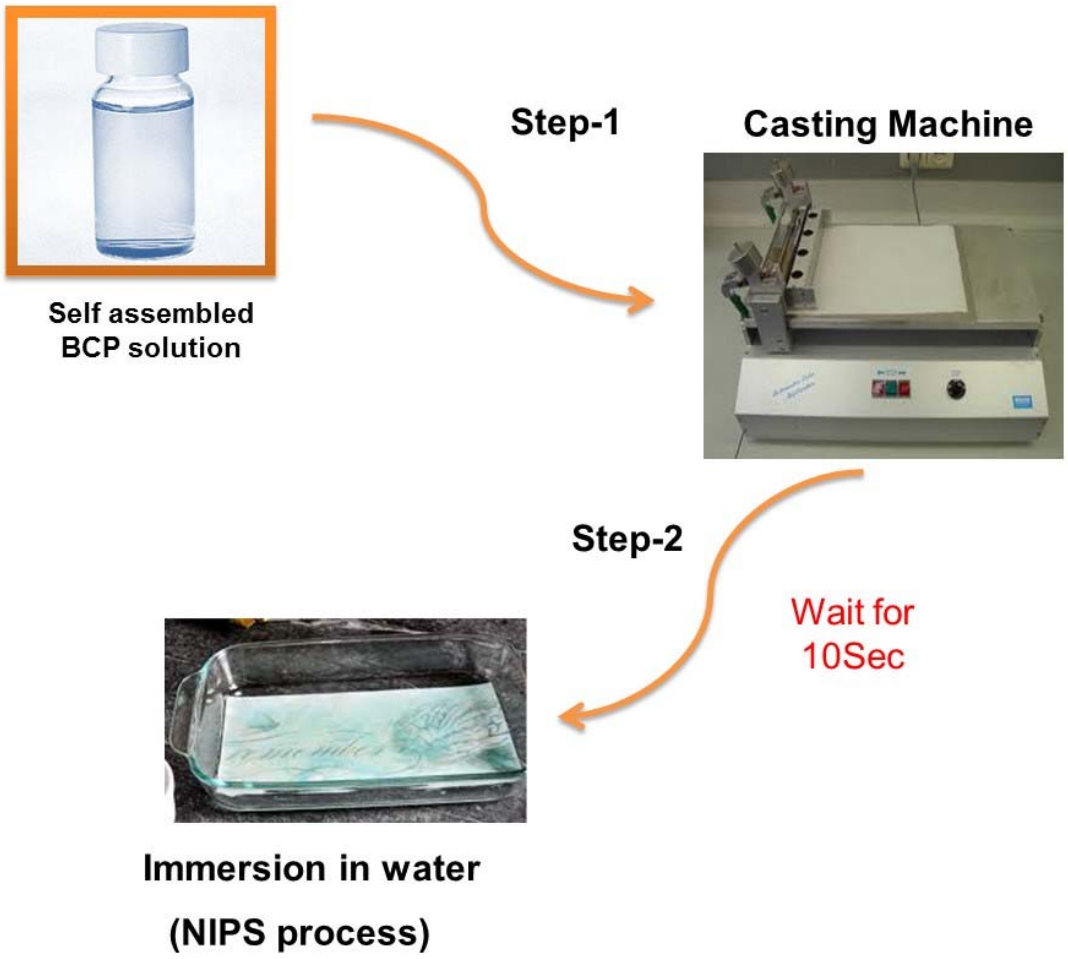

Figure 1.10 Steps for asymmetric PS-b-P4VP membranes preparation by phase inversion method

Initially solvents such as DMF and THF were used for the self-assembly process in solution and water as coagulation bath for the phase inversion process. Different solvent mixtures have been tested with better achievements in terms of membrane reproducibility and stability. Asymmetric membrane with a narrow pore size of about 20-40 nm was obtained on top surface of the membrane followed by a spongy substructure (Figure 1.11). Cryo-Scanning electron microscopy in this case was able to give a clear picture of how a solution is pictured before membrane formation. The solutions with DMF/DIOX /THF reveals the

most promising order in the solution as seen from figure 1.12 which gives a better order in the final membrane. More recently other diblock and triblock copolymers were also used to develop nanoporous membrane by this technique.[41-44] Whereas in most of the cases the block copolymer self-assembly process was controlled using a suitable solvent system for the membrane generation.

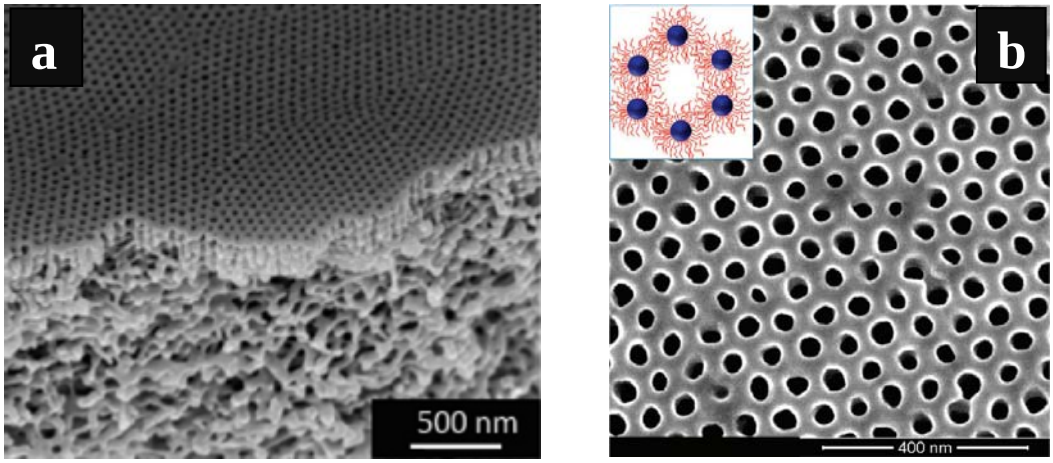

Figure 1.11 Asymmetric PS-b-P4VP block copolymer membrane a) Cross section b) Top surface. Reprinted (adapted) with permission from (Nunes et al, Langmuir 2011, American Chemical Society)[41]

Choosing the right selective solvent mixture and the membrane manufacture condition is an essential criteria for nanopore membrane formation. Most of the above research emphasized that the evaporation time during membrane casting also plays a crucial role in the membrane formation. Recently William et al.[43] reported poly (isoprene-b-styrene-b-4-vinylpyridine) triblock copolymer membrane formation by phase inversion method. In this method they used THF and dioxane as solvents for membrane preparation and water was used as a coagulation bath. Similarly Jung et al.[45] prepared polystyrene-block-poly (2-vinylpyridine)-block-poly (ethylene oxide) (PS-b-P2VP-b-PEO) polymer and developed

an integral asymmetric membranes from this triblock copolymer. The pore structure and water flux showed similar to the diblock copolymer reported.[42]

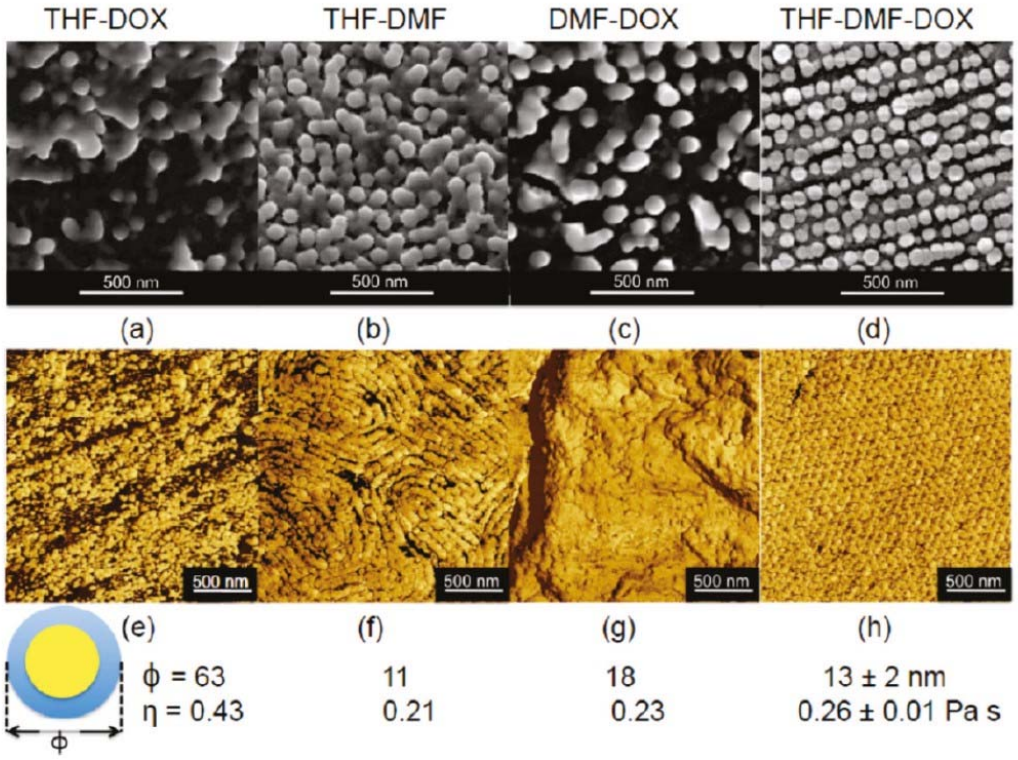

Figure 1.12 Cryo-SEM images and AFM images of final membranes cast with different PS-b-P4VP solutions. Reprinted (adapted) with permission from (Nunes et al, Langmuir 2011, American Chemical Society)[41]

Clodt et al.[46] recently used α -cyclodextrine, α-(D)-glucose, and saccharose as additive material for pore formation in PS-b-P4VP membranes. Nunes et al.[38, 39] reported the metal complexation with block copolymer can also produce nanoporous membrane using the same technique and showed that metal complexation stabilize the micelle lattice, which finally will form the membrane pores (Figure 1.13). The nanopores formed are stimuli pH responsive.

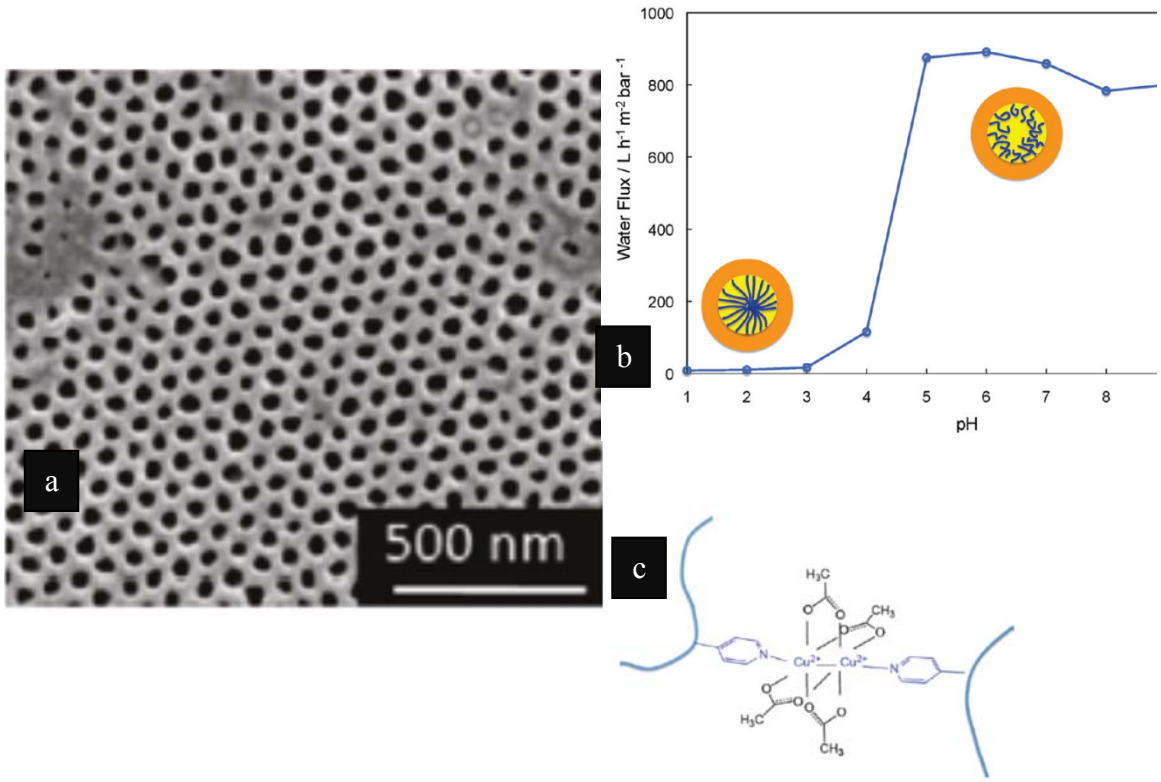

Figure 1.13 a) Cu-Complexed PS-b-P4VP membrane (Top surface) b) Water flux at different pH c) Schematic illustration of complex formation PS-b-P4VP with Cu salts Reprinted (adapted) with permission from (Nunes et al, Macromolecules 2010, American Chemical Society)[38]

1.1.9 Post functionalization of block copolymer membranes

By possible functionalization of one of the blocks or any reaction change can lead to different functional groups in the same block copolymer. In that case the final application can be different depending on the functional groups. The other main advantage of using block copolymers for membrane manufacture is the ability to design pores with controlled morphology. Yu et al.[47] reduced the pore size of PS-b-P4VP membranes larger than 15 nm to in between 3 and 20 nm by electroless gold deposition. The pyridine group of the block copolymer PS-b-P4VP has a lone pair of electron on the nitrogen atom, which can act as a

strong ligand to interact with various metal ions or alkyl halides. In this case the pyridine interacts with Au^{3+} ion and the gold layer was deposited by a two-step redox process.

Polyionic isoporous block copolymer membranes prepared by phase inversion method were reported by Shevate et al.[48] which involves post modification of the membranes by simple oxidation procedure. In this case the pyridine group is converted to N-oxide without any harsh conditions.

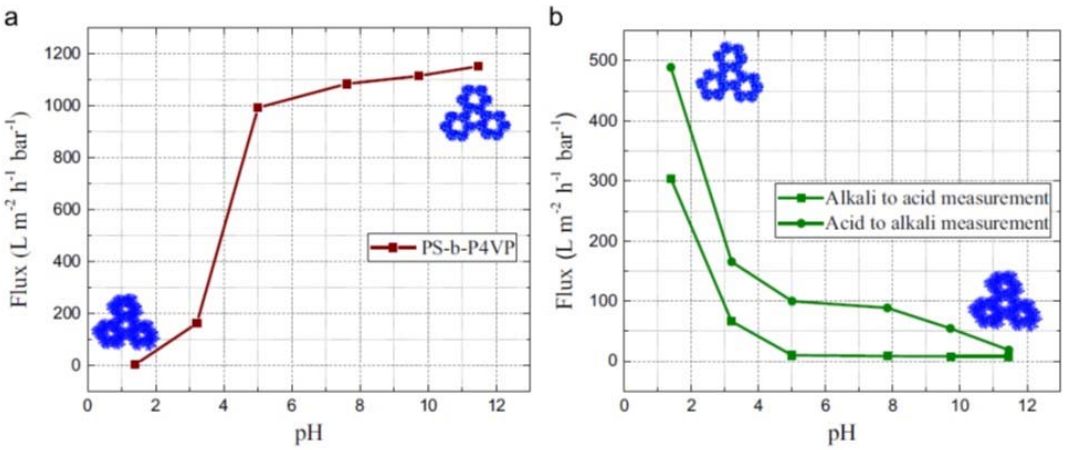

Figure 1.14 pH dependent water flux for PS-b-P4VP membranes and functionalized PS-b-P4VP membranes. [Reprinted (adapted) with permission from Shevate et al. Journal of Membrane science 2016, Elsevier][48]

The resulting membranes showed isoporous geometry with a reverse pH response compared to the original PS-b-P4VP membranes. The water flux values are reversed compared to the unmodified membrane as shown in Figure 1.14 mainly because at low pH the protonation of N^{+}- O^{-} groups in P4VP N-oxide membranes lowers the expansion of polymer chains. Hence the pores are opened whereas at high pH protonation of N^{+}-O^{-} groups results in charge repulsion between chains of P4VP N-oxide groups resulting in

pore closure. The post modification of isoporous thus imparts unique property or chemical functionality, which can be used for several applications

1.2 REFERENCES

1. Basic principles of membrane technology, by Mulder, M. *Kluwer Academic Publishers*, The Netherlands, 2003.

2. Membrane technology and applications by Baker, R. W. *John Wiley & sons*, England, 2000.

3. Membranes and membrane separation processes, Strathmann, H. *Wiley-VCH Verlag GmbH,* Germany, 2005.

4. Website, http://water.org/water-crisis/water-sanitation-facts/

5. Handbook of industrial membrane technology by Porter, M.C. *Noyes publications*, 1990.

6. Pendergasta. M. M.; Hoek, E. M. V. *Energy Environ. Sci.* 2011, 4, 1946-1971.

7. Adiga, S. P.; Curtiss, C.L.A.; Monteiro-Riviere, N.A.; Narayan, R. J. *Nanomed Nanobiotechnol.* 2009, 5, 568–581.

8. Yang, S.Y.; Ryu, I.; Kim, H. Y.; Kim, J.K.; Jang, S.K.; Russell, T.P. *Adv. Mater.* 2006, 18, 709–712.

9. Jackson, E. A.; Hillmyer, M. A. *ACS Nano* 2010, 4, 3548-3553.

10. Hand book of nanoporous materials from block copolymer precursors- Block copolymers II by Hillmyer, M. A. *Advances in Polymer Science.*

11. Nunes, S. P.; Sougrat, R.; Hooghan, B.; Anjum, D. H.; Behzad, A.R.; Zhao, L.; Pradeep, N.; Pinnau, I.; Vainio, U.; Peinemann, K. V. *Macromolecules* 2010, 43, 8079-8085.

12. Formation and Modification of Polymeric Membranes: Overview, by Pinnau, I.; Freeman, B. D. *ACS Symposium Series*.

13. The Loeb-Sourirajan Membrane: How It Came About Membrane, by Loeb, S. *ACS Symposium Series,* 1981, 1-9

14. Strathmann, H.; Kock, K. *Desalination*, 1977, 21, 241-255

15. Smolders, C.A.; Reuvers, A. J.; Boom, R. M.; Wienk, I. M. *J. Membr. Sci.,* 1992, 73, 259–275.

16. Park, H. A.S.; Kim, S. W.; Yoo, P. J.; Ryu, D. Y.; Russell, T.P. *ACS Nano*, 2014, 8, 11745–11752

17. Sperschneider, A.; Schacher, F.; Gawenda, M.; Tsarkova, L.; Müller, A.H.E, Ulbricht, M.; Krausch, G.; Köhler, J. *Small*, 2007, 3, 1056-1063.

18. Phillip, W. A.; Rzayev, J.; Hillmyer, M. A.; Cussler, E. L. *J. Membr. Sci.,* 2006, 286, 144–152

19. Chen, L.; Phillip, W. A.; Cussler, E. L.; Hillmyer, M.A.; *J. Am. Chem. Soc.* 2007, 129, 13786-13787

20. Mai, Y.; Eisenberg, A.; *Chem. Soc. Rev*, 2012, 41, 5969-5945.

21. Bates, F. S.; Fredrickson, G. H. *Physics Today*, 1999, 52, 32-38

22. Bates, F. S. *Annu. Rev. Phys. Chem*. 1990, 41, 525-57

23. Amphiphilic Block Copolymers: Self-Assembly and Applications by Alexandridis, P.; Lindman, B, *Elsevier*, Amsterdam, 2000.

24. Thomas, E. L.; Anderson, D. M.; Henkee, C. S.; Hoffman, D. *Nature*, 1988, 334, 598–601.

25. Bates, F. S. *Science*, 1991, 251, 898–905.

26. Discher, D. E.; Ahmed, F. Annu. Rev. Biomed. Eng., 2006, 8,323–341

27. Zhang, L.; Eisenberg, A. *Science*, 1995, 268, 1728–1731.

28. Halperin. A.; Tirell,M.; Lodge, T.P. *Adv.Poym.Sci.*1992, 100, 31-71

29. Uehara, H.; Kano, M.; Tanaka, H.; Kato, S.; Masunaga, H.; Yamanobe, T. *RSC Adv*.

2014, 4, 42467-42470

30. Crossland, E. J. W.; Cunha, P.; Ludwigs, S.; Hillmyer, M. A.; Steiner, U. *ACS Appl.*

Mater. Interfaces 2011, 3, 1375–1379

31 Li, Y.; Maire, H. C.; Ito, T. *Langmuir* 2007, 23, 12771–12776

32 Hillmyer, M. A.; *Adv Polym Sci* 2005, 190, 137–181,

33 Demire, G. B.; Buyukserin, F.; Morris, M. A.; Demirel, G. *ACS Appl. Mater. Interfaces* 2012, 4, 280–285,

34 Yang, S. Y.; Son, S.; Jang, S.; Kim, H.; Jeon, G.; Kim, W. J.; Kim, J. K. *Nano Lett.* 2011, 11, 1032–1035

35. Thurn-Albrecht, T.; Schotter, J.; Kastle, G. A.; Emley, N.; Shibauchi, T.; Krusin-Elbaum, L.; Guarini, K.; Black, C. T.; Tuominen, M. T.; Russell, T. P. *Science* 2000, 290, 2126−2129.

36. Wang, Y.; He, C.; Xing, W.; Li, F.; Tong, L.; Chen, Z.; Liao, X.; Steinhart, M. *Adv. Mater.* 2010, 22, 2068-2072.

37. Peinemann, K.V.; Abetz.V.; Simon, P.W.F. *Nat. Mat*. 2007, 6, 992-996.

38. Nunes, S. P.; Karunakaran, M.; Neelakanda, P.; Behzad, A. R.;Hooghan, B.; Sougrat, R; He, H.; Peinemann, K.-V. *Langmuir* 2011, 27, 10184-10190.

39 Nunes, S. P.; Behzad, A. R.; Hooghan, B.; Sougrat, R.; Karunakaran, M.; Pradeep, N.; Vainio, U.; Peinemann, K. V. *ACS Nano* 2011, 5, 3516-3522.

40. Hilke, R.; Pradeep, N.; Madhavan, P.; Vainio, U.; Behzad, A. R.; Sougrat, R.; Nunes, S. P.; Peinemann, K.-V. *ACS Appl. Mater. Interfaces* 2013, *5*, 7001-7006.

41. Karunakaran, M.; Nunes, S. P.; Qiu, X.; Yu, Peinemann, K. V. *J. Membr. Sci.*2014, 453, 471–477.

42. Jung, A.; Rangou, S.; Abetz, C.; Filiz, V.; Abetz, V. *Macromol. Mater. Eng.* 2012, 297, 790–798.

43. Phillip, W. A.; Dorin, R. M.; Werner, J.; Hoek, E. M.V.; Wiesner, U.; Elimelech, M. *Nano Lett.* 2011, 11, 2892-2900.

44. Schacher, F. H.; Ulbricht, M.; Müller, A. H.E. *Adv. Funct. Mater.* 2009, 19, 1040-1045.

45.Jung, A.; Filiz, V.; Rangou, S.; Buhr, K.; Merten, P.; Hahn, J.; Clodt, J.; Abetz, C.; Abetz, V.; *Macromol. Rapid Commun*, 2013, 34, 610–615.

46. Clodt, J. I.; Rangou, S.; Schröder, A.; Buhr, K.; Hahn, J.; Jung, A.; Filiz, V.; Abetz, V. *Macromol. Rapid Commun,* 2013, 34, 190–194.

47. Yu, H.; Qiu, X.; Nunes, S.P.; Peinemann, K. V. *Angew. Chem. Int. Ed*. 2014, 53, 10072–10076.

48. Shevate, R.; Karunakaran, M.; Kumar, M.; Peinemann, K.-V. *J. Membr. Sci.* 2016, *501*, 161-168.

1.3 OBJECTIVES

The main objective of this work is to tune the nanostructure morphology of membranes prepared from block copolymers in the presence of additives, which could be complexing agents, catalysts, biocides or light responsive segments. Many research reports show that the block copolymer self-assembly process is controlled by the solvents, which preferentially interact each block as part of the pore formation, leading to the final membrane. In this dissertation in addition to solvents, we show that the presence of additives can tune the final membrane morphology and separation ability.

We show that membranes with metallic additives can have additional functions. Finally, stimuli responsive behavior of the block copolymer is studied in the last part of the dissertation, especially the response to light.

Chapter 2 describes the isoporous block copolymer membrane formation with hydrogen bonding additives. In this case six –OH and –COOH containing organic molecules are chosen for the study and their effect on the final membrane morphology has been discussed. In addition their rheological properties after complexing with these small molecules and water flux and retention properties with BSA and Gamma-globulin are discussed.

In Chapter 3, we studied the isoporous membrane formation using green structure-driving additives such as ionic liquids. In this case both protic and aprotic liquids are chosen to study the effect on the final membrane morphology. Interestingly, different membrane morphologies are obtained due to the interaction of pyridine group with ionic liquids. In this case, rheological properties along with water flux and retention properties are

discussed. This chapter describes the TEM tomography imaging of ionic liquid membranes and also Cryo-SEM microscopy for block copolymer solutions with ionic liquids.

The post modification of isoporous block copolymer membranes obtained from PS-b-P4VP is studied in Chapter 4, aiming at adding catalytic properties to the membrane. The membranes with pyridine group were complexed with $HAuCl_4$ followed by reduction with $NaBH_4$ to generate Au^{3+} on the pore walls of the membrane. The resulting membranes are tested for the catalytic activity to convert nitrophenol to aminophenol, a model reaction to test the catalytic effect of gold nanoparticles.

Chapter 5 describes the post modification of isoporous membranes using silver for biocidal purposes. In this case the pyridine group of block copolymer is complexed with silver from $AgNO_3$ precursor followed by reduction with $NaBH_4$ to generate Ag^{+} ions in the pore walls. The pH of $AgNO_3$ solutions were varied as these membranes are pH responsive. In this case the antibacterial activity of the silver complexed isoporous PS-b-P4VP membranes are tested with *P. aeruginosa* and the proportion of viable cells are less for pH 9 membranes compared to pH 2 and pH 7 membranes.

Chapter 6 describes the isoporous membrane formation with poly(styrene-b-anthracene methyl methacrylate-b-methylmethacrylate) (PS-b-PAnMMA-b-PMMA) targeting the development of membranes which are responsive to light. Depending on the solvent compositions and molecular weight these membranes form cylindrical or lamellar structure on the top surface. The photoresponsive behavior of the anthracene block is also studied with UV lights of two wavelengths 254 nm and 365 nm. The water flux and retention properties in response to photodimerization of anthracene block is also studied.

Chapter 7 summarizes and discusses the results of the different chapters and provides an outlook for future research and challenges.

Chapters 2, 3, 4a, 4b, 5 are copies of the paper published elsewhere and reproduced with permission from respective journals. In addition, it is cited in each chapters.

CHAPTER 2

Complexation Tailored Morphology of Asymmetric Block Copolymer Membranes

Summary

Hydrogen-bond formation between PS-b-P4VP block copolymer and –OH/ –COOH functionalized organic molecules was used to tune morphology of asymmetric nanoporous membranes prepared by simultaneous self-assembly and non-solvent induced phase separation. The morphologies were characterized by FESEM and AFM. Hydrogen bonds were confirmed by IR and the results were correlated to rheology characterization. The OH-functionalized organic molecules direct the morphology into hexagonal order. COOH-functionalized molecules led to both lamellar and hexagonal structures. Micelle formation in solutions and their sizes were determined using DLS measurements and water fluxes of 600-3200 $l/m^2h.bar$ were obtained. The pore size of the plain BCP membrane was smaller than with additives. The following series of additives led to pores with hexagonal order with increasing pore size: terephthalic acid (COOH-bifunctionalized) < rutin (OH-multifunctionalized) < 9-anthracenemethanol (OH-monofunctionalized) < 3,5-dihydroxybenzyl alcohol (OH-trifunctionalized).

This chapter was published as*: P. Madhavan, K.V. Peinemann and S.P. Nunes, Complexation Tailored Morphology of Asymmetric Block Copolymer Membranes, ACS Applied Materials and Interfaces, 2013, 5(15), pp 7152-7159.

2.1 Introduction

The self-assembly of block copolymers (BCP) has gain increasing importance for applications such as membranes, templates and lithography[1-3]. The equilibrium morphology in bulk is controlled by the thermodynamic interaction between blocks as well as their degree of polymerization. In solution the block interaction with solvents is an additional very important parameter. In selective solvents different morphologies such as spherical micelles, vesicles, wormlike aggregates, gyroids, lamellas, and cylinders[4-11] can be observed. Efforts have been made to search for new routes to tune the morphologies of block copolymer self-assembly by chemically modifying one of the blocks of BCP[12], changing the pH[13], addition of complex forming metal salt[14], homopolymers and small molecules acting as surfactants, which form hydrogen-bonds with one of the copolymer blocks[15-17]. Complex formation with metal salts (coordination) and small organic molecules (hydrogen-bond formation) are reported to be particularly effective in controlling the morphology[18-20] of thin films. In this way supramolecular chemistry can tune the morphology without the burden of synthesizing completely new families of BCPs. Small organic molecules can be also washed away as a strategy to form nanoporous structures[21].

Varieties of block copolymers are readily available. Polystyrene-*b*-poly (4-vinylpyridine) (PS-*b*-P4VP) is convenient for supramolecular self-assembly, since the basic pyridine groups easily complex with metal salts or hydrogen donor organic molecules containing –OH, -COOH groups. Brinke, Ikkala and co-workers[22-24] are pioneering in supramolecular assembly of BCP with addition of small organic molecules to tune their morphology in solution and in bulk. Our interest is to use analogous supramolecular technique to form

nanoporous block copolymer membranes by phase inversion technique, i.e. by solution casting and immersion in water. We previously demonstrated that nanoporous block copolymer membranes could be obtained with exceptionally high selectivity and high flux, resulting from narrow pore size distribution and a high pore density, respectively[25-28]. The method is easily scalable, at one step, without need for post treatment like block etching or additive post-extraction. We have been working on understanding the mechanism of pore formation involved and optimizing the manufacture process to assure reproducibility with long-range order [26-28]. Figure 2.1 shows a simplified scheme of how micelles assemble in solution to give rise to regular pores. We recently reported a detailed investigation on the mechanism of pore formation in block copolymer membranes by phase inversion with help of small-angle scattering and modeling[29]. Although it is possible to achieve long-range order, by tuning the solvent mixture, the addition of complexing agents is expected to facilitate and stabilize the assembly and/or induce different morphologies. We have reported that metal complexation with PS-b-P4VP allows to generate isoporous membranes by non-solvent induced phase separation[28] even with solvent mixtures and copolymer concentrations, which would not lead to ordered morphology. The degree of order is a function of the different cations used

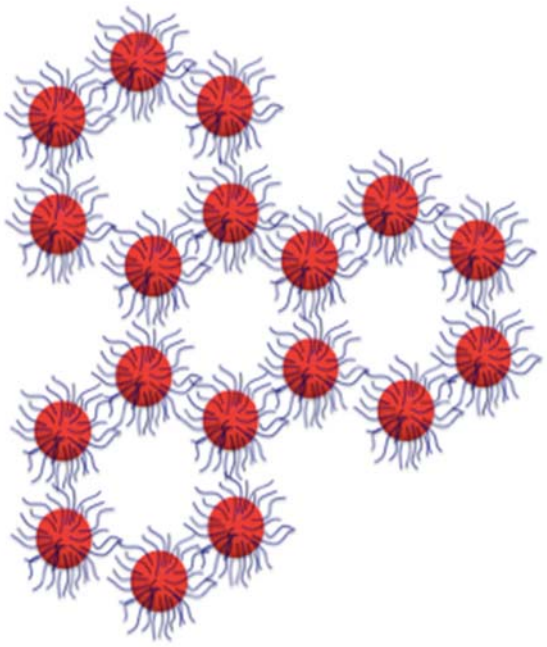

Figure 2. 1 Micelle assembly for formation of hexagonal pores in block copolymer membranes.

such as Cu^{2+}, Ni^{2+}, Co^{2+} and Fe^{2+} and of the pyridine-metal complex stability constant. We believe that the cations intensify the intermicellar links and stabilize the order before immersion in water. We also recently demonstrated that isoporous membranes prepared from block copolymer could be used for challenging tasks like the separation of bovine serum albumin and hemoglobulin, proteins with very similar molecular weights[30]. Extending the application to other biological macromolecules would require membranes with other pore sizes. A potential strategy for pore size control is to change the block size and therefore the micelle dimensions, which are involved in the assembly and pore formation. A challenge is to tune pore size in an even simpler way, which this is the main motivation of this work. By a systematic investigation we demonstrated that organic molecules containing mono-, di-, tri- and polyhydroxyl/acids functional groups strongly interact with the pyridine block of PS-*b*-P4VP, leading to morphology diversification and controlled membrane pore size.

2.2 Experimental section

2.2.1 Materials

Polystyrene-b-poly (4-vinylpyridine) block copolymer P10900-S4VP (PS-b-P4VP 188,000-b-64,000 g/mol) was purchased from Polymer Source, Inc., Canada. Dimethyl formamide (DMF) was supplied by Fisher Scientific; Rutin (Ru) was supplied by Acros organics and used without further purification. 3,5-Dihydroxybenzyl alcohol (DHBA), 9-Anthracenemethanol (AM), Mellitic acid (MA), Terephthalic acid (TPA), 1,3,5-Tris(4'carboxy[1,1'-biphenyl]-4-yl) benzene (Tris) and THF were purchased from Sigma-Aldrich and used as received.

2.2.2 Membrane Preparation

All the membranes were prepared using a solution containing 18 wt % block copolymer (BCP) in a mixture of 50 wt % DMF and 32 wt% THF. Different organic molecules were mixed to the solution and stirred at room temperature for 24 h. The BCP solutions were cast on a glass plate using a casting knife with 200μm air gap. The solvent was allowed to evaporate for up to 10 s, and the film was immersed in water at room temperature followed by drying at 60^{o}C for 24h for IR and DSC analysis.

2.2.3 ATR-FTIR

Perkin-Elmer 100 ATR-FTIR spectrometer was used for recording the IR spectra of block copolymer membrane. Data were collected over 16 scans with a resolution of 4 cm^{-1}. The ATR-FTIR measurements were made at room temperature, using an ATR unit at a nominal incident angle of 45^{o}.

2.2.4 Scanning Electron Microscopy

Micrographs of membranes were obtained using a FEI Quanta 200 Field Emission Scanning Electron Microscope. Imaging was carried out at 5 kV with a working distance of 10 mm. The membrane samples were mounted on aluminum stubs using aluminum tape and Au coated before imaging for 45s at 20mA.

2.2.5 Atomic Force Microscopy

AFM analysis was performed using an ICON Veeco microscope in tapping mode. The tip characteristics are as follows: spring constant 3 Nm^{-1}, resonant frequency 60-80 Hz. Block copolymer membranes were dried and a small piece of membranes were imaged directly.

2.2.6 Rheology

Rheological Measurements were carried out at 25^0 C with AR- 1500 ES Rheometer with a cone and plate fixture of diameter 25 mm and a cone angle of 1^0. The rheology measurements were performed in the linear viscoelastic region. The range of shear rates used for the viscosity measurements is 10-1000 s^{-1}.

2.2.7 Dynamic Light Scattering (DLS)

DLS measurements were taken with a Malvern Zetasizer Nano Series(nano-ZS) at room temperature. Solutions of 0.1 g/L PS-b-P4VP with various weight percent of –OH and –COOH molecules in DMF/THF solvent mixtures were investigated.

2.2.8 Water Flux Measurement

Pure water fluxes of membranes were measured using a stirred Amicon dead-end ultrafilitration cell at 1 bar. The membranes for flux measurements were prepared on a nonwoven polyester support. Effective membrane area was 5 cm^2. Deionized water was used for water flux measurements.

2.3 Results and discussion

The organic molecules bearing –OH and –COOH functional group in Figure 2.2 and 2.3 have been used for complex formation with PS-b-P4VP block copolymer and membrane formation.

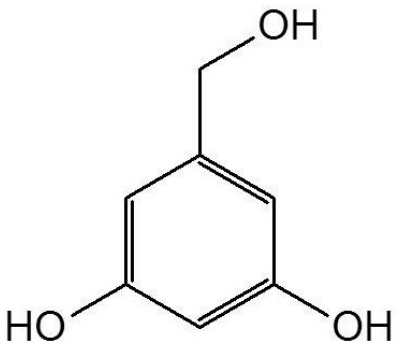

3,5-Dihydroxybenzyl alcohol (DHBA)

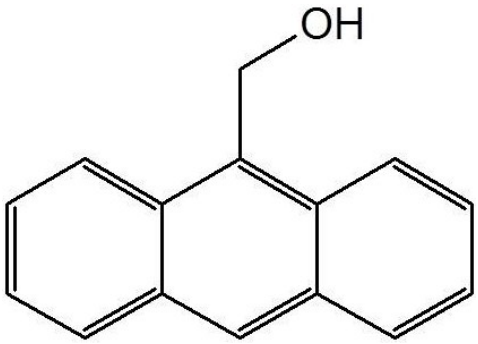

9-Anthracenemethanol (AM)

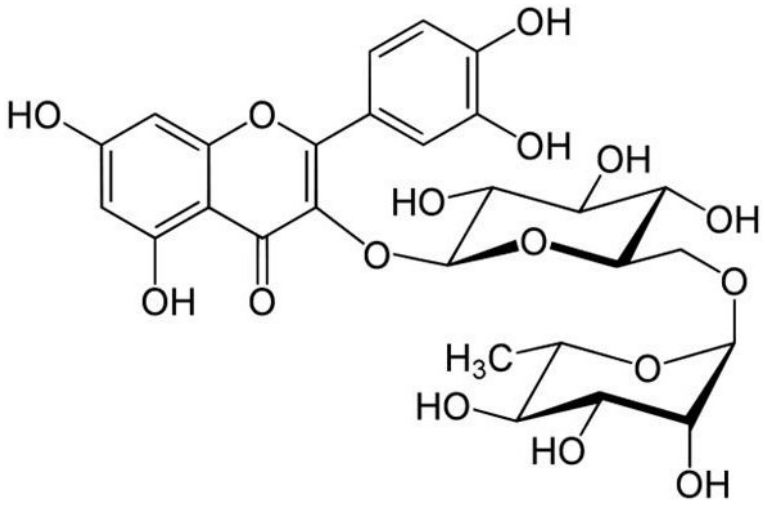

Rutin (Ru)

Figure 2.2 OH-bearing organic molecules for supramolecular self-assembly with PS-b-P4VP

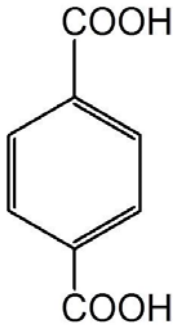

Terephthalic acid (TPA)

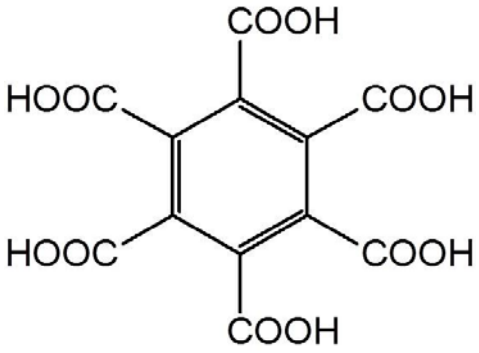

Mellitic acid (MA)

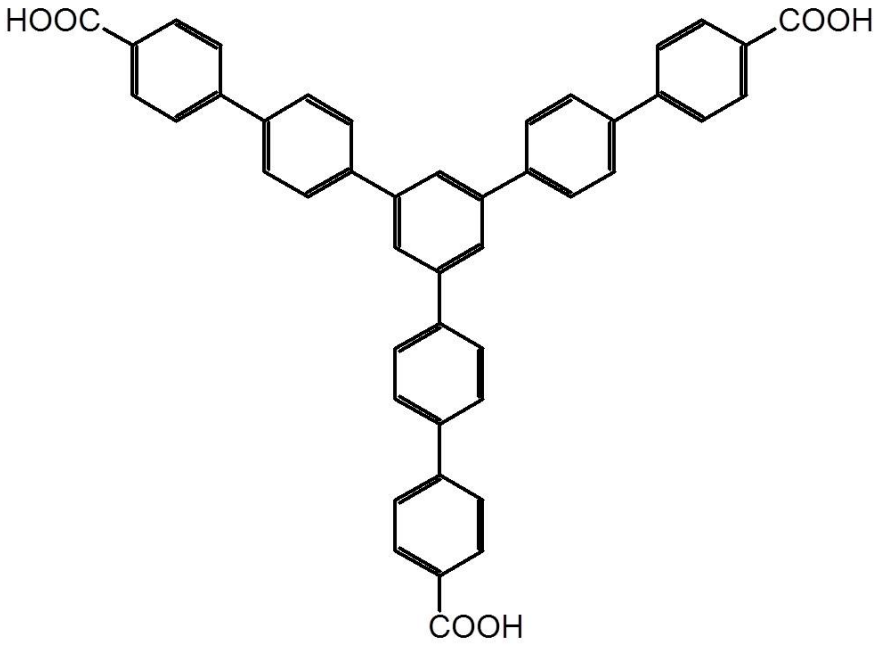

1,3,5-Tris(4'carboxy[1,1'-biphenyl]-4-yl) benzene (Tris)

Figure 2.3 COOH-bearing organic molecules used for supramolecular self-assembly with PS-b-P4VP

We have demonstrated that the complexation of P4VP blocks with metals such as Cu, Ni, Fe, Co could be used to guide the formation of ordered nanoporous membranes[27, 28] Small organic molecules with strong tendency of forming hydrogen bonds and/or favoring acid-base complexation[6, 24] have been proposed by different groups to guide the nano-

structuration of block copolymer systems. Zoelen et al.[24] used the strong interaction of pentadecylphenol and pyridine to induce the formation of nanorods. Hayward and Pochan[6] used multi-amines to tailor assemblies of poly (acrylic acids). The amines are able to redefine micelle geometries and introduce long-range interactions. Complexation of P4VP-containing block copolymers with small molecules like naphtol, naphtoic acid and 1-pyrenebutyric acid, perfluorooctanoic acid, which contain hydrogen donor groups, has been explored to prepare nanostructured dense BCP thin film by dip coating [31-33]. Here we propose an analogous strategy, using different molecules to direct the morphology of nanoporous membranes manufactured by combining phase inversion and block copolymer self-assembly. We focused on two classes of molecules: with OH and –COOH groups as in Figure 2.2 and 2.3. Organic molecules such as Rutin (3 wt%), DHBA (6 wt%), MA (6 wt%), TPA (3 wt%), Tris (6 wt%), AM (6 wt%) were blended with PS-b-P4VP in solution for hydrogen bond formation. The organic molecules were added to the BCP solution and stirred for 24 h at room temperature. The copolymer composition (18 wt %) and solvents were kept constant for all casting solutions. The amounts of added organic molecules were mostly 6 wt %, but for Rutin and TPA only a maximum of 3 wt % could be added without precipitation. The solutions were cast on a glass plate or polyester non-woven, evaporated for 10 s and immersed in water for phase inversion. When immersed in water solvent-water exchange occurs. The solvent in the BCP solution migrates to water and the water penetrates into the incipient membrane solution to create the pores on the top surface of membrane. Phase separation proceeds and the porous substructure of the membrane is then formed. To study the hydrogen bonding behavior and morphology of membrane, pure BCP

solutions were cast and manufactured into membranes under the same condition, and compared with those obtained in the presence of different organic molecules.

2.3.1 ATR- FTIR characterization

Chemical structure and hydrogen bond formation between PS-b-P4VP and –OH/COOH containing organic molecules were investigated using IR spectroscopy. Figure 2.4 shows the IR spectra range with peaks, which are relevant for hydrogen bonds.

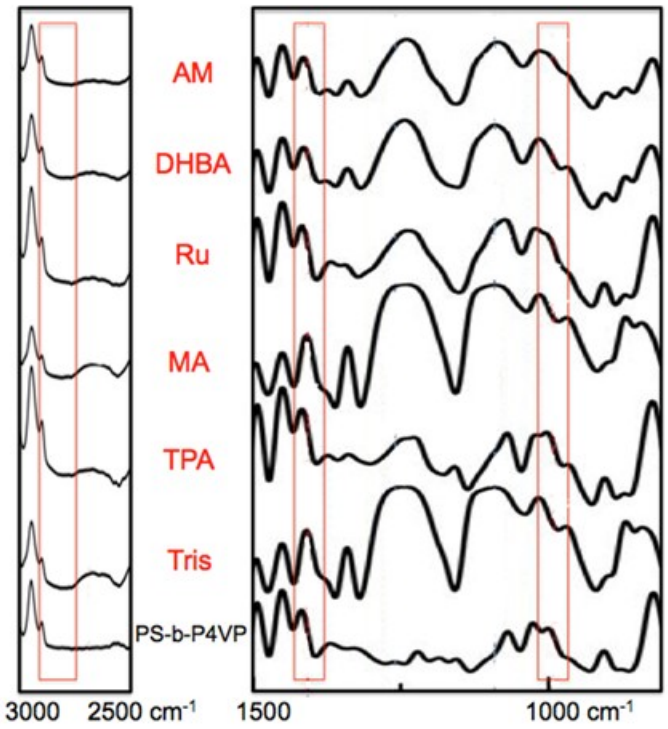

Figure 2.4 ATR-FTIR spectra for PS-b-P4VP nanostructured membranes (plain membranes and membranes with different additives).

An absorption band at 995 cm^{-1} corresponds to the free pyridine group, observed in pure BCP membrane. This peak shifted to 1013cm^{-1} after the formation of H-bonds with proton donor groups. This is evident for Tris, MA, TPA (less than for the first two) and for DHBA.

For AM and Ru practically no change can be seen. An absorption peak near 1415cm^{-1}, for the plain membranes is characteristic of unbounded pyridine. The peak is broadened and slightly shifted to 1419cm^{-1} after hydrogen bond formation between pyridine and the hydrogen-donor groups. The change in the peak again is more accentuated for Tris and MA. The appearance of a broad absorption band at 2550cm^{-1} for BCP solutions with acid functionalized organic molecules indicates the presence of hydrogen bonding between the acid functional group and the pyridine moiety of the BCP. Additional absorption bands (not all shown in Figure 2.4) are present at 2153, 1715, 1340, 1238, 1095 cm^{-1} for membranes formed from solutions with small organic molecules. This indicates that after the phase inversion process, the additives are still strongly bonded and are not completely washed out of the membrane.

Both Tris and MA are functionalized with at least three COOH groups, which are symmetrically placed in the molecule. Hydrogen-bonds formation[34-36] depends on the strength of the proton donors and acceptors and the effectiveness of the complex formation between different molecules depends also on the steric position of the proton donor group as well as the preference to intermolecular hydrogen bonds compared to intramolecular ones. Intramolecular bonds are for instance preferred if six-membered-rings could be formed. The preference for intermolecular hydrogen bonds instead of intramolecular dimers is the key for building co-crystals of small molecules. Carboxylic acid-pyridine H-bonds play an important role in the formation of pharmaceutical co-crystals designed by supramolecular chemistry and crystal engineering.[36,37] Carboxylic acid moieties are among the most frequent in supramolecular synthons,[36,37] which include self-associated systems like dimers and hetero associations (heterosynthons) composed of complementary

functional groups. The analysis of crystal structures containing carboxylic acids in the presence of molecules, containing basic nitrogen atoms as part of a delocalized or conjugated system, demonstrates 98% preference for supramolecular heterosynthons. The requirements for complexation with a pyridine block to guide the copolymer assembly in our work are analogous and COOH-functionalized molecules showed to be excellent additives with strong hydrogen bonds confirmed by FTIR. Alcohols are similar to carboxylic acids as they both can be a hydrogen bond donor or acceptor, depending on the complementary moiety. With pyridine they both act as proton donor. In the presence of basic nitrogens like in pyridine at least 50 % of supramolecular heterosynthons (78% in the absence of other proton donors) are formed instead of homosynthons. Although less effective than COOH-functionalized molecules, those bearing OH groups have been also reported to affect self-assembly.[33] In a recent paper, cyclodextrine was used to optimize the morphology of PS-b-P4VP porous films.[38] The IR spectra analysis of the systems investigated here indicates that the most effective hydrogen-bond among the OH-functionalized molecules is DABH. The molecule contains three OH groups, which are symmetrically placed, facilitating the interaction with different pyridine groups. AM on the other hand is monofunctional and therefore not appropriate as linker between 2 pyridine blocks.

2.3.2 Membrane Morphology

Field emission scanning electron micrographs (FESEM) and topographic atomic force micrographs (AFM) are shown in Figure 2.5 and 2.6 for membranes prepared by complexation of hydroxyl functionalized organic molecules and block copolymers, followed by phase inversion in water. The solvent composition and polymer weight

proportion for all membranes were maintained the same (18 wt % copolymer). Figure 2.5a represents the surface of the pure PS-b-P4VP membrane with no significant order. Figure 2.5b-d shows membranes with complexing agents as additives. PS-b-P4VP(DHAB), PS-b-P4VP(Ru), PS-b-P4VP(AM) have hexagonal ordered pores. With anthracene methanol (AM), the order is the most pronounced. The hexagonal morphology could be better confirmed by AFM (Figure 2.6). AM being monofunctional, has no possibility of linking two different pyridine groups.

(a) (b)

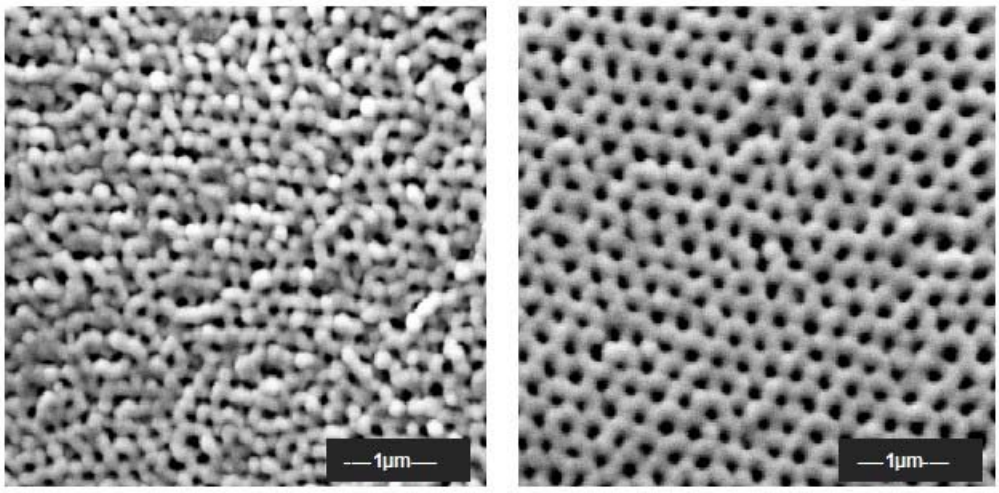

(c) (d)

Figure 2.5 FESEM images of PS-b-P4VP nanostructured membrane: (a) Pure PS-b-P4VP, (b) PS-b-P4VP (6 wt % DHBA), (c) PS-b-P4VP (3 wt % Ru), (d) PS-b-P4VP (6 wt % AM)

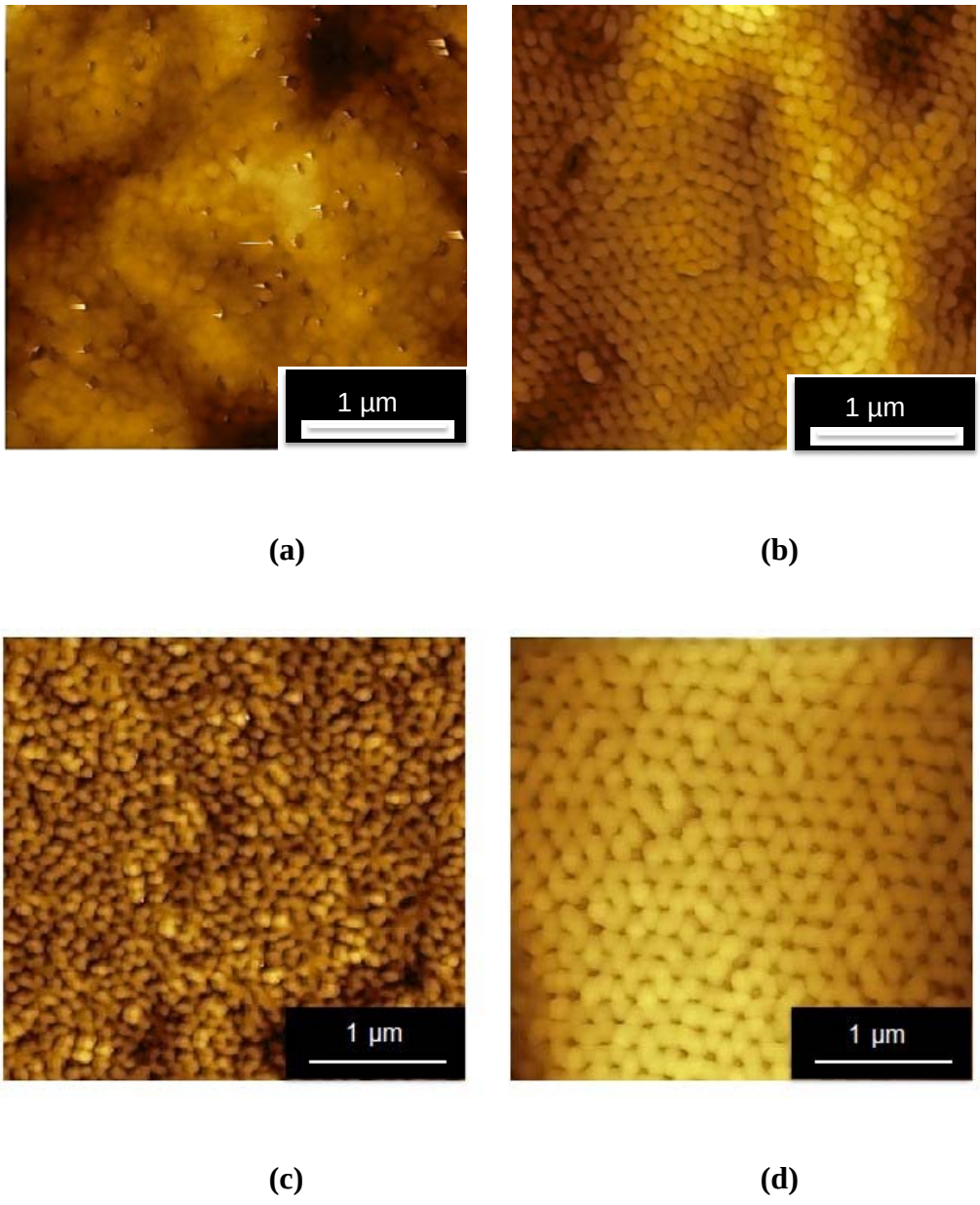

Figure 2.6 AFM images of PS-b-P4VP nanostructured membrane: (a)Pure PS-b-P4VP, (b) PS-b-P4VP (6 wt % DHBA), (c) PS-b-P4VP (3 wt % Ru), (d) PS-b-P4VP (6 wt % AM).

However it can decrease the flexibility of the P4VP segments. We have demonstrated that when we combine BCP self-assembly phase separation in water, the mechanism of pore formation involves BCP micelles formation and their supramolecular assembly.[26,27,39] In the presence of AM, the P4VP-rich corona might become less deformable than without

AM. Rigid spherical micelles are better ordered[26]. At the same time the inclusion of AM in the corona increases the intermicellar distance and as a consequence the pores are larger than in the plain membrane.

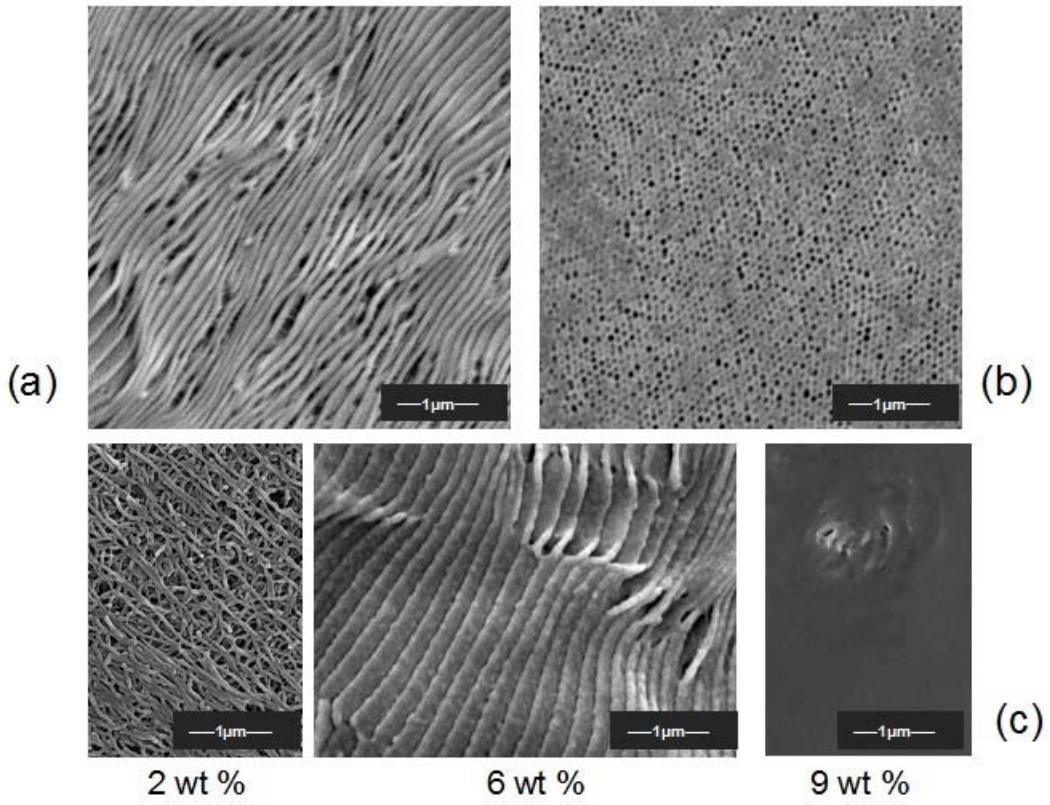

Figure 2.7 FESEM images of PS-b-P4VP nanostructured membrane: (a) PS-b-P4VP (6 wt% Tris), (b) PS-b-P4VP (3 wt % TPA) and (c) PS-b-P4VP (2, 6 and 9 wt % MA)

Membranes from BCP complexed with the bulkier and less symmetric Rutin molecules are more porous than the pure BCP membrane but the order is lower than AM-BCP membranes. DHAB-complexed BCP membranes are highly porous, the order is confirmed by FESEM and AFM, but FESEM images indicate that the assembly might have a preferential stability in one direction. Pores are larger than for the other OH-additives and certainly larger than in the plain membrane.

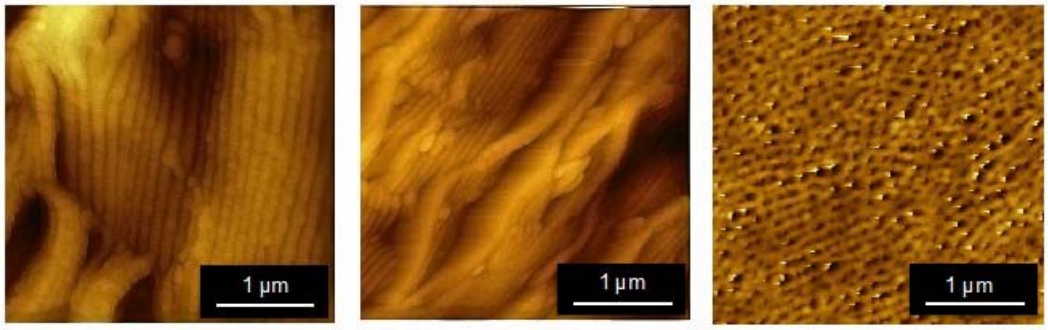

(a) **(b)** **(c)**

Figure 2.8 AFM images of PS-b-P4VP nanostructured membrane: (a) PS-b-P4VP (6 wt % Tris), (b) PS-b-P4VP (3 wt % TPA), (c) PS-b-P4VP (6 wt % MA)

The surfaces of membranes prepared from block copolymer solutions with COOH-functionalized organic molecules are shown in Figure 2.7 (FESEM) and 2.8 (AFM). In Figure 2.7c the influence of the additive concentration can be observed. Excessively high concentration practically eliminates the pores. The membrane prepared with TPA has very ordered hexagonal pores with high porosity and small pore sizes. With this result we can report that while using the same block copolymer, the pore size of the manufactured membrane and the order of the pore morphology can be increased by changing the hydrogen donor additive in the following series:

- Pore size of plain BCP membrane < TPA < Ru < AM < DHBA

Order of plain BCP membrane < Ru < DHBA < TPA = AM

Roland et al.[33] reported the morphology of PS-b-P4VP block copolymer thin-film prepared by dip coating in the presence of napthol and naphthoic acid. In that case the solution was prepared in tetrahydrofuran, which was completely evaporated to form the solid film. They reported preferential dot morphology when 1-naphthol is used and stripes when acid is the

additive, however, the morphology depends also on the coating rate, stripes observed for rapid and thinner coatings.

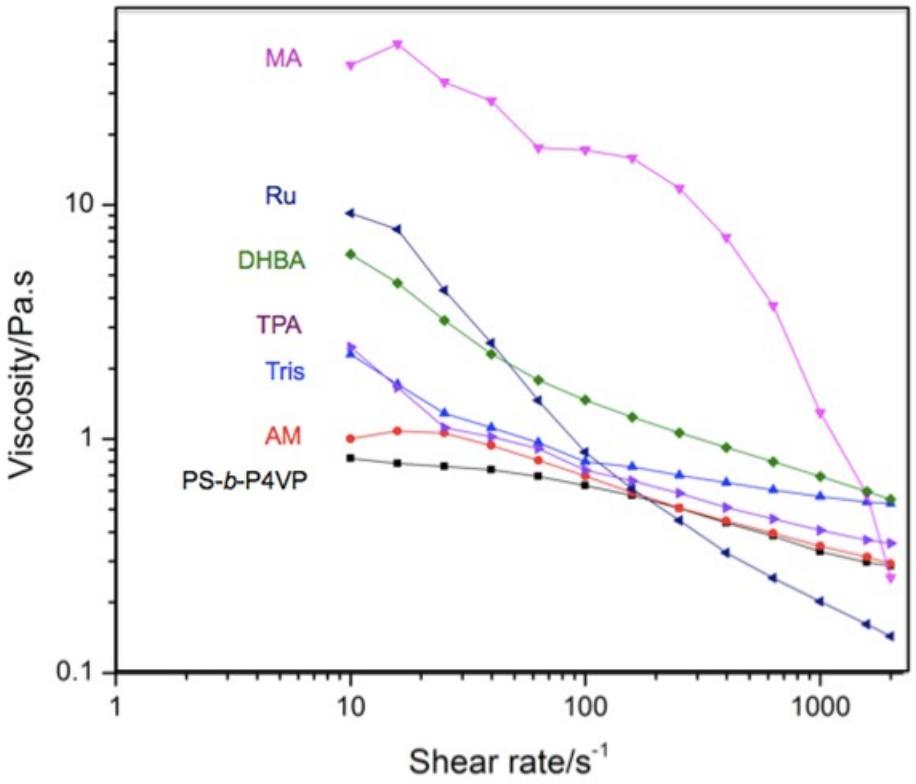

Figure 2.9 Viscosity of PS-b-P4VP solutions with different small organic additives

We work with 32 wt % THF: 50 wt % DMF mixtures. DMF is a polar (solubility parameter closer to P4VP than to PS, favoring PS cores), low-volatile solvent. The solution layers are much thicker (> 100 μm) than used in dip coating and practically independent of substrate wetting influence. A fast solvent-water exchange is promoted, by immersion in water and the morphology is frozen, remaining much closer to that in the solution. According to previous evidence,[26-28] supramolecular micelle assembly is an essential step in the pore formation of self-assembly/phase inversion membranes. Micelles are favored in the

presence of all OH-additives and TPA. On the other hand the addition of MA and Tris led to films with lamellar or cylindrical structure (parallel to the surface).

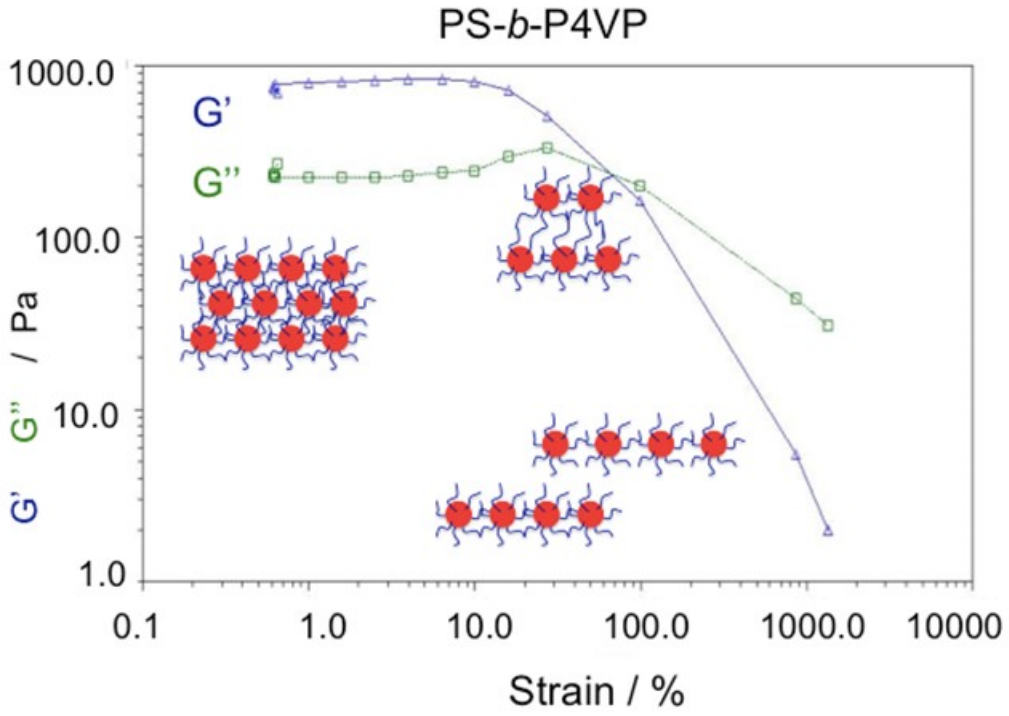

Figure 2.10. Storage (G') and loss (G'') modules as a function of strain (%) at 1 Hz for a 18 wt % PS-*b*-P4VP solution in 50 wt % DMF and 32 wt % THF; scheme of the corresponding micelle assembly in different stages.

The hydrodynamic radii of PS-b-P4VP micelles in dilute solutions with different hydrogen-donor molecules were determined by dynamic light scattering. For DLS measurement DMF/THF solvent mixtures with 50:32 weight ratios were used, analogously to the copolymer membrane casting solution. The copolymer concentration for DLS measurements needs to be much lower (1.0 g /L) than that used for membrane preparation (18 wt %). Light scattering data suggests that micelles are formed in all measured BCP

solutions in THF/DMF. The z-average value of pure BCP micelle radius in the mixed solvent was 8.1 ± 0.2 nm.

Table 2.1. Values of storage (G') and loss (G'') module at low strain for 18 wt % solution of PS-b-P4VP in DMF/THF with different additives; strain % at the crossing point between the G'' and G' curves.

S.No	Additive	G' (Pa) at low strain	G'' (Pa) at low strain	Strain (%) at G'=G''
1	no	800	200	65
2	Ru	300	80	50
3	AM	<20	<20	-
4	DHBA	300	90	50
5	TPA	900	220	70
6	Tris	1000	350	60
7	MA	380	280	-

In BCP solutions with Ru, DHBA, AM and TPA, the z-average values were 8.1 nm, 8.7 nm, 8.3 nm, and 8.3 nm, respectively, practically non-distinguishable. In the solutions containing hydrogen-donor molecules, which led to lamella morphology (Tris and MA) Z-average values for micelle radius are higher than without additive. The z-average values for Tris is 16.3 nm and for MA is 25.2 nm, respectively twice and 3 times higher than for the plain block copolymer in solution.

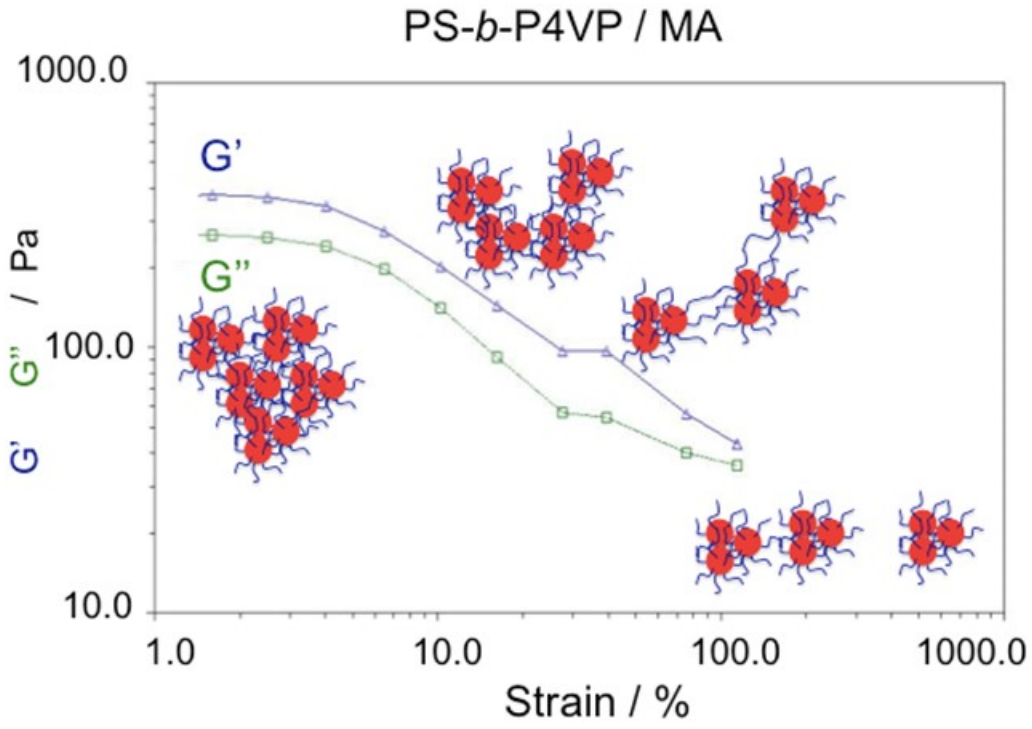

Figure 2.11. Storage (G') and loss (G'') modules as a function of strain (%) at 1 Hz for a 18 wt % PS-*b*-P4VP solution in 50 wt % DMF and 32 wt % THF with mellitic acid; scheme of the corresponding micelle assembly in different stages.

It can be concluded that compact micelles favor the hexagonal order and pore morphology shown in Figure 2.5 and 2.7c. Light scattering data clearly indicates that the addition of organic molecules changes the micelle sizes in solution. The micelle radius size in solutions with Tris and MA are twice and three-fold that for copolymers without additives, respectively, indicating that 2 or 3 micelles might be strongly linked or merged. The multifunctional COOH-molecules could facilitate it. Additionally the interaction of the acid molecules with pyridine groups could be strong enough to at least partially protonate them and promote a stretching of the P4VP block.

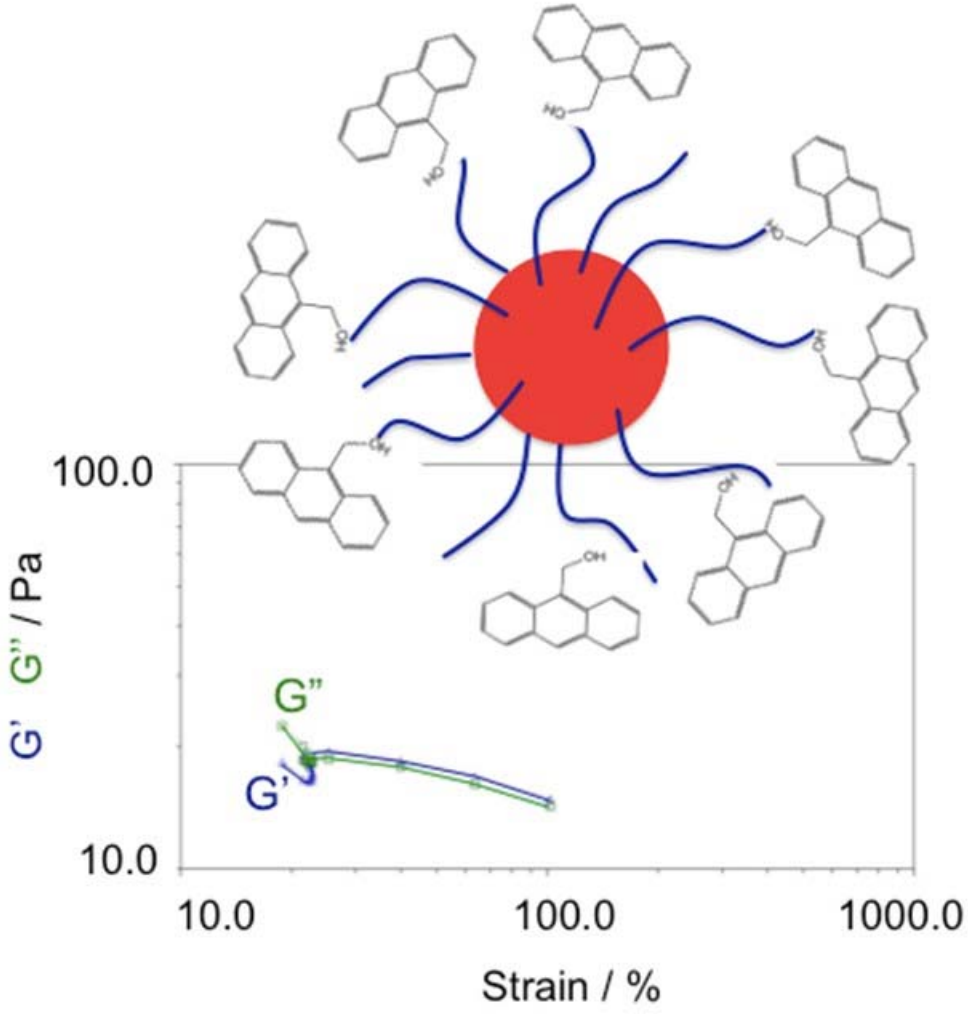

Figure 2.12. Storage (G') and loss (G'') modules as a function of strain (%) at 1 Hz for a 18 wt % PS-*b*-P4VP solution in 50 wt % DMF and 32 wt % THF with 9-anthracene methanol (AM); micelle surrounded by AM molecules forming hydrogen-bonds to pyridine groups in the corona.

The hydrogen bond formation between organic molecules and pyridine affects the solution viscosity and therefore also the membrane formation and final morphology. Figure 2.9 shows how the viscosity changes with the additive incorporation. In all cases the solutions are shear-thinning, indicating that as soon as shear is applied to the ordered assemblies, the

interactions between micelles can be disturbed, facilitating the flow. Solutions with mellitic acid (MA), which has 6 symmetric COOH groups available for interaction with pyridine sites, are those with the highest viscosity, distinguishing from the others. The same system led to micelle radius 3-fold larger than others and led also to final lamellar structure, in opposite to most other investigated systems. The multi COOH functionality certainly facilitates intermolecular and intermicellar linking, causing the increase of viscosity. The second system (Tris), which leads to lamellar structure, however did not substantially distinguish from others, regarding viscosity. The effect of different additives becomes evident in oscillating measurements by taking in account the storage (G') and loss modules (G'') as a function of the strain amplitude at a fixed frequency. There is detailed investigation in the literature on rheology of water-soluble copolymers with poly (ethylene oxide) blocks.[40,41] Their behavior in semi-diluted solution was a starting point for us to understand the micelle rheology in our system as well as results reported by Buitenhuis and Förster[42] for PS-b-P4VP in toluene. Toluene is a better solvent for PS and induces micelle formation with P4VP core, in opposite to the DMF/THF solvent mixture chosen here. For the 188,000-*b*-64,000 g/mol PS-b-P4VP system investigated here, "crew cut" micelles with P4VP corona are expected in a 50 (wt%) DMF / 32 (wt%) THF solvent mixture. Figure 2.10 shows the dependence of G' and G'' on strain. Below 65 % strain, G' is higher than G'', indicating a strong elastic contribution, typical of soft and hard gels. This is the result of closely packed micelle assemblies, which have been confirmed by SAXS before[29]. As the strain increases G' and G'' are constant up to 10 %. G' decreases. A strain overshoot is observed for G'', indicating breakup of the network. Above 65 % a strain thinning is observed due to the possibility of layers sliding with the flow direction.

The viscous contribution to the flow predominates and the system behaves like a sol with G' < G''. A scheme representing the transition is proposed in Figure 2.10. A similar behavior was observed for solutions containing different additives, except for 9-anthracenemethanol (AM) and mellitic acid (MA), as summarized in Table 2.1. The elastic contribution, reflected by G', is larger for terephtalic acid (TPA) and 1,3,5-tris(4'carboxy[1,1'-biphenyl]-4-yl) benzene (Tris) than for the plain copolymer solution. Strong hydrogen bonds were confirmed by IR (Figure 2.4) for the 2 systems. They contribute to increase the intermicellar linking and stabilize the gel. This is an important aspect to maintain the assembly order during the immersion in water, during the membrane manufacture.

Although MA forms also strong hydrogen bonds to pyridine and led to copolymer solutions with higher viscosity than the others, G' and G'' were relatively low and not far from each other (Figure 2.12). As the strain amplitude decreases, both decrease and G' continues to be slightly larger than G''. An explanation for it is shown in Figure 2.12. The multi-functionality of MA allows the formation of a large number of hydrogen bonds. Strong intra and intermicellar linking lead to the formation of aggregates and the system is metastable. The solution is visually milky. The large aggregates are not strongly linked to form a strong network. As the strain is increased the connection between the large aggregates is broken and they are progressively aligned with the flow direction.

A different behavior was observed for solutions with AM. The monofunctional molecule forms hydrogen bonds with pyridine, which becomes less available to interact with segments of another micelle. The inter-corona link decreases, G' and G'' are similar and the elasticity of the gel is low. At the same time the rigid anthracene units make the

membrane less deformable and lead to a very uniform morphology (Figures 2.5d and 2.6d). The bulky anthracene moieties might also stretch the corona segments and/or be partially dissolved in the PS core. A swollen ordered morphology can be seen by microscopy and larger pores are formed.

2.3.3 Water flux measurement and retention

Water flux measurements were carried out using an Amicon ultrafiltration under 1bar N_2 gas pressure. Table 2.2 reports the water flux of pure PS-b-PVP membrane and those with complexing organic molecule. All the membranes had a high water flux between 600 and 3200 $L.m^{-2}\,h^{-1}.bar^{-1}$. The water flux did not follow a trend or correlation to the structure on the membrane top layer. The lamellar structured BCP membranes such as PS-b-P4VP (MA) and PS-b-P4VP (Tris) had fluxes of 3000 and 1600 $L\ m^{-2}\,h^{-1}\ bar^{-1}$. Membranes with hexagonal order had water flux from 600 to 3200 $L\ m^{-2}\,h^{-1}\ bar^{-1}$. The retention of bovine albumin (molecular weight 66,000 g/mol) was measured, by filtering the protein solution and analyzing UV absorption. The lamellar-structured membranes (Tris) had the lowest retention (5%). The elongated pores are not selective enough. The retention is more than 5-fold higher (26%) for (AM) membranes. Both AM and TPA led to pores with hexagonal order. (TPA) membrane pores are clearly smaller (Figure 2.5d and 2.7c) than those of (AM) membranes. TPA membranes are able to retain 62% of albumin. The retention of gamma-globulin (molecular weight 150,000 g/ mol) was 94% for AM membranes, while for the lamellar Tris it was only 15%.

Table 2.2. Water flux and retention of membranes prepared from PS-*b*-P4VP solutions with different additives

S. No	Additive	Water flux (10^3 L m^{-2} h^{-1} bar^{-1})	Albumin Retention (%)
1	no	1.2 ± 0.2	-
2	DHBA (OH)	0.6 ± 0.2	-
3	AM (OH)	1.8 ± 0.2	26 ± 2
4	Ru (OH)	3.2 ± 0.2	-
5	TPA (COOH)	1.2 ± 0.2	62 ± 2
6	Tris (COOH, lamella)	1.6 ± 0.2	5 ± 2
7	MA (COOH, lamella)	3.0 ± 0.2	-

Therefore we confirm that the membranes with hexagonal pore morphology are much more selective than those with lamellar order, while still keeping very high flux. Probably due to the rigidity of the corona, the resulting pores of the AM membrane are not only very uniform; they are less deformable than in the case of other membranes. This contributes to the high separation factor for globulin/albumin.

2.4 REFERENCES

1. Jackson, E. A.; Hillmyer, M. A. *ACS Nano* 2010, 4 (7), 3548–3553.
2. Chinthamanipeta, P.S.; Lou, Q.; Shipp, D. A. *ACS Nano* 2011, 5 (1), 450–456.
3. Li, M; Douki, K; Goto, K.; Li, X.; Coenjarts, C.; Smilgies, D. M.; Ober, C. K. *Chem. Mater*. 2004, 16, 3800-3808.
4. Bates, F. S.; Fredrickson, G. H. *Physics Today* 1999, 52, 32-38.
5. Vukovic, I.; Voortman, T. P.; Hermida Merino, D.; Portale, G.; Ruokolainen, P. H. J.; Ten Brinke, G.; Loos, K. *Macromolecules* 2012, 45, 3503−3512.
6. Hayward, R. C.; Pochan, D. J. *Macromolecules* 2010, 43, 3577–3584.
7. Ludwigs, S.; Boker, A.; Voronov, A.; Rehse, N.; Magerle, R.; Krausch. G. *Nat. Mater*. 2003, 2, 744-747.
8. Albert, J. N. L.; Epps,T. H. *Mater. Today* 2010, 13(6), 24-33.
9. Elbs, H.; Fukunaga, K.; Stadler, R.; Sauer, G.; Magerle, R.; Krausch, G. *Macromolecules* 1999, 32, 1204-1211
10. Malenfant, P. R. L.; Wan, J.; Taylor, S.T.; Manoharan, M. *Nat. Nano Tech.* 2007, 2, 43- 46.
11. Xu, T.; Stevens, J.; Villa, J.A.; Goldbach, J.T.; Guarini, K.W.; Black, C.T.; Hawker, C.J.; Russell, T.P. *Adv. Funct.Mater.* 2003, 13, 698-702.
12. Cheng, F.; Yang, X.; Peng, H.; Chen, D.; Jiang, M. *Macromolecules* 2007, 40, 8007-8014.
13. Zhulina, E. B.; Borisov, O.V. *Macromolecules* 2012, 45, 4429-4440.
14. Noro, A.; Sageshima, Y.; Arai, S.; Matsushita, Y. *Macromolecules* 2010, 43, 5358-5364

15. Zhang, L.; Eisenberg, A. *J. Am. Chem. Soc*. 1996, 118, 3168-3181.

16. Cui, H.; Chen, Z.; Wooley, K. L.; Pochan, D. J. *Soft Matter* 2009, 5, 1269-1278.

17. Zhong, S.; Cui, H.; Chen, Z.; Wooley, K. L.; Pochan, D. J. *Soft Matter* 2008,4, 90-93

18. Koh, H. D.; Park, S.; Russell, T. P. *ACS Nano* 2010, 4, 1124-1130

19. Soininen, A. J.; Tanionou, I.; Ten Brummelhuis, N.; Schlaad, H.; Hadjichristidis, N.; Ikkala, O.; Raula, J.; Mezzenga, R.; Ruokolainen, J. *Macromolecules* 2012, 45, 7091-7097.

20. Valkama, S.; Ruotsalainen,T.; Nykanen, A.; Laiho, A.; Kosonen, H.; Ten Brinke, G.; Ikkala, O.; Ruokolainen, J. *Macromolecules* 2006, 39, 9327-9336.

21. Yang, S.Y.; Ryu, I.; Kim, H.; Kim, J. K.; Jang, S. K.; Russell, T.P. *Adv. Mater.* 2006, 18, 709-712

22. Valkama, S.; Kosonen, H.; Ruokolainen, J.; Haatainen, T.; Torkkeli, M.; Serimaa, R.; Ten Brinke, G.; Ikkala, O. *Nat. Mater*., 2004, 3, 872-876

23. Van Zoelen, W.; Asumaa, T.; Ruokolainen, j.; Ikkala, O.; Ten Brinke, G. *Macromolecules* 2008, 41, 3199-3208,

24. Van Zoelen, W.; Alberda Van Ekenstein, G.; Ikkala, O.; Ten Brinke, G.; *Macromolecules* 2006, 39, 6574 6579.

25. Peinemann, K.V.; Abetz.V.; Simon, P.W.F. *Nat. Mat*. 2007, 6, 992-996.

26. Nunes, S. P.; Karunakaran, M.; Pradeep, N.; Behzad, A.R; Hooghan, B.; Sougrat, R.; He, H.; Peinemann, K.V. *Langmuir* 2011, 27, 10184-10190.

27. Nunes, S. P.; Behzad, A. R.; Hooghan, B.; Sougrat, R.; Karunakaran, M.; Pradeep, N.; Vainio, U.; Peinemann, K. V. *ACS Nano* 2011, 5, 3516-3522.

28. Nunes, S. P.; Sougrat, R.; Hooghan, B.; Anjum, D. H.; Behzad, A.R.; Zhao, L.; Pradeep, N.; Pinnau, I.; Vainio, U.; Peinemann, K. V. *Macromolecules* 2010, 43, 8079-8085.

29. Marques, D. S.; Vainio, U.; Chaparro, N. M.; Calo, V. M.; Behzad, A. R.; Pitera, J. W.; Peinemann, K.V.; Nunes, S. P. *Soft Matter*, DOI:10.1039/C3SM27475F.

30. Qiu, X.; Yu, H.; Karunakaran, M.; Pradeep, N.; Nunes, S. P.; Peinemann. K.V. *ACS Nano* 2013, 7, 768-776.

31. Kuila, B. K.; Gowd, E. B.; Stamm, M. *Macromolecules*, 2010, 43 7713-7721.

32. Peng, H.; Chen, D.; Jiang, M. *J. Phys. Chem. B* 2003, 107, 12461-12464.

33. Roland, S.; Gaspard, D.; Prudhomme, R. E.; Bazuin, C.G. *Macromolecules* 2012, 45, 5463-5476.

34. Donohue, J. *J. Phys. Chem*. 1952, 56, 502-510.

35. Etter, M. C. *J. Phys. Chem*. 1991, 95, 4601-4610.

36. Shattock, T. R.; Arora, K. K.; Vishweshwar, P.; Zaworotko, M. J. *Crystal Growth and Design* 2008, 8, 4533-4545.

37. Almarsson, O.; Zaworotko, M. J.; *Chem. Commun*. 2004, 17, 1889-1896.

38. Clodt, J. I.; Rangou, S.; Schröder, A.; Buhr, K.; Hahn, J.; Jung, A.; Filiz,V.; Abetz, V. *Macromol. Rapid Commun.* 2013, 34, 190-194.

39. Dorin, R. M.; Marques, D. S.; Sai, H.; Vainio, U.; Phillip, W.A.; Peinemann.K.V.; Nunes,S. P.; Wiesner, U. *ACS Macro Lett*. 2012, 1, 614-617.

40. Bhatia, S. R.; Mourchid, A.; Joanicot, M. *Current Opinion in Colloid and Interface Sci.* 2001, 6,471-478.

41. Hyun, K.; Nam, J.G.; Wilhellm, M.; Ahn, K.H.; Lee, S. J. Rheol. *Acta,* 2006, 45, 239-249.

42. Buitenhuis, J.; Förster, S. J. *J. Chem. Phys*. 1997, 107, 262-272.

CHAPTER 3

Ionic Liquids As Self-Assembly Guide For the Formation of Nanostructured Block Copolymer Membranes

Summary

Nanostructured block copolymer membranes were manufactured by water induced phase inversion, using ionic liquids (ILs) as cosolvents. The effect of ionic liquids on the morphology was investigated, by using polystyrene-b-poly(4-vinyl pyridine) (PS-b-PV4P) diblock as membrane copolymer matrix and imidazolium and pyridinium based ILs. The effect of IL concentration and chemical composition was evident with particular interaction with P4VP blocks. The order of block copolymer/ILs solutions previous to the membrane casting was confirmed by cryo scanning electron microscopy and the morphologies of the manufactured nanostructured membranes were characterized by transmission and scanning electron microscopy. Non-protic ionic liquids facilitate the formation of hexagonal nanoporous block copolymer structure, while protic ILs led to a lamella-structured membrane. The rheology of the IL/block copolymer solutions was investigated, evaluating the storage and loss moduli. Most membranes prepared with ionic liquid had higher water flux than pure block copolymer membranes without additives.

This chapter was published as*: Poornima Madhavan, Rachid Sougrat, Ali Reza Behzad, Klaus-Viktor Peinemann and Suzana.P.Nunes, Ionic liquids As Self-Assembly Guide for the Formation of Nanostructured Block Copolymer Membranes, J. Membr. Sci., 2015, 498, pp. 568-577

3.1 Introduction

Block copolymers (BCP) are an attractive class of material that can self-assemble into various nanoscale structures. They have been combined with additives such as salts and nanoparticles to provide a variety of self assembled morphologies. [1-3] The micellization of block copolymers in solvents has been well investigated. Routes to tune the morphologies of block copolymer include chemical modification[4] and the use of additives such as metal salts,[5,6] homopolymer,[7] surfactants,[8] and H-bonding organic molecules.[9, 10] Ionic liquids (ILs) have been also reported to influence the bulk morphology of block copolymers.[11-14] ILs have unique characteristics compared to traditional solvents with negligible vapor pressure, recyclability, non-flammability, thermal and chemical stability[15] and also can lead to specific interaction with polymeric segments, being considered as "designers solvent".[16] ILs have been reported to influence the morphology of block copolymers in solution or in the bulk and dense films. He et al.[17] investigated the micellization of poly(1,2-butadiene)-block-PEO diblock copolymers (PB-*b*-PEO) in 1-butyl-3-methylimidazolium hexafluoro phosphate $[B_4MIM]PF_6$. Gwee et al.[18] showed that the morphology of poly(styrene-b-methyl methacrylate) (SbMMA) can be changed by using different concentrations of IL, going from lamellae to cylindrical microdomains. Virgili et al.[14, 19, 20] studied the phase behavior of polystyrene-*b*-poly(2-vinylpyridine) copolymers in a selective ionic liquid such as imidazolium bis(trifluoromethane) sulfonimide ([IM][TFSI]). They observed ordered microstructures corresponding to lamellae, hexagonally close-packed cylinders, body-centered cubic, and face-centered cubic oriented micelles in the bulk or in thin dense films. A mixed behavior was observed for [IM][TFSI] as selective solvent toward P2VP blocks: at high polymer concentration, it acted similar to a salt with

induced pyridine-metal ion complexation, which results in an increase of the glass transition temperature (T_g), while at intermediate block copolymer concentrations, it acted more like a plasticizer, decreasing T_g.

In membrane technology ionic liquids have been considered before for other reasons. First there is a need for substituting well-established solvents for membrane manufacture to turn the manufacture process more environmentally friendly[21,22]. Xing et al.[23, 24] were the first to report the fabrication of cellulose acetate membranes using ionic liquids as casting solvents. A second reason to integrate ionic liquids in membrane systems is their strong interaction with CO_2, which leads to high gas selectivity. In this case the ionic liquid has been supported in porous membranes[25] or polymerized to constitute a gas separation membrane.[26,27] Ionic liquids have been also reported to facilitated bioconversion processes in combination with membrane separation technology like pervaporation.[28]

In this work we use ionic liquids for the first time to tune the pore morphology of nanostructured block copolymer membranes, produced by self-assembly and water induced phase separation. The general idea of combining block copolymer self-assembly and phase inversion to manufacture isoporous membranes was proposed and demonstrated by Peinemann et al.[29] using polystyrene-b-poly (4-vinyl pyridine) casting solutions in dimethylformamide (DMF) and tetrahydrofuran (THF). However this initially proposed copolymer/solvent system is sensitive to minor changes of molecular weight. Only with better understanding of the mechanism of pore formation based on micelle supramolecular assembly in solution it was possible to find alternative solvent mixtures, leading to stricter and more reproducible morphology control.[30] This could be achieved for instance with the addition of copper acetate,[30, 31] ternary solvent mixtures with dioxane[32,33] and hydrogen

bond forming molecules.[34] The disclosure of the mechanism facilitated the application of this method extended to other systems, containing for instance triblock copolymers.[35, 36] Ionic liquids have not been explored so far as additive for this application. We propose to use ionic liquids to guide the morphology in solution as a result of block-solvent thermodynamic interactions, coulombic and hydrogen-bond interactions mainly between ionic liquids and pyridine. By immersion in water, the solvent non-solvent (water) exchange should kinetically trap the order to manufacture asymmetric porous membranes.

3.2 Experimental section

3.2.1 Materials

Polystyrene-*b*-poly (4-vinylpyridine) block copolymer P10900-S4VP (PS-*b*-P4VP 188,000-*b*-64,000 g/mol) was purchased from Polymer Source, Inc., Canada. Dimethyl formamide (DMF) and Tetrahydofuran (THF) was supplied by Fisher Scientific. 1-methyl imidazole and sulphuric acid were purchased from Sigma Aldrich. ILs such as 1-Butyl-4-methylpyridinium tetrafluoroborate ([B4MPy][BF4]) (≥97% purity), N-Butyl-3-methylpyridinium trifluoromethanesulfonate ([B3MPy][TFMS]) (98% purity), 1-Ethyl-3-methyl imidazolium tetrafluoroborate ([EMIM][BF4]) (≥97% purity), 1-Butyl-3-methylimidazolium tetrafluoroborate ([B3MIM][BF4]) (≥98% purity) were purchased from Sigma Aldrich and Merck; they were used as received. Imidazolium bistrifluoro methane sulphonimide ([IM][TFSI]) and 1-methylimidazolium bisulfate ([HMIM][HSO_4]) were synthesized by previously reported procedure.[14,37] The monomer Imidazole was purified by sublimation under vacuum before the [IM][TFSI] was prepared.

3.2.2 Membrane Preparation

All the membranes were prepared using 17.4 to 18.0 wt% block copolymer solutions in a mixture of IL/ DMF/ THF. Different types of ionic liquids were mixed to the solution and stirred at room temperature for 24 h. The block copolymer solutions were cast on a glass plate using a casting knife with 200 μm air gap. The solvent was allowed to evaporate for different times and the films were immersed in water at room temperature.

3.2.3 ATR-FTIR

Perkin-Elmer 100 ATR-FTIR spectrometer was used for recording the IR spectra of block copolymer membrane. Data were collected over 16 scans with a resolution of 4 cm^{-1}. The ATR-FTIR measurements were made at room temperature, using an ATR unit at a nominal incident angle of 45^{o}.

3.2.4 Transmission Electron Microscopy

The cross section of the membranes was imaged using TEM. All the membranes were embedded in a low-viscosity epoxy resin (Agar R1165) and cured at 60^{o}C for 24 h. Ultrathin sections (80 nm) were prepared with an ultramicrotome (Leica EM UC6) and placed on a carbon-coated copper grid. Images were obtained on a Tecnai 12 (FEI) operating at 120 keV. Most samples were stained with RuO4 vapors before imaging to increase contrast. An additional membrane prepared from solutions containing [B3MIM][BF4] was stained with methyl iodide (CH_3I). TEM tomography was performed for one of the samples.

3.2.5 Field Emission Scanning Electron Microscopy (FESEM)

Micrographs of membranes were obtained using a FEI Quanta 600 Field Emission Scanning Electron Microscope. Imaging was carried out at 5 kV with a working distance of 10 mm. The membrane samples were mounted on aluminum stubs using aluminum tape and Au coated before imaging for 45 s at 20mA.

3.2.6 Cryo- Field Emission Scanning Electron Microscopy

The low temperature FESEM was performed using a FEI Nova Nano 630 SEM with a field emission electron source through the lens electron detector. A small amount of block copolymer /ILs solution mixture was placed between two rivets and was then cryo quenched by rapidly plunging into liquid nitrogen at -180^0C. The sample was then transferred to a SEM cryo- stage, which was held at -115^oC. Then the sample was sputter coated with 5 nm thick platinum in an argon atmosphere inside the cold chamber and high resolution FESEM images were captured. Detailed procedure reported elsewhere.[32,38]

3.2.7 Rheology

Rheological measurements were carried out at 25^0 C with AR- 1500 ES Rheometer with cone and plate fixture of diameter 25 mm and a cone angle of 1^0. The rheology measurements were performed in the linear viscoelastic region. The range of shear rates used for the viscosity measurements is 10-1000 s^{-1}. All tested solutions had 17.4 to 18 wt % copolymer. Except for solutions containing [IM][TFSI], all solutions had 3.8 wt % ionic liquid/ 31 wt% THF/ 48 wt% DMF. In the case of [IM][TFSI] and [HMIM][HSO_4] the copolymer was dissolved in 1.2 wt % IL/ 32 wt% THF/ 49 wt% DMF. Larger [IM][TFSI]

concentration led to gelation. Larger concentration of [HMIM][HSO_4] led to phase separation.

3.2.8 Water Flux Measurement

Pure water fluxes of membranes were measured using a stirred Amicon dead-end ultrafilitration cell at 1 bar. The membranes for flux measurements were prepared on a nonwoven polyester support. Effective membrane area was 5 cm^2. Deionized water was used for water flux measurements.

3.3 Results and Discussion

3.3.1 Membrane preparation

Different types of ILs shown in Scheme 3.1 were added as an additive/cosolvent to guide the assembly of PS-*b*-P4VP copolymers in THF/DMF solutions. When used as casting solutions for the manufacture of membranes by phase inversion in water baths, no regular pore structures were observed with the 188,000-*b*-64,000 g/mol PS-*b*-P4VP without addition of ILs. The ILs evaluated so far strongly interact with the copolymer, but are not capable to dissolve PS-*b*-P4VP with Mw.188,000-*b*-64,000 g/mol as single solvent. Gelation or phase separation was observed in some cases even at IL concentrations higher than used here. On the other hand we observe that even small amounts of ILs with different chemical structures can be very useful to tune the membrane morphology. The block copolymer solutions were cast on glass plates and allowed to evaporate in different time periods before immersion in water. The incipient membrane on the glass plate was immersed in water. During this process solvent-water exchange occurs, the solvent and ILs

migrate from the block copolymer solution to the water bath. Water penetrates the solution, leading to an unstable thermodynamic condition.

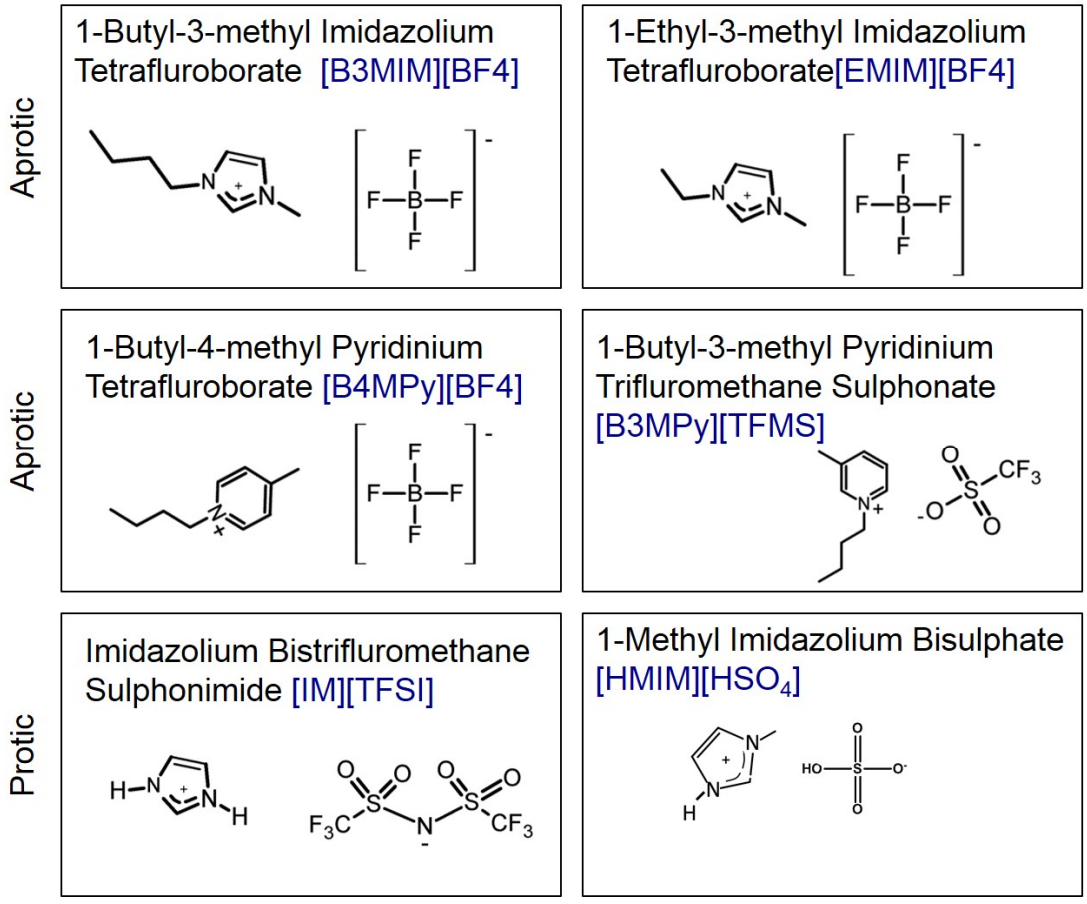

Figure 3.1 Chemical structures of the aprotics ([B3MIM][BF4], [EMIM][BF4], [B4MPy][BF4], [B3MPy][TFMS]) and protic ([IM][TFSI], [HMIM][HSO4]) ILs used for membrane preparation.

The introduction of water abruptly decreases the solvent quality and kinetically traps the order previously achieved in solution, leading to the formation of smaller regular pores at the membrane top layer. Microphase separation proceeds in deeper layers. The phase with lower concentration of copolymer leads to pore formation with increasing size across the membrane. An asymmetric structure if finally observed. The combination of a more classical phase separation mechanism and copolymer self-assembly has been discussed in

previous publications without the presence of ionic liquids.[30-34] The addition of ionic liquids affected the final membrane morphology, Being soluble in water, the IL is washed out. No IL residue was detected by FTIR spectroscopy after washing with water for 3-4 times repeatedly during 24 h and dried.

3.3.2 Membrane Morphology

We used protic ([IM][TFSI], [HMIM][HSO4]) and aprotic ([B4MPy][BF4], [B3MPy][TFMS], [EMIM][BF4], [B3MIM][BF4]) ionic liquids as additives. Figure 3.2 shows membranes prepared with various concentrations of the aprotic [B4MPy][BF4]. Figure 3.2a is the control, PS-*b*-P4VP membrane manufactured from solutions in DMF/THF without ionic liquid. Although Peinemann et al.[29] reported isoporous membranes obtained from PS-*b*-P4VP in DMF/THF an analogous ordered structure could not be obtained with other copolymer molecular weights investigated by our group, including the 188,000-*b*-64,000 copolymer used in this work. As the IL concentration increases from 1.8 wt% to 5.1 wt% (Figure 3.3 b-d) the morphology changes. Solutions containing 3.8 wt% IL have an optimized pore structure (Figure 3.2c). With further IL concentration increase to 5.1% the pores become elongated; 1.8 wt % IL facilitates the micelle self-assembly but was not enough to induce the needed order. This indicates that the concentration of [B4MPy][BF4] contents plays a vital role in the final membrane morphology.

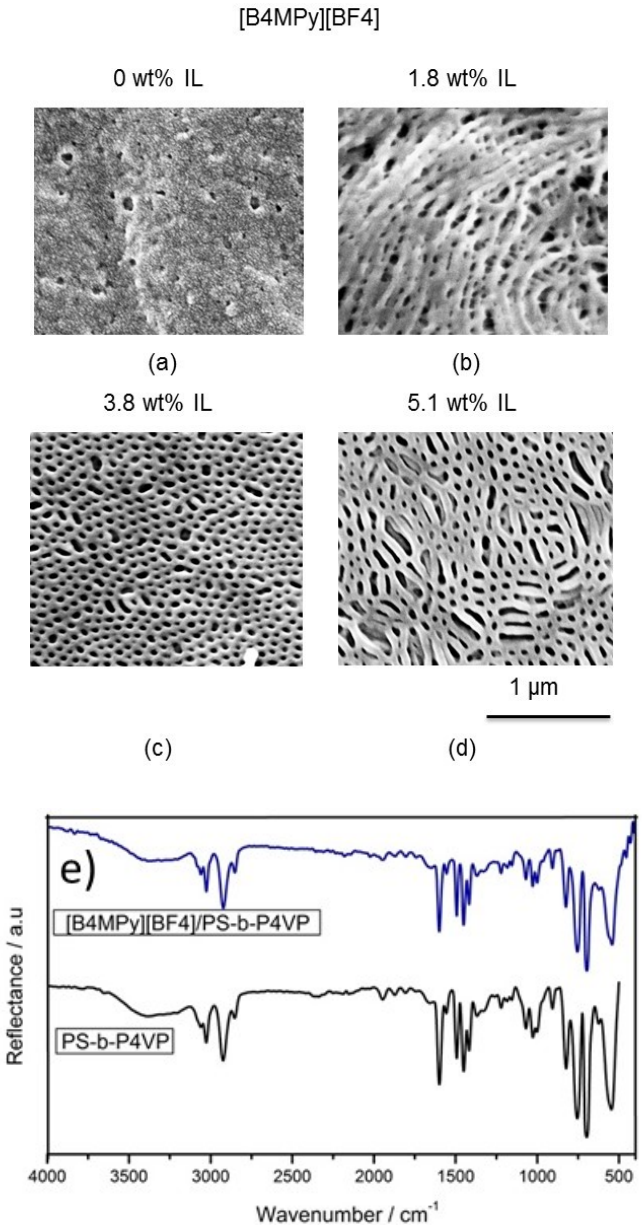

Figure 3.2 Membranes prepared from (a) 18 wt% PS-*b*-P4VP solutions in 32 wt% THF/ 50 wt% DMF; (b) 18 % PS-b-P4VP solutions in 1.8 wt% [B4MPy][BF4]/ 31 wt% THF/ 49 wt% DMF; (c) 17.4 wt % PS-b-P4VP solutions in 3.8 wt% [B4MPy][BF4]/ 31 wt% THF/ 48 wt% DMF; (d) 17.4 wt % PS-b-P4VP solutions in 5.1 wt% [B4MPy][BF4]/ 30 wt % % THF/ 47 wt % DMF. The evaporation time was 20 s. e) ATR-FTIR spectrum of a PS-*b*-P4VP copolymer membrane and analogous membrane prepared with [B4MPy][BF4] as additive

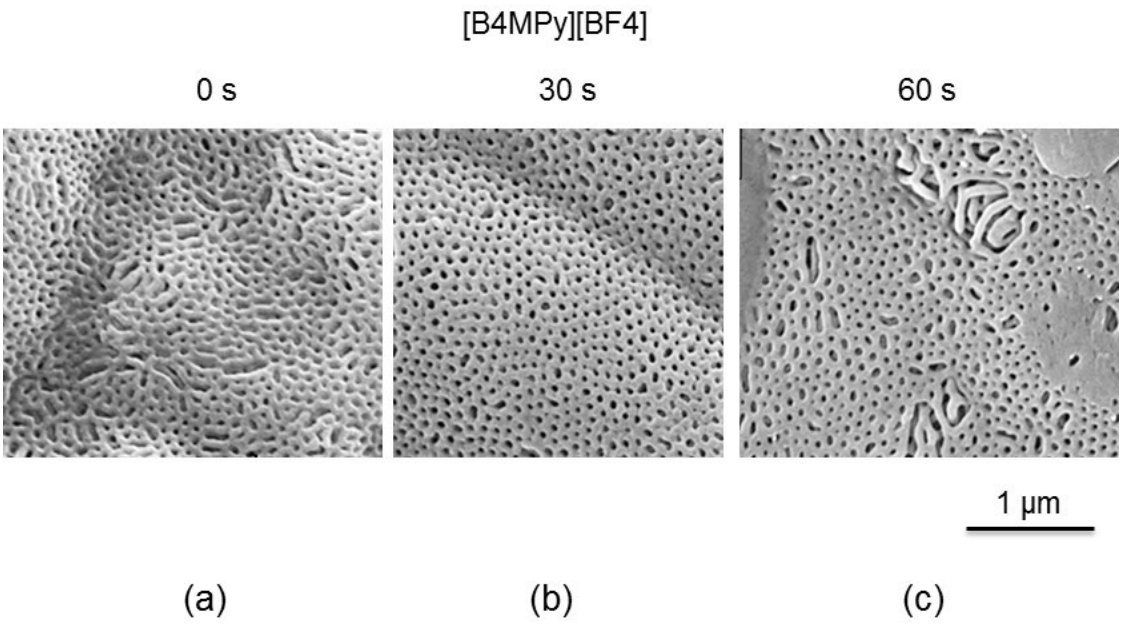

Figure 3.3 Membranes from 17.4 wt % PS-*b*-P4VP solutions in 31 wt% THF/ 48. wt% DMF with 3.8 wt % [B4MPy][BF4], prepared with different evaporation times: (a) 0s, (b) 30s, and (c) 60s.

We have earlier explained the formation of block copolymer membranes from PS-*b*-P4VP solutions in selective solvents (THF/DMF) with complexing salts (Cu^{2+}). It starts with the copolymer micellization with an inner core of PS block and P4VP block as corona, which strongly interacts with the dissolved cation.[31] A supramolecular assembly of block copolymer micelles is responsible for the final membrane morphology in the top layer of the membranes. In this work the IL also preferentially interacts with the pyridine blocks. The polar [B4MPy][BF4] solvates the basic nitrogen atoms of pyridine, keeping the micelles formed in solution intact in a hexagonal arrangement, which leads to the ordered membrane pore structure.

To study the effect of evaporation time during the membrane formation, the membranes were prepared with 3.8 wt % [B4MPy][BF4] with various evaporation times ranging from

0 s to 60 s respectively. The resulting FESEM images are shown in Figure 3.3. The most regular pores were obtained with 20-30 s (Figure 3.3b) evaporation time. Longer evaporation led to heterogeneous morphology.

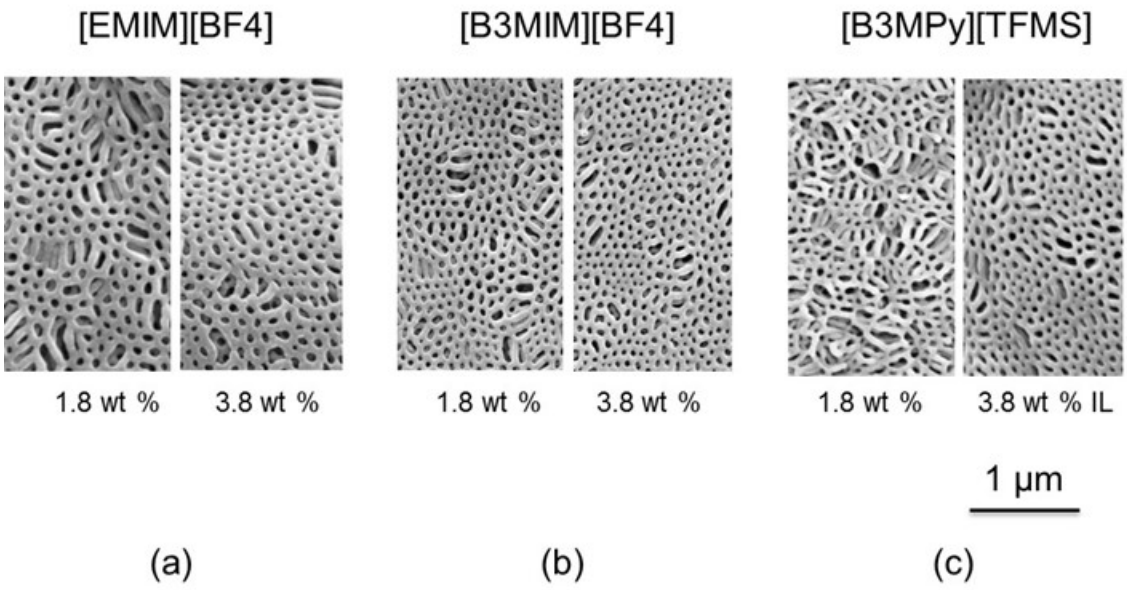

Figure 3.4 Membranes from 17.8 wt% PS-*b*-P4VP solutions in 31 wt% THF/ 49 wt% DMF with 1.8 or 3.8 wt % IL. Aprotic ionic liquids: (a) [EMIM] [BF4], (b) [B3MIM][BF4] and (c) [B3MPy][TFMS]. The evaporation time was 10s.

Similarly to [B4MPy][BF4], we tested ILs with a different substituted pyridinium, [B3MPy][TFMS] and different imidazolium functionalizations as cation, [EMIM][BF4], [B3MIM][BF4], all aprotics. The comparison for two concentrations (1.8 and 3.8 wt %) can be seen also in Figure 3.4. When 3.8 wt% was added, all ILs referred in Figure 3.4 led to ordered pores tending to hexagonal pore geometry. The image for [B3MIM][BF4] shows slightly better order (Figure 3.4b). [EMIM][BF4] led to larger pores (Figure 3.4a). The most evident difference could be seen in Figure 3.4c with addition of 1.8 wt% [B3MPy][TFMS], which has a different anion than the other ILs in Figure 3.4. While BF_4^-

is completely symmetric, TFMS is an asymmetric anion. Also the cation, B3MPy, is less symmetric than B4MPy.

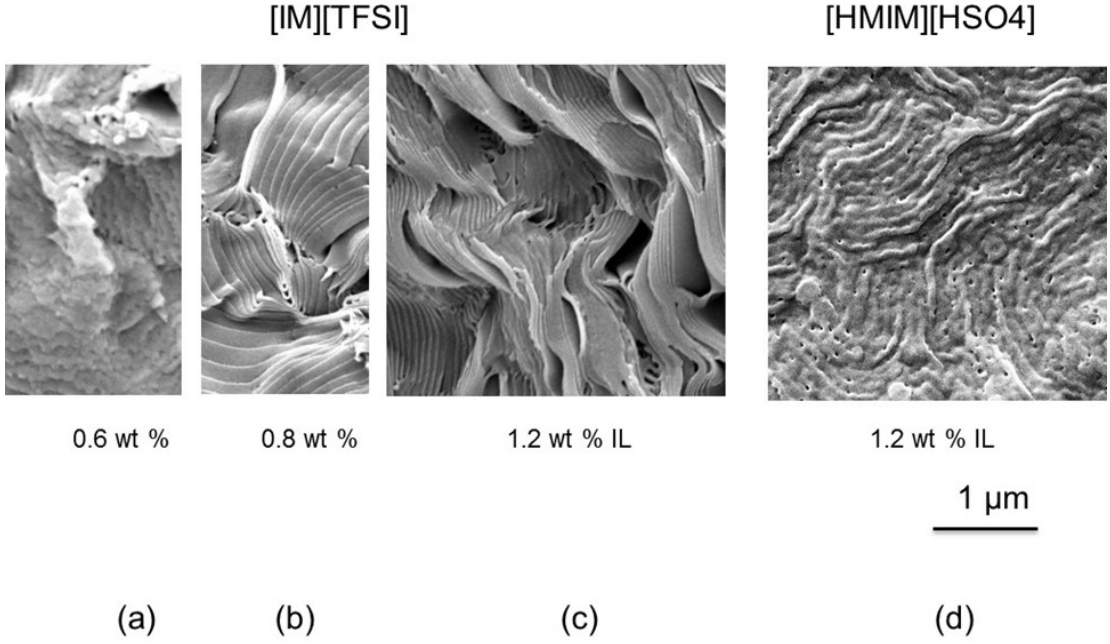

Figure 3.5 Membranes prepared from 17.8 wt% PS-*b*-P4VP solutions in 32 wt% THF/ 49 wt% DMF and (a) 0.6 wt%, (b) 0.8 wt%, (c) 1.2 wt% [IM][TFSI] or (d) 1.2 wt% [HMIM][HSO4]. The evaporation time was 10s.

This shows that all the above aprotic ILs having both the pyridinium and imidazolium cation group favor the formation of hexagonal pores during the membrane preparation if the IL concentration is high enough. However when the protic ionic liquids, [IM][TFSI] and [HMIM][HSO4], were added to the block copolymer solution, only lamellar morphologies were observed, for all investigated IL concentrations (0.6-1.2 wt %) as seen in Figure 3.5 (a-d). Solutions of poly (styrene-block-2-vinylpyridine) copolymer in [IM][TFSI] have been reported to have lamellar geometry, when studied by small-angle X-ray scattering (SAXS).[14, 19, 20] A large change in the domain spacing upon addition of a small amount of ionic liquid has been detected. [IM][TFSI] selectively solvates the PVP

block. The imidazolium group interacts with PVP and protonates it, promoting strong interactions between protonated 2VP moieties and the TFSI anion. It is clear that the [IM][TFSI] IL behaves both as a solvent and salt. [HMIM][HSO4], another protic IL, led also to a lamellar morphology (Figure 3.5d) similar to [IM][TFSI]. The interactions in the case of protic ionic liquids were strong enough to promote macroscopic phase separation ([HMIM][HSO4]) at high IL concentration. For all other ILs both the imidazolium group and the pyridinium groups are non protic, apparently with weaker interaction with the P4VP blocks.

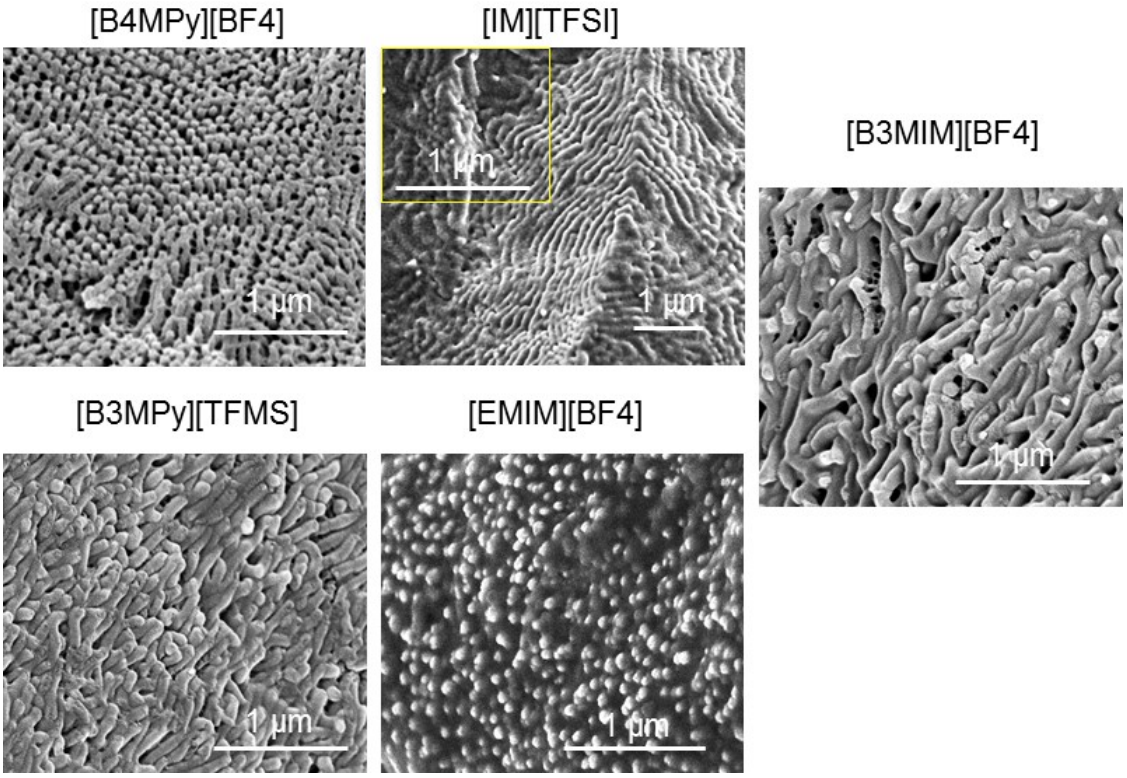

Figure 3.6 Cryo FESEM images of 17.4 wt% PS-*b*-P4VP solutions in 31 wt% THF/ 48 wt% DMF with 3.8 wt % [B4MPy][BF4], [EMIM][BF4], [B3MPy][TFMS], [B3MIM][BF4]; 17.8 wt % PS-b-P4VP solution in 32 wt% THF/ 49 wt% DMF with 1.2 wt % [IM][TFSI].

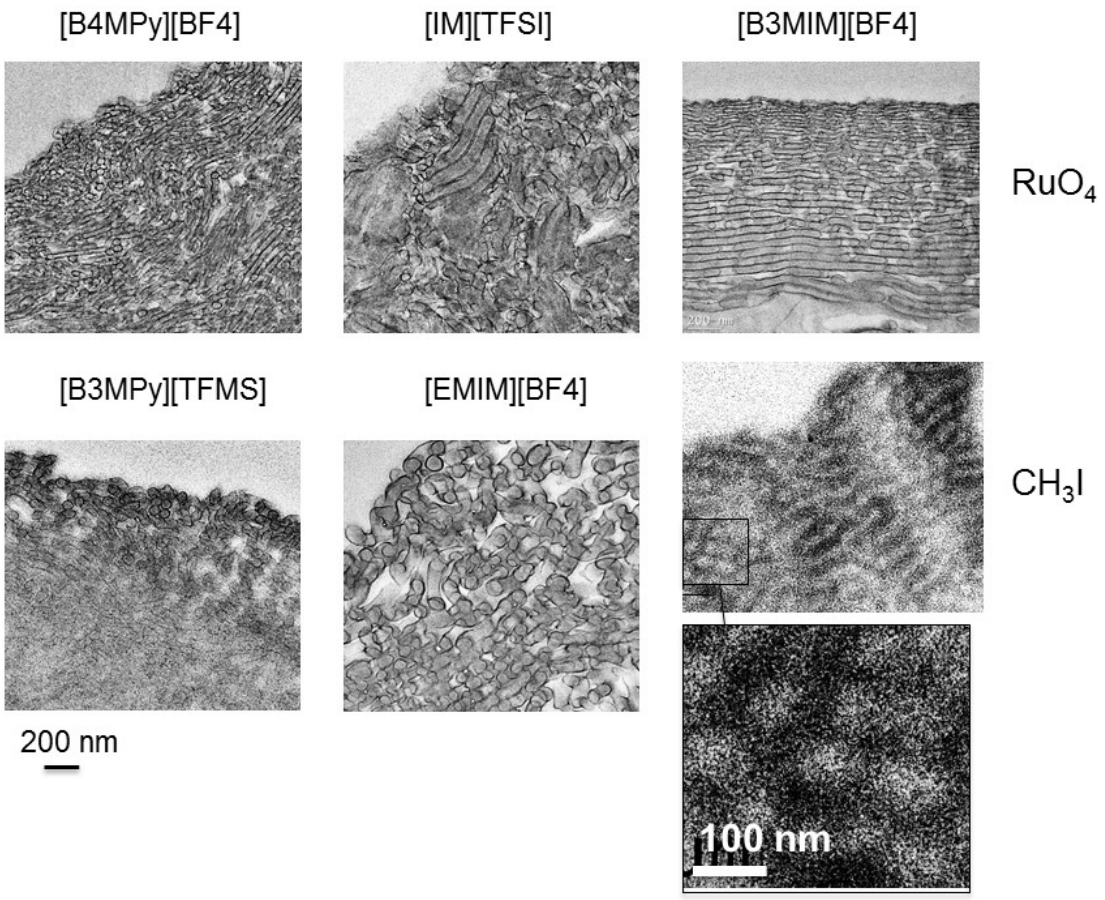

Figure 3.7 TEM cross section images of membranes prepared from 17.4 wt% PS-*b*-P4VP solutions in 31 wt% THF/ 48 wt% DMF with 3.8 wt % [B4MPy][BF4], [EMIM][BF4], [B3MPy][TFMS], [B3MIM][BF4]; 17.8 wt % PS-b-P4VP solution in 32 wt% THF/ 49 wt% DMF with 1.2 wt % [IM][TFSI]. All stained with RuO_4, except for [B3MIM][BF4], which was stained both by RuO_4 (top) and CH_3I (bottom).

To get further insight into the effect of ILs on final membrane morphological details, we investigated the block copolymer /ILs solutions by cryo scanning electron microscopy. Figure 3.6 shows the cryo FESEM images of block copolymer solutions in DMF/THF, containing different ILs. We have previously demonstrated how micelles self-assemble in

solution prior to immersion in water [20] for membrane formation. The cryo FESEM image of the solutions clearly depicts the spherical micelle formation and their ordering pattern in the solution state. Figure 3.6 shows a very well ordered pattern of micelles for the ([B4MPy] [BF4])/ block copolymer solution, which directs the final membrane morphology into the hexagonal ordered porous structure shown in Figure 3.3. In the case of ([IM][TFSI])/ block copolymer solutions the spherical micelles form strings, which leads to a lamellar morphology after the phase inversion in water as in Figure 3.3.

Membrane cross sections were microtomed and imaged using TEM, the cross sectional TEM images of all ILs/ block copolymer membranes are shown in Figure 3.7. For [IM][TFSI], lamellar or cylindrical arrangements are clearly seen but the general order is smaller. The best order is seen by TEM for [B3MIM][BF4]. However cylindrical or lamellar structures are observed apparently parallel to the membrane surface. This would not be consistent with the regular pores imaged in Figure 3.4b. We performed therefore the TEM tomography shown in Figure 3.8. By tilting the membrane slice, we see that they are rather worm-like with an arrangement, which leads to the pore formation on the surface. This morphology can be also well correlated to the order observed in solution, imaged by cryo microscopy and shown in Figure 3.6. The membrane has high water flux, as shown in Table 3.1, again demonstrating high porosity. RuO4 increases the contrast and it is known to stain both PS and P4VP [39, 40]. By taking into account that P4VP is the shorter block (PS 188,000 g/mol, P4VP 64,000 g/mol) the darker regions in Figure 3.7 should correspond to P4VP. For [B3MIM][BF4] the TEM was repeated, staining with CH_3I, which preferentially stains only P4VP. A higher magnification of the CH_3I stained image is shown in Figure 3.7, revealing areas with brighter PS cores surrounded by darker P4VP

coronas. The micelles assemble into strings with cores partially merged into the cylindrical or worm-like structures seen also with RuO_4 staining.

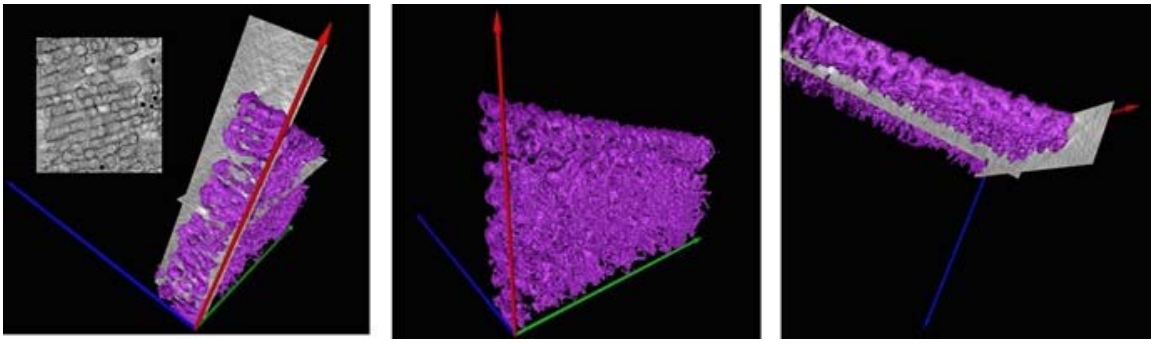

Figure 3.8 TEM tomography (different tilting angles) of membranes prepared from 17.4 wt% PS-*b*-P4VP solutions in 31 wt% THF/ 48 wt% DMF with 3.8 wt % [B3MIM][BF4].

The morphological analysis proves that ILs chemical structure, particularly its capability of forming hydrogen bonds or protonating pyridine, and the added concentration play important roles in the self-assembly and membrane formation.

A simplistic approach would be the estimation of solubility parameters, in analogy to organic solvents. For instance for [B3MIM][BF4] a solubility parameter of 16.2 cal $^{0.5}$ cm$^{-1.5}$ has been estimated by Swiderski et al.[41] placed between water 23.4 cal $^{0.5}$ cm$^{-1.5}$ and THF 9.1 cal$^{0.5}$cm$^{-1.5}$. However the solubility parameter alone might be oversimplified, since it does not take into consideration strong directional interactions such as coulombic, hydrogen-bonding and π-π interactions, which are important for ionic liquids and can contribute to structure-forming solvation and self-assembly. Protic IL can even protonate pyridine. The anions can influence in different extents. BF4 anion is known to have strong hydrogen bond acceptor ability, low polarizability and has the highest symmetry of all IL anions investigated here.

3.3.3 Rheology of block copolymer solution

In order to better understand the effect of the IL on the final membrane morphology, the rheological behavior of IL/ block copolymer solutions was investigated. The rheology of ionic liquids like [B3MIM][BF4] or [B3MIM][Cl] in DMF solutions (without copolymer) was investigated by Wang[42] and Attri et al[43]. Negative excess molar volumes have been detected for [B3MIM][BF4], suggesting that effective packing and attractive interactions are present. DMF has resonance structures characterized by a negative pole in the oxygen atom, which make it a very good hydrogen bond acceptor. Hydrogen bond can be formed with the alkyl chain IL cation. Furthermore ion-dipole interactions between DMF and the [B3MIM][BF4] ions are also possible. Depending on the IL concentration the hydrogen bonds between [B3MIM][BF4] and DMF becomes less relevant. At high [B3MIM][BF4] concentration self-association through hydrogen bonding or ion-ion interaction can also take place.

Pyridine is also a good hydrogen bond acceptor and strongly interacts with hydrogen bond-forming IL cations, particularly those with protic character. Figure 3.9 shows how the viscosity of 17.4 wt % PS-*b*-P4VP copolymer solutions in 31 wt% THF and 48 wt% DMF changes with addition of 3.8 wt% ionic liquids and with shear rate. The effect of different ILs is compared. Except for [HMIM][HSO4], the addition of IL increases the viscosity at low shear rates. Turbidity was observed for solutions with [HMIM][HSO_4] in this concentration range, indicating that phase separation takes place, explaining the low viscosity. All solutions had a shear-thinning behavior. For the block copolymer sample without IL, an accentuated viscosity decay occurs already below 20 s^{-1} and becomes practically constant until 200 s^{-1}, passing through an almost Newtonian regime, probably

corresponding to the flow of disconnected spherical micelles. The viscosity at low shear rate is highly influenced by the soft interaction between micelle coronas. Higher viscosity values in the presence of IL indicate that the ILs improves the linking between the crew cut micelles, which are formed in DMF/THF. The shear thinning at higher shear rate values might be more related to micelle deformation and alignment under stress. Higher viscosity than solutions without IL indicates a stronger connectivity between micelles, favored by stronger interaction between IL and pyridine.

Among solutions containing aprotic ILs, the largest viscosity was measured with addition of [B3MIM][BF4]. At high shear rates the viscosity difference between solutions containing aprotic ILs is small. A clear difference was observed when measuring the storage and loss moduli as a function of angular frequency or oscillation strain (Figure 3.10). Particularly the storage moduli of solutions with [B3MIM][BF4] and [B3MPy][TFMS] are more than 10-fold larger than that of solutions with [EMIM][BF4] or [B4MPy][BF4]. Figure 3.11 shows analogous curves for storage and loss moduli of solutions without ILs or with protic ILs. The storage modulus for solutions without IL is similar to that with [B4MPy][BF4]. For all systems shown in Figure 3.10 and for the system without IL the storage modulus was larger than the loss modulus, at least in angular frequencies up to 200 rad s^{-1}, indicating high elastic contribution. For [B3MIM][BF4] and [B3MPy][TFMS] the storage modulus remain larger than the loss in all investigated angular frequency range, indicating a strong elastic contribution and a stable tridimensional micelle network.

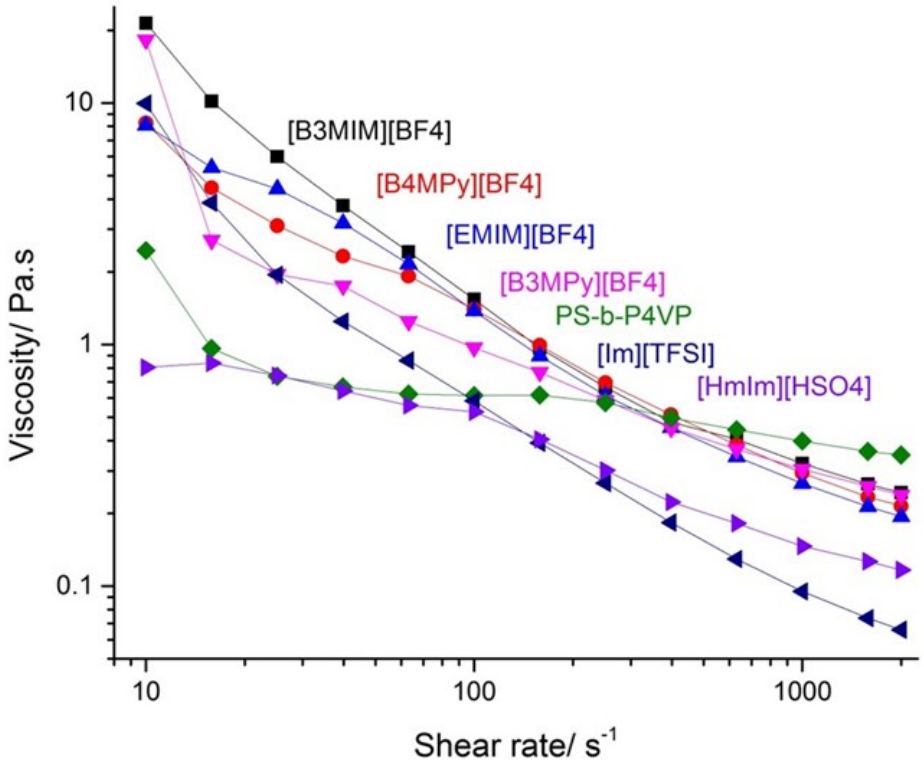

Figure 3.9 Plots of viscosity vs shear rate for 17.4 wt % PS-*b*-P4VP copolymer solutions in 31 wt% THF, 48 wt% DMF, containing 3.8 wt % % aprotic ionic liquids, [B4MPy][BF4], [EMIM][BF4], [B3MPy][TFMS] or [B3MIM][BF4]; and protic ionic liquids [IM][TFSI] or. [HMIM][HSO_4].

We recently reported [34] a rheological investigation proposing how curves of storage and loss moduli could be correlated to intermicellar connectivity. High storage modulus values are related to strongly connected micelles, forming a gel-like tridimensional network, similar to what is observed for solutions with [B3MIM][BF4] and [B3MPy][TFMS]. At high angular frequency, the micelle network disrupts and the micelles align to the shear direction, reducing the storage modulus to values similar to or smaller than the loss modulus. The gel behaves then like a fluid.

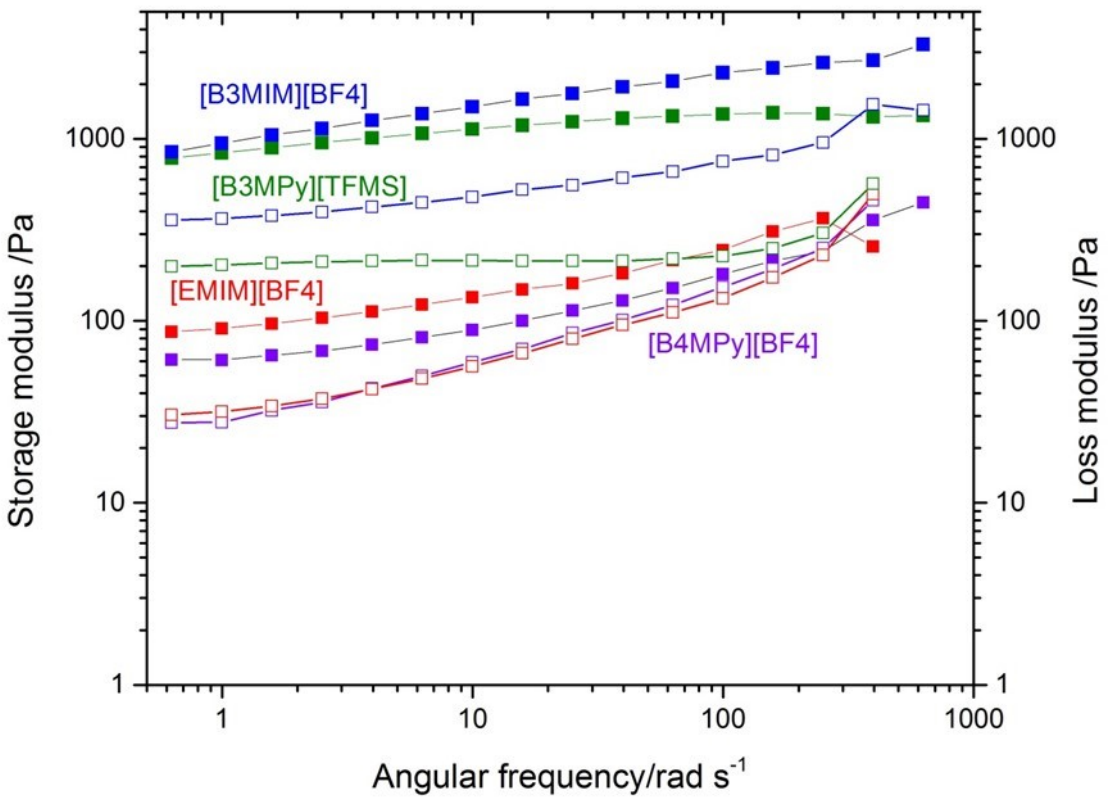

Figure 3.10 Plots of (□) storage and (☐) loss moduli vs angular frequency for 17.4 wt % PS-*b*-P4VP copolymer solutions in 31 wt% THF/ 48 wt% DMF, containing 3.8 wt % aprotic ionic liquids, [B4MPy][BF4], [EMIM][BF4], [B3MIM][BF4] and [B3MPy][TFMS].

Solutions with protic ionic liquids with similar concentrations have much lower storage moduli (<20 Pa). The storage modulus decreases even more with angular frequency and becomes smaller than the loss modulus between 3 and 10 rad s^{-1}. For these systems turbidity started to be observed at this IL concentration. This is an indication of macrophase separation. Homogeneous membranes could be prepared only with solutions containing up to 1.2 wt % IL. Solutions with 1.2 wt % [IM][TFSI] had storage modulus close to 100 Pa at low angular frequency range, higher than the 3.8 wt% solution. The strong interaction between [IM][TFSI] and the copolymer probably might lead to aggregation and further to

phase separation. Phase separation with a copolymer concentrated phase dispersed in a diluted phase (rich in solvents) would explain the low storage moduli.

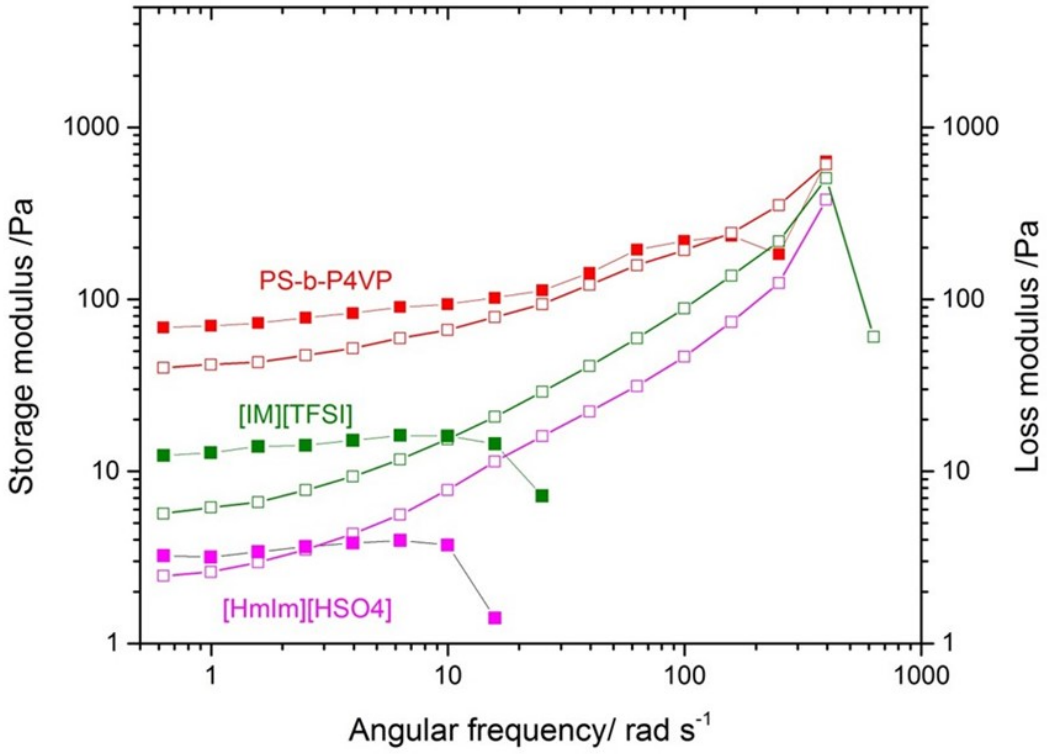

Figure 3.11 Plots of storage and loss moduli vs angular frequency for 17.4 wt % PS-b-P4VP solutions in 31 wt% THF/ 48 wt% DMF containing 3.8 wt % protic ionic liquids [IM][TFSI], [HMIM][HSO4]; analogous PS-b-P4VP solution without ionic liquid.

Hoarfros et al.[44, 45] reported that [IM][TFSI] highly protonates the P2VP block when the PS-*b*-P2VP mixed with [IM][TFSI]. A strong interaction is expected to take place also with the P4VP block in this work, since P4VP is also basic in nature and susceptible to protonation If the [IM][TFSI] concentration is low aggregation is moderate. The micelles assembly in strings, worm-like or lamellar structures in solution, as shown in cryo images depicted in Figure 3.6. With immersion in water the lamella morphology is kinetically trapped giving rise to the membranes shown in Figure 3.5.

The protic ionic liquid [HMIM][HSO4] also led to membranes with lamellar structures, with strong protonation of pyridine groups in the copolymer as in the case of [IM][TFSI]. The loss modulus becomes higher than the storage one already at 3 rad s^{-1} angular frequency, as shown in Figure 3.11, indicating a liquid-like behavior. Probably the addition of [HMIM][HSO4] led also to the formation of micelle aggregates, which flow under conditions close to complete phase separation

In order to understand the reasons for exceptionally high values of viscosity and storage modulus for solutions with aprotic [B3MIM][BF4] we take into consideration previous investigations reported for [B3MIM][BF4] and pyridine single molecules targeting extraction application. Beside hydrogen bonds, coulombic interactions, charge distribution and steric factors are also relevant. Both cations and anions have to be taken in account. Lu et al.[46] investigated the interactions between 1-butyl-3-methylimidazolium tetrafluoroborate ($[B3MIM]^+$), $[BF4]^-$ and pyridine in pyridine/hexane solutions by means of computational analysis using density functional calculations. They considered π (imidazolium) –π (pyridine) interactions with the 2 rings parallel to each other, hydrogen bonds between [B3MIM] [BF4]-pyridine and partial charge transfer, analyzing the maximum electron density (NBO, natural bond orbital analysis) of $[B3MIM]^+$, $[BF4]^-$, pyridine as isolated unities and as interactive $[B3MIM]^+$ $[BF4]^-$ -pyridine system. They found out that for $[B3MIM]^+$ and pyridine rings σ-bonds are formed through overlap of five hybridization orbitals of carbon and nitrogen atoms and delocalized bonds are formed through overlap or the p-orbitals perpendicular to the rings. They calculated the extent of electron delocalization from donors to acceptors as 15.40 kcal/mol in [B3MIM][BF4]-pyridine. The highest occupied molecular orbital (HOMO) and lowest unoccupied

molecular orbital (LUMO) are directly related to ionization potential and electron affinity respectively. The LUMO indicates the capability of a ligand to accept electrons from a donor. For [B3MIM][BF4] HOMO was estimated to be that of occupied p orbitals of F atoms in $[BF4]^-$ and the LUMO was estimated to be the π^* orbitals of imidazolium ring. The HOMO of [B3MIM][BF4]-pyridine is mainly that of pyridine ring, while the LUMO is that of delocalized orbitals of imidazolium ring. They demonstrate that there is no π- π interaction between imidazolium ring and pyridine ring. Pyridine N···H hydrogen bonds are on the other hand very important for the strong interactions between [B3MIM][BF4] and pyridine. There are nine possible hydrogen bonds for [B3MIM] [BF4]-pyridine. The short estimated distances between fluorine and hydrogen atoms indicate also strong H bonds, which involve the anion $[BF4]^-$ as link between pyridine and the ionic liquid cation. The estimated interaction energy reported for [B3MIM] [BF4] -pyridine was 75.9 kJ/mol. The discussion proposed by Lu et al.[46] could be extended to our case to explain the interactions between the pyridine groups of the P4VP copolymer block with [B3MIM] [BF4], guiding morphology and part of the rheological behavior. Anantharaj et al.[47] used mainly HOMO-LUMO energies and the corresponding energy gaps to understand the interaction and availability of ionic liquids to form complexes. Large HOMO-LUMO energy gap implies high stability, being less prone to charge transfer when forming complexes. High IL HOMO indicates willingness in interacting for instance with the external pyridine ring.

Hunt et al.[48] used density functional theory to compare viscosities between [B3MIM]-based compounds and their analog 1-butyl-2,3-dimethyl-imidazolium [BDMIM]–based ionic liquids (not used in our work), which has an additional methyl group and even higher

viscosity. She found out that comparisons between molecular orbitals and differences in electronic densities were not enough and steric factors had to be taken into consideration. ILs usually form a number of stable conformers, frustrating crystal packing, with larger anions forming a larger number of stable ion-pair structures. This characteristics is less pronounced with compact anions like [BF4]. On the other hand, analogously to the arguments used by Hunt et al.[48] for comparing [B3MIM] and [BDMIM], the large butyl substitution in the imidazole ring might reduce ion pair configurational variation, sterically hampering rotation, at least compared to [EMIM][BF4], the ethyl-substituted analog and maybe also compared to other ionic liquids. Fewer stable conformers are possible if rotation is low, leading to lower entropy and a more regular arrangement of ions. This might also facilitate the alkyl chain association, increase viscosity and favor the order observed by TEM in Figures 3.7 and 3.8. Beside the specific interactions discussed above and the steric factors, the tetrahedral symmetry of BF_4^- favors the tridimensional intermicelle network connectivity, more than other anions used in this work, which are asymmetric and less compact.

3.3.4 Water flux measurements

Table 3.1 reports the water flux of membranes prepared with different casting solutions. Water flux measurements were carried out using an Amicon cell at 1 bar N_2 feed pressure. All the membranes have high water flux, ranging from 450 to 1800 L m^{-2} h^{-1} bar^{-1}. IL/ block copolymer membranes having hexagonal pores structure have higher water flux than block copolymer membranes prepared without IL. The [IM] [TFSI]/block copolymer membrane with lamellar structure and low porosity, as shown in Figure 3.5, has low water flux compared to other membranes and a molecular weight cut-off of 50 kg/mol with more

than 95 % retention of 150 kg/mol polyethylene glycol (PEG). Membranes prepared without IL rejected 55 wt% of the same molecular weight PEG; membranes with other ILs rejected 61-66 wt% 150 kg/mol PEG.

Table 3.1 Water flux and structure arrangements of membranes prepared from PS-*b*-P4VP Solutions with various ILs

Ionic Liquids	Membrane morphology	Water flux ($L\ m^{-2}\ h^{-1}\ bar^{-1}$)
No IL	Random spherical, low porosity	1110
[B4MPy][BF4]	Spherical, hexagonal, highly porous	1300
[B3MPy][TFMS]	Spherical hexagonal, highly porous	1600
[EMIM][BF4]	Spherical hexagonal, highly porous	1120
[B3MIM][BF4]	Spherical hexagonal, highly porous	1800
[IM][TFSI]	Lamella	450
[HMIM][HSO_4]	Lamella	550

3.4 REFERENCES

1. Zhang, W; Shi, L; An, Y.; Gao, L.; Wu, K.; Ma, R. *Macromolecules* 2004, 37*,* 2551-2555.

2. Christian, D. A.; Tian, A.; Ellenbroek, W. G.; Levental, I.; Rajagopal, K.; Janmey, P. A.; Liu, A. J.; Baumgart, T.; Discher, D. E. *Nat. Mat.* 2009, 8, 843-849.

3. Kamps, A. C.; Sanchez-Gaytan, B. L.; Hickey, R. J.; Clarke, N.; Fryd, M.; Park., S.-J. *Langmuir* 2010, *26*, 14345–14350.

4. Jo, G.; Ahn, H.; Park, M. J. *ACS Macro Lett.* 2013, *2*, 990–995.

5. Horechyy, A.; Zafeiropoulos, N. E.; Nandan, B.; Formanek, P.; Simon, F.; Kiriy, A.; Stamm, M. *J. Mater. Chem.* 2010, *20,* 7734–7741.

6. Noro, A.; Sageshima, Y.; A., Shigeo; Matsushita, *Macromolecules* 2010, *43,* 5358–5364.

7. Chiu, J. J.; Kim, B. J.; Kramer, Edward J.; Pine, D. J. *J. Am. Chem. Soc.* 2005, *127*, 5036-5037.

8. Zhu, J.; Ferrer, N.; Hayward, R. C. *Soft Matter* 2009, *5,* 2471-2478.

9. Van Zoelen, W.; Asumaa, T.; Ruokolainen, J.; Ikkala, O.; ten Brinke, G. *Macromolecules* 2008, *41,* 3199-3208.

10. Zhong, S.; Cui, H.; Chen, Z.; Wooley, K. L.; Pochan, D. J. *Soft Matter* 2008, *4,* 90–93.

11. Mok, M. M.; Thiagarajan, R.; Flores, M.; Morse, D. C.; Lodge, T. P. *Macromolecules* 2012, *45,* 4818−4829.

12. Zheng, L.; Guo, C.; Wang, J.; Liang, X.; Chen, S.; Ma, J.; Yang, B.; Jiang, Y.; Liu, H. *J. Phys. Chem. B.* 2007, *111*, 1327–1333.

13. Bai, Z.; Zhao, B.; Lodge, T. P. *J. Phys. Chem. B.* 2012, *116,* 8282−8289.

14. Virgili, J. M.; Hexemer, A.; Pople, J. A.; Balsara, N. P.; Segalman, R. A. Phase *Chem. Rev.* 2011, *111,* 3508–3576.

15. Hallett, J. P.; Welton, T. *Chem. Rev.* 2011, 111, 3508–3576.

16. Miranda, D. F.; Russell, T. P.; Watkins, J. J. *Macromolecules* 2010, *43,* 10528–10535.

17. He, Y.; Li, Z.; Simone, P.; Lodge, T. P. *J. Am. Chem. Soc.* 2006, *128,* 2745-2750

18. Gwee, L.; Choib, J.-H.; Winey, K. I.; Elabd, Y. A. *Polymer* 2010 *21,* 5516-5524.

19. Virgili, J. M.; Nedoma, A. J.; Segalman, R. A.; Balsara, N. P. *Macromolecules* 2010 *43,* 3750–3756.

20. Virgili, J. M.; Hoarfrost, M. L.; Segalman, R. A. *Macromolecules* 2010, *43,* 5417–5423.

21. Figoli, A.; Marino, T.; Simone, S.; Di Nicolo, E.; Li, X.-M.; Tornaghi, S.; Drioli, E. *Green Chem*. 2014, *16*, 4034-4059.

22. Szekely, G.; Jimenez-Solomon, M. F.; Marchetti, P.; Kim, J. F.; Livingston, A. G. *Green Chem*. 2014, DOI: 10.1039/c4gc00701h.

23. Xing, D. Y.; Peng, N.; Chung, T.-S. *Ind. Eng. Chem. Res.* 2010, *49,* 8761–8769.

24. Xing, D. Y.; Peng, N.; Chung, T.-S. *J. Membr. Sci.* 2011, *3*, 87– 97.

25. Neves, L. A.; Crespo, J. G.; Coelhoso, I. M. J. *Membr. Sci.* 2010, *357*, 160–170.

26. Simons, K.; Nijmeijer, K. ; Bara, J. E.; Noble, R. D. ; Wessling, M*J. Membr. Sci.* 2010, *360*, 202-209.

27. Shishatskiy, S.; Pauls, J. R.; Nunes, S. P.; Peinemann, K. V. *J. Membr. Sci.,* 2010, *359*, 44-53.

28. Schäfer, T.; Rodrigues, C. M.; Afonso, C. A. M.; Crespo, J. G. *Chem. Commun.* 2001, 1622-1623.

29. Peinemann, K. V.; Abetz, V.; Simon, P. F. W. *Nat. Mat.* 2007, 6, 992-996.

30. Nunes, S. P.; Behzad, A. R.; Hooghan, B.; Sougrat, R.; Karunakaran, M.; Pradeep, N.; Vainio, U.; Peinemann, K.-V. *ACS Nano* 2011, *5,* 3516–3522.

31. Nunes, S. P.; Sougrat, R.; Hooghan, B.; Anjum, D. H.; Behzad, A. R.; Zhao, L.; Pradeep, N.; Pinnau, I.; Vainio, U.; Peinemann, K.-V. *Macromolecules* 2010, *43,* 8079–8085

32. Nunes, S. P.; Karunakaran, M.; Neelakanda, P.; Behzad, A. R.;Hooghan, B.; Sougrat, R; He, H.; Peinemann, K.-V. *Langmuir* 2011, 27, 10184-10190.

33. Marques, D. S; Vainio, U.; Chaparro, N. M.; Calo, V. M.; Bezahd, A.R.; Pitera, J.; Peinemann, K. V.; Nunes, S. P. *Soft Matter* 2013, 9, 5557-5564

34. Madhavan, P.; Peinemann, K.-V. ; Nunes, S. P. *ACS Appl. Mater. Interfaces* 2013, *5*, 7152-7159.

35. Phillip, W. A.; Dorin, R. M.; Werner, J.; Hoek, E. M.V.; Wiesner, U.; Elimelech, M. *Nano Lett.* 2011, 11, 2892-2900.

36. Dorin, R. M.; Marques, D. S.; Sai, H.; Vainio, U.; Phillip, W. A.; Peinemann, K. V.; Nunes, S. P.; Wiesner, U.; *ACS Macro Lett.* 2012, 1*,* 614−617.

37. Shukla, S. K.; Khupse, N. D.; Kumar, A. *Phys.Chem.Chem.Phys*. 2012, 14, 2754-2761.33.

38. Marques, D. S.; Dorin, R. M.; Wiesner, U.; Smigies, D.-M.; Behzad, A. R.; Vainio, U.; Peinemann, K.-V.; Nunes, S. P. *Polymer* 2014, *55,* 1327-1332.

39. Trent, J. S.; Scheinbeim, J. I.; Couchman, P. R. *Macromolecules* 1983, *16,* 589-598.

40. Vayer, M.; Nguyen, T. H.; Sinturel, C. *Polymer* 2014, *55,* 1048-1054.

41. Swiderski, K.; McLean, A.; Gordon, C. M.; Vaughan, D. H.; *Chem. Commun.* 2004 2178-2179.

42. Wang, J.; Tian, Y.; Zhao, Y.; Zhuo, K. *Green Chem*. 2013, 5, 618-622.

43. Attri, P.; Reddy, M.; Venkatesu, P.; Kumar, A.; Hofman, T. *J. Phys. Chem. B.* 2010, 114, 6126-6133.

44. Hoarfrost, M. L.; Tyagi, M. S.; Segalman, R. A.; Reimer, J. *Macromolecules* 2012, *45,*3112-2120.

45. Hoarfrost, Megan L.; Segalman, R. A. *Macromolecules*. 2011, *44,* 5281–5288.

46. Lu, R.; Qu, Z.; Yu, H.; Wang, F.; Wang, S. *Chem. Phys. Lett.* 2012, 532, 13-18.

47. Anantharaj, R.; Banerjee, T. *Fluid Phase Equilibria* 2010, *293*, 22-31.

48. Hunt, P. *J. Phys. Chem. B* 2007, *111*, 4844-4853.

CHAPTER 4a

Block Copolymer Hollow Fiber Membranes with Catalytic Activity and pH-Response

Summary

We fabricated block copolymer hollow fiber membranes with self-assembled, shell-side, uniform pore structures. The fibers in these membranes combined pores able to respond to pH and acting as chemical gates that opened above pH 4, and catalytic activity, achieved by the incorporation of gold nanoparticles. We used a dry/wet spinning process to produce the asymmetric hollow fibers and determined the conditions under which the hollow fibers were optimized to create the desired pore morphology and the necessary mechanical stability. To induce ordered micelle assembly in the doped solution, we identified an ideal solvent mixture as confirmed by small-angle x-ray scattering. We then reduced p-nitrophenol with a gold-loaded fiber to confirm the catalytic performance of the membranes.

This chapter was published as*: R. Hilke, N. Pradeep, P. Madhavan ,U. Vainio, Ali Reza Behzad, Rachid Sougrat, Suzana. P. Nunes and Klaus-Viktor Peinemann, Block copolymer Hollow Fiber Membranes with catalytic activity and pH response, ACS Applied materials and Interfaces, 2013, 5(15), pp 7001-7006.

My contribution in this chapter was flat sheet membrane preparation, gold incorporation in all membranes and catalytic testing only.

4a.1 Introduction

We demonstrated that isoporous membranes can be obtained by combining block copolymer micelle assemblies with phase separation by solution casting and immersion in water.[1-3] One advantage of this method is the possibility of exploiting the unique versatility of block copolymers for morphological design, a claim that many groups have made,[4-8] to improve membranes used by industry on the large scale. We are now able to prepare isoporous block copolymer flat-sheet membranes continuously by using non-woven substrates as supports. For many applications, such as artificial kidneys, membrane bioreactors, contactors or specific cases of gas separation, however, hollow fiber membranes rather than flat sheets are preferred,[9, 10] because they have higher surface-to-volume ratios, which allow their integration into compact modules. No support is necessary for hollow fibers. The shear strength during the manufacturing process is much higher.

The principle of fabricating hollow fibers is simple and we have explored the use of many materials and applications for these membranes. The polymer (dope) solution is pressed through a spinneret and collected in a rotating immersion bath filled with water. By simultaneously pressing water or other non-solvent mixtures (bore fluid) from the center of the spinneret, a continuous hollow fiber can be manufactured. The big challenge is to adapt the casting solutions and production conditions to produce fibers with high dimensional stability, while maintaining the isoporous surface structure. We note that the complete formation of the membrane structure must be finished in less than five seconds. This short time is determined by the spinning speed (typically 5 m/min), the air gap length (14 cm in most of our experiments) and the very fast precipitation step. Whereas these conditions are well established for routine hollow fiber spinning, our challenge is that a highly ordered, self-assembled fiber top layer must also be formed in this short period. This

is possible only because we pre-order the micelles in the polymer solution. A new solvent mixture was also needed to produce the hollow fibers and the manufacturing conditions had to be adapted to produce mechanically stable systems that would withstand regular operating conditions.

We recently demonstrated that membranes with exceptionally regular pore sizes and with the ability to respond to pH can be used for separation of similarly sized proteins.[11] Here, we look beyond separation to describe the catalytic capabilities of isoporous hollow fiber membranes that incorporate colloidal gold. The inclusion of gold nanoparticles in block copolymers has been previously reported for the formation of micelles, vesicles and nanofibers with applications in biotechnology and biomedicine, cellular imaging, and nanowires.[12-15] Gold catalysis is relevant to the reduction of highly toxic 4-nitrophenol to 4-aminophenol,[16, 17] which we used as our model reaction to test our novel membranes.

4a.2 Experimental section

4a.2.1 Materials

Polystyrene-b-poly-vinyl pyridine block copolymer samples (number P9828-S4VP (PS-b-P4VP, 175000-b-65000)) were purchased from Polymer Source, Inc, Canada. 1,4 dioxane, acetone, dimethylformamide (DMF), nitric acid, sodium hydroxide, gold tetra chloride and sodium citrate were supplied by Sigma Aldrich and tetrahydrofuran (THF) was supplied by Fischer Scientific. Single wall carbon nanotubes were supplied by Sigma Aldrich.

4a.2.2 Membrane preparation

Flat-sheet membranes were prepared for comparisons. Dope solution 1 was prepared by dissolving 16 wt% block copolymer in a mixture of DMF, THF and 1,4 dioxane of equal weight proportions. The casting solution was stirred over night at room temperature. When

the solution was free from air bubbles it was cast using a doctor blade with a gap of 200μm. The polymer solutions were cast on a glass plate and precipitated in deionized water. Finally, the membranes were rinsed with water and dried at 22 °C. We used a ternary solvent system to improve the order and uniformity of the pores. We dissolved 22 wt% block copolymer in 42 wt% 1,4 dioxane, 20 wt% of DMF and 16 wt% of acetone.

The hollow fiber membranes were produced with a small laboratory spinning apparatus. Both the bore fluid and polymer flow were carefully controlled. The bore fluid was pumped by a HPLC pump (Knauer Scientific Instruments, Germany). A nitrogen pressure-induced flow controlled by a digital thermal mass flow meter (Bronkhorst, El-flow, Germany) regulated the flow of the dope.

Deionized water at a temperature of 22 °C was used for the precipitation bath and as the bore fluid. The nascent fiber entered an air gap between the spinneret and the precipitation bath. The moisture in the air gap was regulated by a laminar flow of nitrogen with a relative humidity of 20% at 22°C into the air gap housing. Finally, the fibers were rinsed for at least two days in deionized water that was renewed daily and then air dried at 22 °C.

4a.2.3 Gold complexation with isoporous membranes

We used two methods to deposit gold nanoparticles on the outer surface of the hollow fiber membranes. In one set of experiments, we first prepared the gold nanoparticles as a dispersion, which was then filtered through the hollow fiber membranes. In a second set of experiments, we filtered a 1 wt% gold chloride solution through the fibers. The adsorbed gold ions were then reduced to elementary gold by pumping a 0.05 M sodium citrate solution through the hollow fiber membranes. We used the model reaction of the reduction of p-nitrophenol[16] to confirm the catalytic activity of the hollow fibers after incorporation with gold.

Gold loading of hollow fiber membranes

Method 2: The hollow fiber membrane was placed in the ultrafiltration set up. 1% aqueous gold chloride trihydrate solution and 0.05M sodium citrate solution was freshly prepared and pumped through the hollow fiber membrane at a pressure of 460 mbar for 24 hrs. Finally the membrane was washed with water to remove any non-reduced gold.

4a.2.4 Field Emission Scanning Electron Microscope (FESEM)

The morphology of the membranes was characterized by a field emission scanning electron microscope (FESEM). The membrane surfaces were imaged with a Nova Nano 630 microscope using a voltage of 5 kV. Prior to the imaging, the samples were sputtered with Pt using a K575X Emitech sputter coater. Secondary and backscattered detectors were also used.

4a.2.5 Transmission Electron Microscope (TEM)

The membranes were cut in a LEICA EM UC6 cryo-ultramicrotome after being embedded in a low viscosity resin and imaged in a Titan FEI transmission electron microscope (TEM) at 300 kV. For clarity in some of the images, the membrane slices were stained with methyl iodide vapor for 4 h before imaging.

4a.2.6 Small-Angle X-Ray Scattering (SAXS)

Casting solutions with different copolymer concentrations and a mixture of DMF/dioxane/acetone were investigated by small-angle x-ray scattering (SAXS) with the B1 beam line of the DORIS III, HASYLAB of the *Deutsches Elektronen-Synchrotron* (DESY) in Hamburg, Germany. The solution was placed into 2 mm diameter quartz capillaries by using a syringe and sealed with epoxy glue. The experiments were performed at $P = 10^{-4}$ mbar using a single-photon counting PILATUS 1M detector (Dectris) placed 3.6 m behind the sample. The x-ray wavelength was 1.764 Å, with a photon flux of

~10^8 photons/s on the sample. The scattering vector magnitude, q, is defined as $q = (4\pi/\lambda) \sin\theta$, where θ is half of the scattering angle.

4a.2.7 Flux measurement

Flux through the flat sheet membranes was measured with an Amicon filtration cell at a pressure of 1 bar. The pH of the feed solution was adjusted by adding nitric acid or sodium hydroxide. Small single fiber modules each containing a fiber about 9 cm in length were used for the flux measurements. pH-adjusted solutions were pumped through the hollow fiber modules by a roller pump (Heidolph, Pumpdrive 5001, Germany) and the pressure was monitored by a digital pressure sensor (Greisinger Electronic, GDH13AN, Germany). A needle valve regulated the pressure.

4a.2.8 Reduction of 4-NP catalyzed by PS-b-P4VP/Au Nps hollow fiber membrane

The prepared PS-b-P4VP hollow fiber membrane with Au NPs was tested for the catalytic activity with the help of the model reaction of reduction of 4-nitrophenol to 4-aminophenol.The reactant solution was prepared by mixing sufficient volumes of the mother solutions containing 1 mM 4-NP and 100 mM NaBH4 and diluting with distilled water. The 1 mM mother solution of 4-nitrophenol was prepared prior and stirred for two hours at room temperature and allowed to rest for five hours to achieve thermal equilibrium. The NaBH4 mother solution is prepared just few minutes before to avoid any kind of decomposition. A Cary 1000 UV/VIS spectrometer was used to determine the concentration of nitrophenolate ion. A calibration curve is constructed to determine the value of ε with the help of Beer-Lambert law. From the mother solutions, samples containing 10 mM NaBH4 and the following concentration of 4-NP were prepared:

0,0.01mM, 0.025 mM , 0.05 mM , 0.075 mM, 0.1 mM, 0.25 mM. The samples absorbance were measured in the 200-600 nm range.

4a.3 Results and discussion

4a.3.1 Surface characterization

Although the formation of isoporous flat-sheet membranes has been demonstrated before with DMF/THF[18] and DMF/THF/dioxane[2], we had to optimize the system to produce hollow fibers with adequate properties and sufficient stability for ultrafiltration.

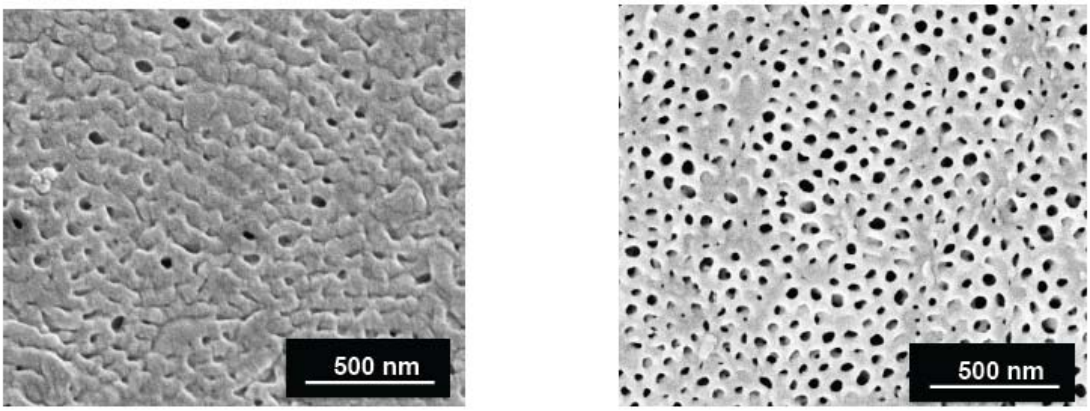

(a) **(b)**

Figure 4a.1 FESEM micrographs of the outer surfaces of the hollow fiber membranes prepared with a 16 wt % copolymer solution in DMF/THF/dioxane with a dope flow of (a) 6 ml/min and (b) 3.4 ml/min.

Our preliminary experiments[19] to develop isoporous PS-*b*-P4VP block copolymer hollow fibers were conducted with 16 wt % DMF/THF/dioxane and DMF/THF. The rates of the polymer (dope) solution flow and the bore flow (water) were 6 ml/min and 1.2 ml/min, respectively.

The morphology of the outer surface of the hollow fibers produced at a flow rate of 6 ml/min is shown in the FESEM image in Figure 4a.1a where it is clear that the pores are mostly closed and the porosity is low. We surmised that the poor surface morphology of

this hollow fiber membrane was caused by the shear rate in the spinneret. We found that it is possible to decrease the shear rate with either a larger annulus in the spinneret or a lower volume flow of polymer solution. We used the lowest possible dope solution flow in the available setup, which we found to be 3.4 ml/min. The improved structure of the outer surface as shown in the SEM image in Figure 4a.1b is the result of the lower shear rate, which allowed us to produce isoporous hollow fibers based on block copolymers[19]. A similar attempt using DMF/THF as the solvent mixture was recently reported by Radjabian et al.[20] No uniform pore size could be obtained although the crucial influence of the shear rate on the pore structure was identified. The surface structure obtained here with DMF/THF/dioxane using a dope flow rate of 3.4 ml/min is certainly more uniform. This observation also confirms our previous findings for flat sheet membranes with dioxane as an additional solvent.[2] However, the fibers produced with solutions containing both DMF and THF are not flexible and can easily break, features that are not acceptable for integration of the fibers into modules or even lab-scale operations. Two methods were investigated to increase the mechanical stability of the fibers: (i) increasing the polymer concentration and (ii) adding carbon nanotubes to the mixture. When we increased the polymer concentration in the DMF/THF/dioxane solvent system, the surface morphology was less ordered, even in the flat-sheet membranes, which we prepared for comparisons. A high polymer concentration can also cause a reduction in the water permeance, a property relevant to many practical applications. We tested other solvent mixtures and found that a 22 wt % copolymer dope solution in the DMF/acetone/dioxane solvent system led to the most uniform flat-sheet membrane surface as shown in Figure 4a.2a. We next spun hollow fibers from 22 wt % copolymer solutions (Figure 4a.2b).

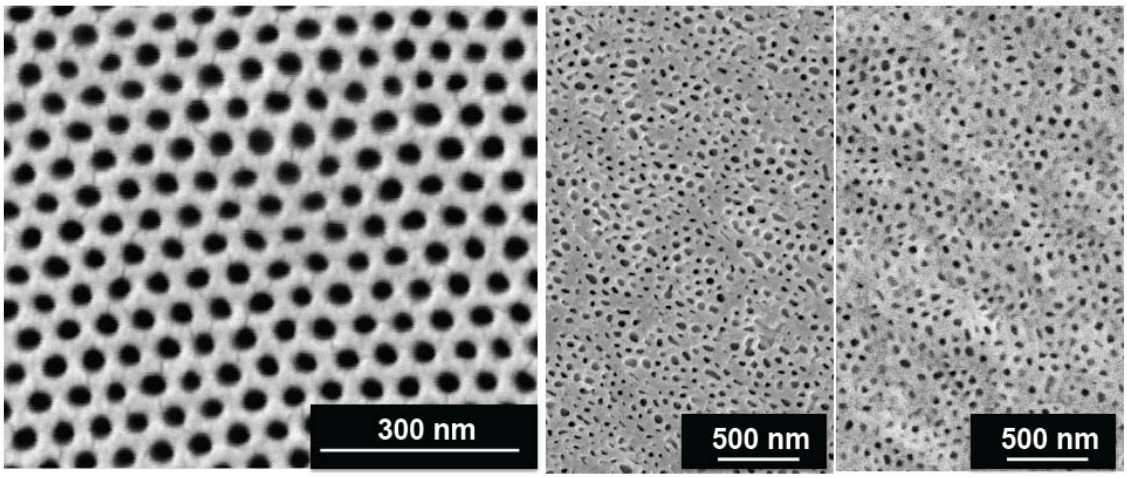

(a) **(b)** **(c)**

Figure 4a.2 FESEM micrographs of the outer surface of (a) a flat-sheet membrane and (b) a hollow fiber made from 22 wt % copolymer solutions in DMF/acetone/dioxane; (c) the outer surface of a hollow fiber prepared from the same solution with the addition of 0.08 wt % carbon nanotubes.

We used the same procedure and added 0.08 wt % carbon nanotubes (Figure 4a.2c). The surface morphologies of the hollow fibers were similar. The mechanical stability of both types of hollow fibers (with and without carbon nanotubes) prepared in the DMF/acetone/dioxane solvent system was similar and it was much higher than that obtained when the hollow fibers were prepared from other solvent mixtures. We therefore conducted further optimization using the 22 wt % polymer solution without carbon nanotubes.

4a.3.2 SAXS characterization

We recently demonstrated[21] that controlling the micelle assembly of block copolymer in solution is essential to the final pore morphology of the membrane. We therefore investigated the order of the PS-b-P4VP in DMF/dioxane/acetone solutions by small-angle

x-ray scattering. The results for different copolymer concentrations are shown in Figure 4a.3.

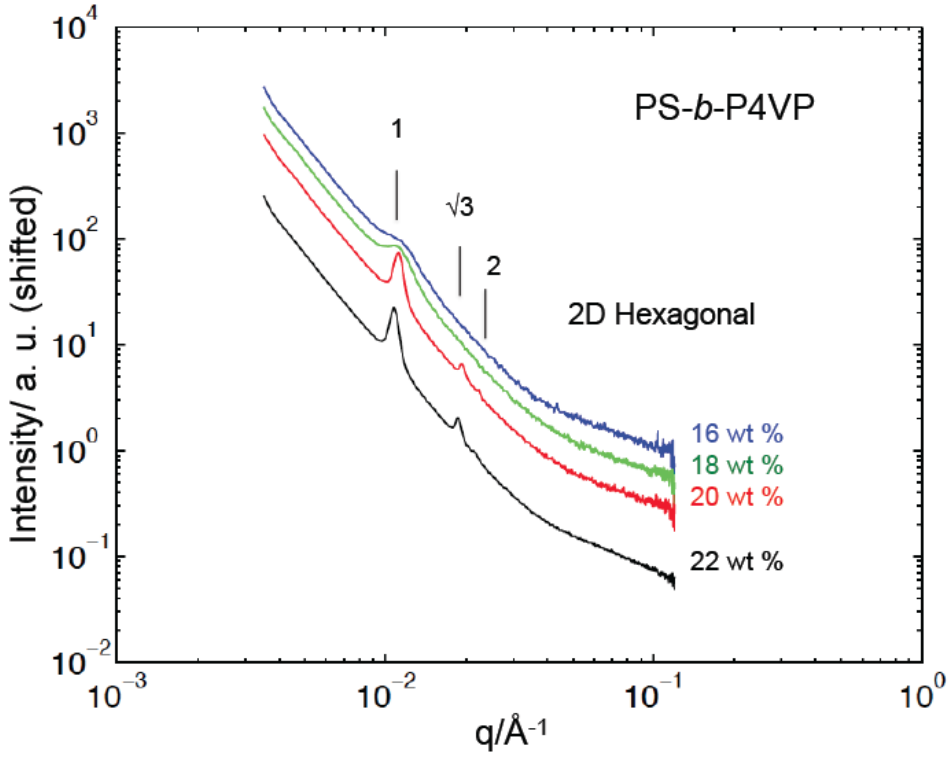

Figure 4a.3 Small-angle x-ray scattering of PS-*b*-P4VP copolymer solutions in DMF/dioxane/acetone.

4a.3.3 Process optimization

The process of making hollow fiber membranes was further optimized with respect to the air gap humidity and length of the membrane and with respect to the bore fluid composition and flow. As noted above, we fixed the dope flow at 3.4 ml/min. A bore flow gave of 2.4 ml/min produced the best results with thin-walled round fibers consistently produced. For our setup, the minimal fiber speed for a continuously spun fiber was 7 cm/sec. We obtained good results with an air gap of 14 cm and a relative humidity of 20%. The resulting

evaporation time of 2 s was short compared with the 10 s evaporation time for the flat sheet membranes. This might be one reason for the prevalence of less uniform pores on the surface of the hollow fibers. We could achieve a porous sponge-like structure without any macrovoids, as shown in Figure 4a.4, with a well-ordered, highly porous outer surface.

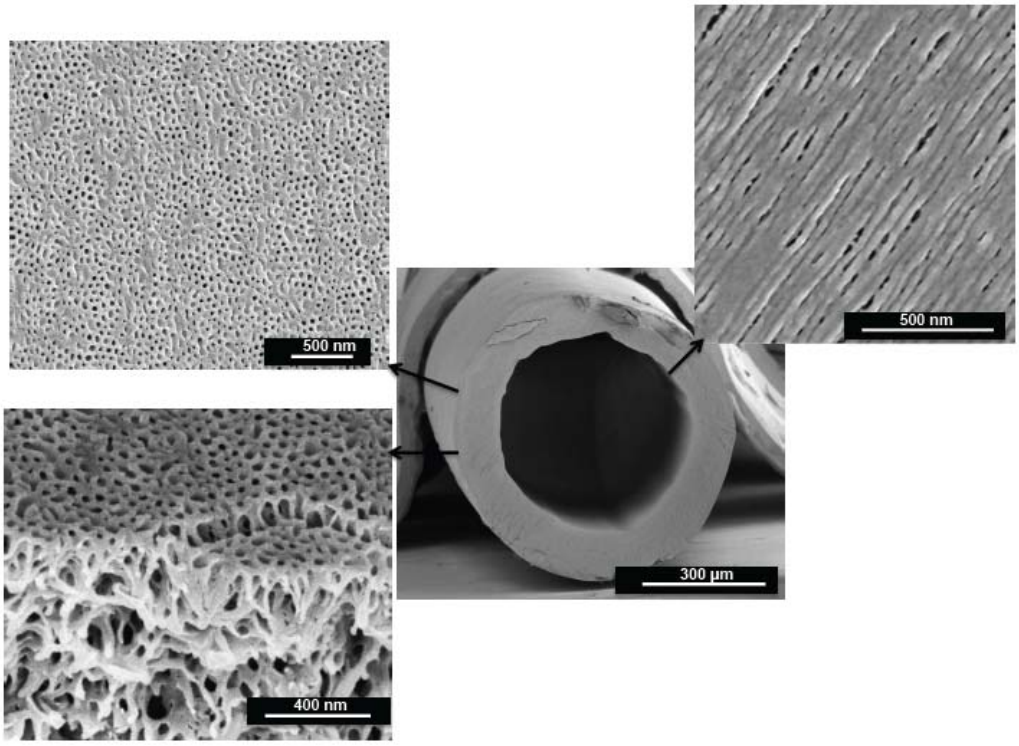

Figure 4a.4 FESEM images of the surface morphology of optimized hollow fibers made from 22 wt % PS-b-P4VP in a DMF/acetone/dioxane solvent system spun with water/DMF bore fluid.

By adding 33 wt % DMF to the bore fluid, we could obtain a more open internal structure, as shown in Figure 4a.4. Moreover, greater than three-fold higher water permeance was achieved by the addition of DMF to the bore fluid (Figure 4a.5).

4a.3.4 Hollow fibers with pH response

We showed earlier that asymmetric flat sheet membranes made from PS-*b*-P4VP exhibited a strong pH response.[1,11] We have now found that PS-*b*-P4VP hollow fiber membranes behave similarly. The water permeance of the hollow fiber membranes was very low when the pH was below 2, whereas a steep but reversible increase in water flux occurred when the pH was around 4 (Figure 4a.5). The pH response of the hollow fiber membranes would be important in biomedical applications because they can be integrated into very small devices, while maintaining the reversible pH response.

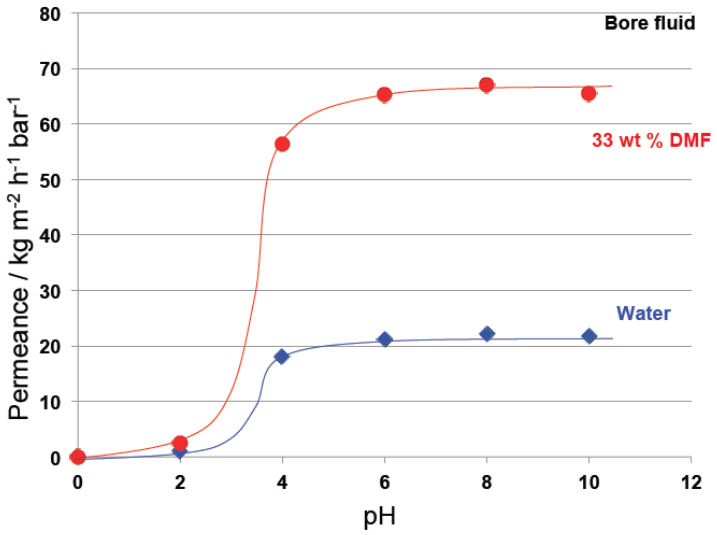

Figure 4a.5 Water permeance of hollow fibers prepared from 22 wt % PS-*b*-P4VP in a DMF/acetone/dioxane solvent system using water or water/33 wt % DMF as the bore fluid.

4a.3.5 Hollow fibers with catalytically active gold nanoparticles

Our two methods, either depositing preformed colloidal gold or reducing the gold ions after adsorption, resulted in the deposition of nano-sized gold particles on the outer surface of the fibers. The particles were preferentially placed in the pyridine coronas and could be detected by electron microscopy (Figures 4a.6 and 4a.7).

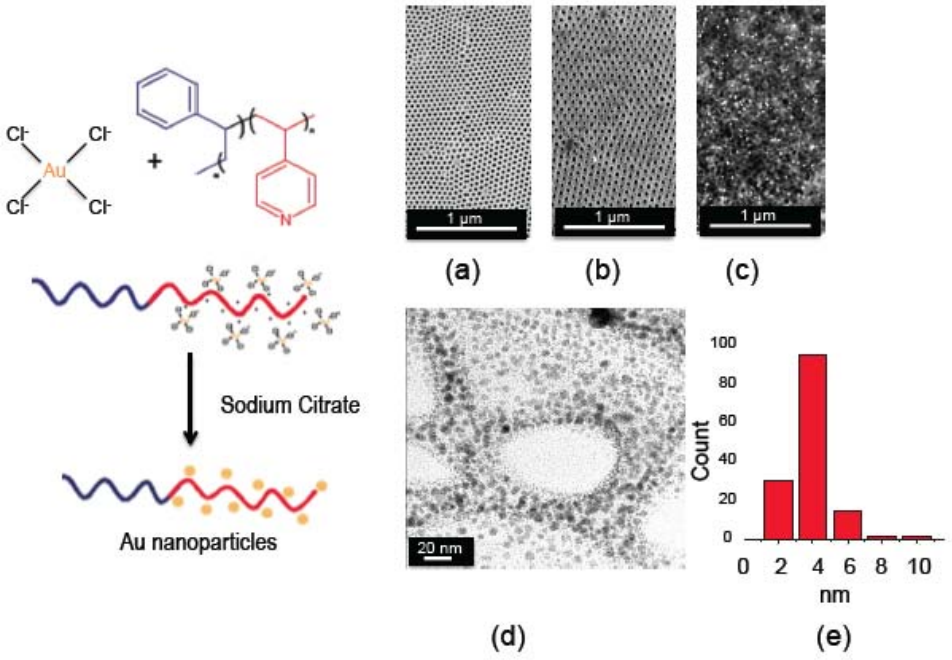

Figure 4a.6 Preparation of catalytic membranes by treatment with gold salts followed by reduction with sodium citrate. (a) FESEM image of an untreated flat-sheet membrane; (b and c) a membrane after gold incorporation; (b) secondary electrons and (c) backscattering electrons; (d) TEM image of a membrane cross-section with gold nanoparticles; (e) the size distribution of the gold nanoparticles is around 4 nm.

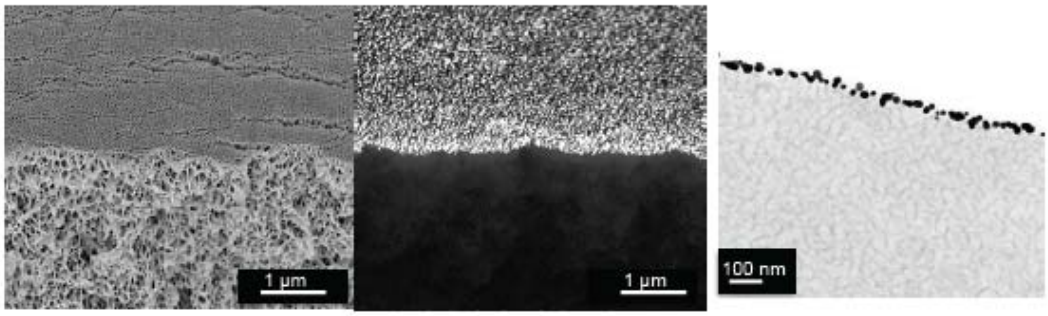

(a) **(b)** **(c)**

Figure 4a.7 Hollow fibers with gold nanoparticles. FESEM images of the (a) secondary and (b) backscattering electrons; (c) TEM image of a cross-section of a fiber.

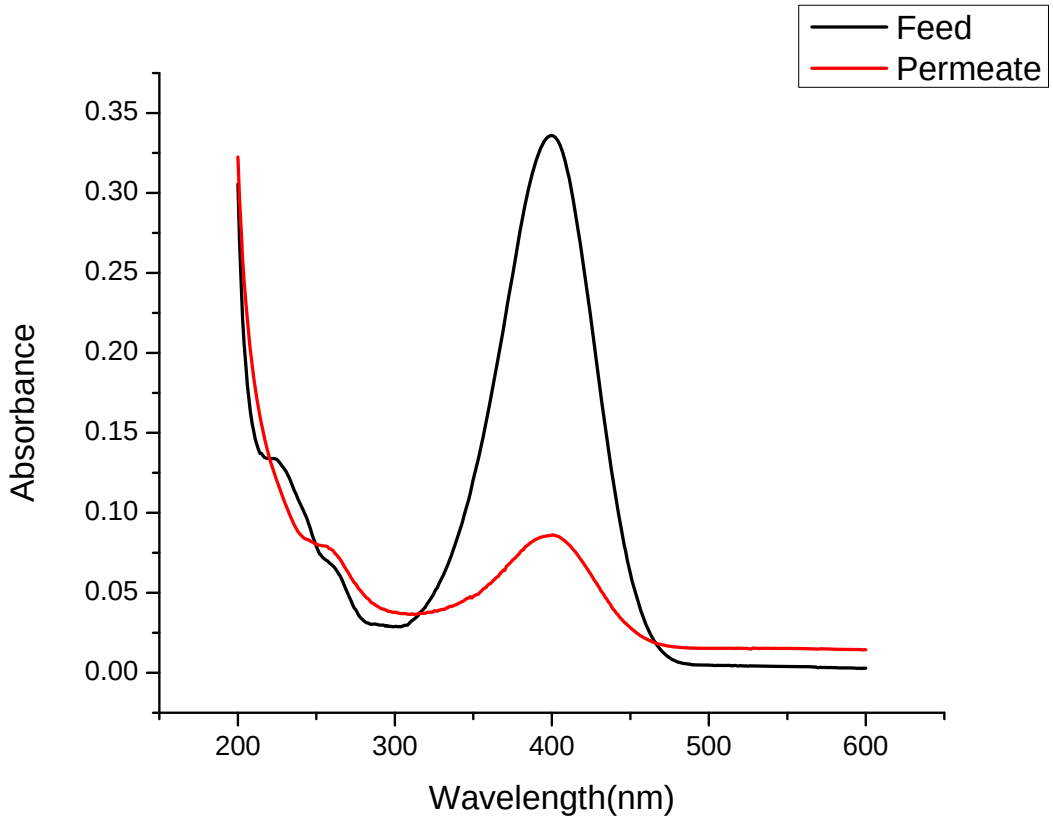

Figure 4a.8 Reduction of p-nitrophenol to p-aminophenol catalyzed by gold nanoparticles and followed by UV absorbance measurements

The catalytic activity was tested using a small one-fiber module (fiber length 9.9 cm, fiber diameter 694 µm, effective area 2.16 cm^2). One hundred ml of a solution containing 1.39 mg nitrophenol and 37.83 mg sodium borohydride as a reducing agent was pumped under a pressure of 1.5 bar through the hollow fiber module. About 0.5 ml of the solution were collected as the permeate after 21 hours. Figure 4a.8 shows the nitrophenol peak at 400 nm of both the feed and the permeate. The nitrophenol concentration in the permeate was reduced from 0.1 mM to 0.023 mM due to reduction to aminophenol.

4a.4 REFERENCES

1. Nunes, S.P.; Behzad, A.R.; Hooghan, B.; Sougrat, R.; Karunakaran, M.; Pradeep, N.; Vainio, U.; Peinemann, K.-V. *ACS Nano* 2011, 5, 3516-3522.

2. Nunes, S.P.; Karunakaran, M.; Pradeep, N.; He, H.; Behzad, A.R.; Hooghan, B.; Sougrat, R.; Peinemann, K.-V. *Langmuir* 2011, 27, 10184-10190.

3. Nunes, S.P.; Sougrat, R.; Hooghan, B.; Anjum, D.H.; Behzad, A.R.; Zhao, L.; Pradeep, N.; Pinnau, I.; Vainio, U.; Peinemann, K.-V. *Macromolecules* 2010, 43, 8079-8085.

4. Bates, F.S.; Hillmyer, M.A.; Lodge, T.P.; Bates, C.M.; Delaney, K.T.; Fredrickson, G.H. *Science* 2012, 434, 440.

5. Park, C.; Yoon, J.; Thomas, E.L. *Polymer* 2003, 44, 6725-6760.

6. Park, S.; Lee, D.H.; Xu, J.; Kim, B.; Hong, S.W.; Jeong, U.; Xu, T.; Russell, T.P. *Science* 2009, 323, 1030.

7. Ruzette, A.V.; Leibler, L. *Nat. Mat.* 2005, 4, 19-31.

8. Mai, Y.; Eisenberg, A. *Chemical Society Reviews* 2012, 41, 5969-5985

9. Kneifel, K.; Nowak, S.; Albrecht, W.; Hilke, R.; Just, R.; Peinemann, K.-V. *J. Membr. Sci.* 2006, 276, 241-251.

10. Kneifel, K.; Peinemann, K.-V. *J. Membr. Sci.* 1992, 65, 295-307.

11. Qiu, X.; Yu, H.; Karunakaran, M.; Pradeep, N.; Nunes, S.P.; Peinemann, K.-V. *ACS Nano* 2013, 7, 768-776.

12 Mai, Y.; Eisenberg, A. *Acc. Chem. Res.* 2012, 45, 1657-1666.

13. Nandan, B.; Stamm, M.; Horechyy, A.; Chen, H.L.; Srivastava, R., Pal, J.; Sanwaria, S. *J. Mater. Chem.* 2012. 22, 25102– 25107.

14. Kao, J.; Thorkelsson, K.; Bai, P.; Rancatore, B.J.; Xu, T. *Chem. Soc. Rev.* 2013. 42, 2654– 2678.

15. Daniel, M.C.; Astruc, D. *Chem. Rev.* 2004, 104, 293-346.

16. Chen, X.; Zhao, D.; An, Y.; Zhang, Z.; Cheng, J.; Wang, B.; Shi, L. *J. Colloid Interface Sci.* 2008, 322, 414-420.

17. Kuroda, K.; Ishida, T.; Haruta, M. *Journal of Molecular Catalysis A: Chemical* 2009, 298, 7-11.

18. Peinemann, K.-V.; Abetz, V.; Simon, P.F.W. *Nature Materials* 2007, 6, 992-996.

19. Peinemann, K.-V. Self-assembled block copolymer membranes with high water flux and selectivity. *In IUPAC MACRO World Polymer Congress*, Blacksburg, VA, June 24–29, 2012.

20. Radjabian, M.; Koll, J.; Buhr, K.; Handge, U.A.; Abetz, V. *Polymer* 2013, 54, 1803–1812.

21. Dorin, R.M., Marques, D.S., Sai, H., Vainio, U., Phillip, W.A., Peinemann, K.-V., Nunes, S.P., Wiesner, U. *ACS Macro Letters,* 2012, 1, 614-617.

CHAPTER 4b

3D Membrane Imaging and Porosity Visualization

Summary

Ultrafiltration asymmetric porous membranes were imaged by two microscopy methods, which allow 3D reconstruction: Focused Ion Beam and Serial Block Face Scanning Electron Microscopy. A new algorithm was proposed to evaluate porosity and average pore size in different layers orthogonal and parallel to the membrane surface. The 3D-reconstruction enabled additionally the visualization of pore interconnectivity in different parts of the membrane. The method was demonstrated for a block copolymer porous membrane and can be extended to other membranes with application in ultrafiltration, supports for forward osmosis, etc, offering a complete view of the transport paths in the membrane.

This chapter was published as*: Ganesh Sundaramoorthi, Markus Hadwiger, Mohamed Ben-Romdhane, Ali R. Behzad, Poornima Madhavan, and Suzana P. Nunes, 3D Membrane Imaging and Porosity Visualization, Ind. Eng. Chem. Res., 2016, 55 (12), pp 3689–3695

My contribution in this chapter was the membrane preparation, gold incorporation and membrane staining only.

4b.1 Introduction

Synthetic membranes are integrated in a variety of processes, which go from hemodialysis to water desalination, beverages and dairy product manufacture, gas separation in petrochemical and pharmaceutical industry. They have different requirements of stability, flux and selectivity. Integral asymmetric or multilayer asymmetric porous membranes are used in almost all membrane-based process [1]. While the top layer determines the membrane selectivity and the separation capability, the porous sub-layer provides the needed mechanical stability and should not negatively interfere with the transport. The control of the sub-layer porosity is relevant for many other reasons. We mention here some of the motivations for porosity control in membranes:

(a) assure high selectivity and high flux in micro-, ultra- and nanofiltration

(b) guarantee high resistance to compaction in high pressure gas processes

(c) minimize concentration polarization in forward osmosis (FO)

(d) optimize chemical conversion in membrane reactors using catalytic membranes

(e) deliver high flux in membrane distillation (MD)

(f) optimize catalyst access in fuel cell (FC) membrane-electrode-catalyst assemblies

(g) optimize cell growth in tissue scaffolds

(h) increase the efficiency of separators in lithium batteries

We detail here some of the examples. While reverse osmosis (RO) uses high hydrodynamic pressure as driving force for water transport, in FO the driving force is concentration difference leading to osmotic pressure. A draw solution drives the water through the membrane with lower energy needs than for RO. Membranes are asymmetric with a very thin selective layer and a porous substrate. The main drawback of the method is

concentration polarization (CP), i.e. the polarization process within the porous sub-layer, which substantially affects the mass transfer through the membrane. Different modeling approaches have been proposed to understand polarization to better design FO membranes. This is usually done, by assuming membrane structure parameters, which are related to specific levels of tortuosity, porosity and layer thickness [2-5].

Membrane distillation is an emerging desalination method, which uses a hydrophobic porous membrane to separate a hot feed with high salinity from the cold permeate side [6]. The main driving force for MD is a temperature difference. How fast the water transfer through the membrane and condensation will take place depends not only on the temperature gradient but also on the membrane porosity and tortuosity.

In polymer electrolyte fuel cell a dense ionic membrane is coated with dispersed catalyst particles and assembled to a porous electrode and gas diffusion layer. The porosity of all layers contributes to the efficiency of the reactive conversion. Optimizing the morphology of the membrane-electrode-assembly is an important part of the fuel cell development [7, 8]. The combination of phase inversion and block copolymer self-assembly leads to the formation of an isoporous aligned structure on the top of the membrane and a sub-layer with gradient porosity [9-11]. Morphology control in solution and in the final asymmetric membrane is decisive for the final membrane application in ultrafiltration.

Well-known methods for pore size characterization are extensively used for membranes [12]. Examples are scanning electron microscopy (SEM), atomic force microscopy (AFM), bubble pressure and gas transport, mercury porosimetry, permporometry, BET adsorption and thermoporometry. BET gives us quantified information of total surface area

or the overall porosity, accessible to the probing gas. SEM and AFM are restricted in most cases to image the membrane surface morphology. 2D imaging of membrane cross-sections is possible by SEM. Porosimetry gives information on average pore size and distribution. However in none of these methods it is possible to have a detailed characterization of porosity in all different layers of the membrane.

As far as morphological characterization is concerned, we have been using advanced microscopy and scattering methods for membrane characterization [9-11], including field emission electron microscopy (FESEM) and transmission electron microscopy (TEM) tomography, associated to synchrotron scattering methods. Cryo-TEM and cryo-SEM helped in investigating copolymer assembly in solution [11-14], before the membrane manufacture. We used for the first time cryo-SEM and environmental scanning electron microscopy to image the effect of pH on stimuli-responsive porous membranes [10]. Mottern et al. [15] used focus ion beam (FIB) to prepare ceramic membrane samples as single slices for TEM imaging. Kyotani et al. [16] reported a similar method combined to grazing incidence X-ray diffraction analysis of tubular zeolites.

More recently new methods of tomography or 3D microscopy image reconstruction have become available with potential use in membrane technology, offering then the perspective of having a complete overview of porosity in the whole volume. Holzer et al. [17] applied focused ion beam (FIB/SEM) for 3D reconstruction of porous ceramics. FIB has been much more applied to inorganic porous materials. However its application to polymeric membranes has been much less explored, since additional care and control of experimental parameters are required to avoid sample damage for instance when exposed to Gallium ions. We were the first to report the used of FIB coupled to FESEM for a qualitative 3D-

reconstruction of polymeric porous membranes [9]. The 3D visualization and semi-automated segmentation were carried out using software tools implemented in the program Amira (TGS, San Diego, CA). Zils et al. [18] applied FIB nanotomography in a similar way for characterization of polymer electrolyte fuel cell. They used FIB serial sectioning and SEM imaging sequence. Alignment of the image stacks was done with the software ImageJ and StackReg Plugin and analyzed with Otsu algorithm. 3D reconstruction of polymeric membranes is also possible by X-ray computed tomography [19] or synchrotron radiation computed microtomography [20, 21], however the image resolution is around a few micrometers or for the microtomography around 100 nm, what makes the methodology suitable only for microfiltration.

If quantitative information is required on membranes with pores in the nanometer range, 3D reconstruction associated to FESEM would be more a suitable method, as far as image resolution is concerned. Even better resolution (<1 nm) is provided by TEM tomography. We have used TEM tomography before to image block copolymer membranes [22], offering precise and detailed information on the membrane selective layer. TEM tomography was recently used by Pacheco et al. [23] to visualize the structure of the top selective layer of thin film composite membranes. High resolution is important in these cases. The disadvantage of TEM tomography is the small sampling volume (*ca.* 2-5 micrometer in the three dimensions), which does not give an overview of the whole membrane structure.

More than an optical visualization method, a quantitative analysis is required to fully correlate morphology to transport, selectivity and additional parameters such as concentration polarization. While 2D microscopy images do not allow measurements of

volume specific surface area with pore length distribution and connectivity across the membrane, a 3D quantitative analysis is ideal for this purpose. We recently demonstrate how 3D image simulation can help in predicting transport characteristics in membranes [24]. Quantitative analysis can be incorporated as starting point for flux simulations to design better membranes. By providing experimental 3D quantitative visualization of membrane morphology, transport simulations would be even more effective. Valuable achievements on quantified morphological characterization of membranes have been recently reported. ElHadidy et al. [25, 26] and AlMarzooqi et al. [26] worked on pore analysis for ultrafiltration membranes based on AFM images correlating with porometry techniques. AFM images have 3D visualization, Their disadvantage is that they just sample the superficial layers of a membrane. Kazemi et al. [27] proposed an image analysis technique to quantify the structural characteristics of electrospun membranes based on SEM, enabling computation of layered and overall porosity. It would be very useful to have a quantitative analysis of pore size distribution layer by layer for a porous membrane, obtaining a complete 3D mapping of the structure. This can be hardly done experimentally. Confocal microscopy gives information on porosity in different layer depths for a porous structure. Snyder et al. [28] reported a quantitative analysis of zeolite membranes imaged by laser scanning confocal microscopy. However again the resolution is not as high as for FESEM or TEM and it is not enough for membranes with pore size in the range of nano- or ultrafiltration. There is a need for more complete approaches, offering quantitative characterization associated to 3D reconstruction with high resolution. Reingruber et al. [29] recently published the quantitative analysis of a 3D-reconstruction of microfiltration membranes using serial sectioning provided by an ultramicrotome in the specimen chamber

of an environmental scanning electron microscope (ESEM). The method is called serial block face scanning electron microscopy (SBF/SEM). The ESEM resolution is normally lower than that of FESEM, but the method was appropriate for microfiltration membranes.

Figure 4b.1 summarizes the resolution of different 3D imaging methods and the sampling volume.

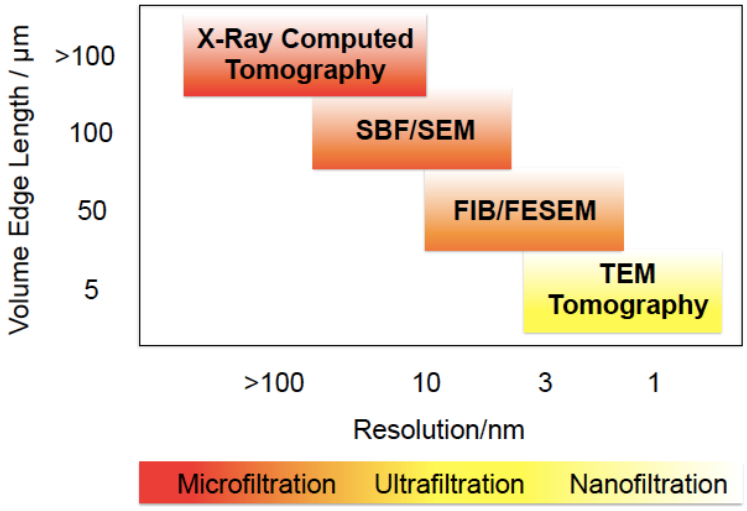

Figure 4b.1 3D Imaging of membranes

In this work we explore two electron microscopy methods for 3D imaging, FIB/FESEM and SBF/SEM, for the characterization of block copolymer membranes with pore size of 20-50 nm, a range, which requires higher resolution than for microfiltration and can not be achieved by X-ray computed tomography. We propose a new segmentation method for quantitative analysis of porosity of membranes slice sets applied to the two methods. Information on porosity can be obtained in different layers or depths. We demonstrate the feasibility, by applying the methods to membranes prepared by block copolymer self-assembly and non-solvent induced phase separation. The membranes are asymmetric with

a top layer containing pores in the range of 20-50 nm. As the depth increases, the pore size increases and the pores become less regular. The same method can be extended in principle to any other polymeric porous membrane.

4b.2 Experimental section

4b.2.1 Materials

Polystyrene-*b*-poly(4-vinylpyridine) block copolymer (PS-b-P4VP 175000-*b*-65000)) (P9828-S4VP was purchased from Polymer Source, Inc., Canada. 1,4-Dioxane, dimethylformamide (DMF), gold (III) chloride and sodium citrate were supplied by Sigma-Aldrich. Tetrahydrofuran was supplied by Fischer Scientific. Methyl iodide used for staining was supplied by Acros-organics.

4b.2.2 Membrane preparation

The membranes analyzed in this work were prepared by block copolymer self-assembly and non-solvent induced phase separation, a method, which has been explored by our group in the last few years. The membranes characterized by FIB/FESEM and by SBF/SEM were prepared by slightly different procedures:

Procedure 1: The membrane imaged by FIB/FESEM was prepared by casting a PS-b-P4VP solution in a mixture of dimethyl formamide and tetrahydrofuran with copper acetate, as previously reported in Ref. [9].

Procedure 2: The membrane analyzed by SBF/SEM was prepared by casting a PS-b-P4VP solution in a 1:1:1 (wt%) mixture of DMF, THF and dioxane, followed by immersion in

water, analogous to the description reported in Ref. [14]. The prepared PS-b-P4VP membrane was then used to filter a 1 wt% gold (III) chloride solution. Gold ions complex with pyridine blocks [30]. The complexed gold was then reduced to gold nanoparticles by treating the membrane with a 0.05 M sodium citrate solution.

Imaging

Two methods were used for imaging: (1) Focused Ion Beam (FIB)/Field Emission Scanning Electron Microscopy and (2) Serial Block Face Scanning Electron Microscopy (SBF/SEM).

4b.2.3 Focused Ion Beam (FIB) and Field Emission Scanning Electron Microscopy (FESEM)

Membranes prepared by procedure 1 were sectioned, by using focused ion beam. To minimize the polymer sample damage by the ion beam, the beam currents were lower than usually applied for semiconductors analysis, and a protective Pt layer was deposited, prior to milling the surface at the region of interest. The layer was deposited using ion beam induced CVD, inside the FIB/FESEM chamber. In order to effectively dissipate surface charge from the surface, the membrane surface was also sputter- coated with Au prior to imaging/milling.

The series of 150 slices (each with 50 nm thickness) was obtained by using a FEI Helios 400S small dual beam system and Slice & View software.

4b.2.4 Serial Block Face Scanning Electron Microscopy (SBF/SEM)

The morphology of membranes prepared by procedure 2 was analyzed by serial block-face scanning electron microcopy (SBF/SEM), performed with a GATAN 3View sectioning system. SBF/SEM combines environmental scanning electron microscopy and an automated ultramicrotome placed inside the microscope chamber. Backscattered electrons detector is normally used for imaging. To increase the conductivity and coefficient of backscattered electron signals, the membrane was stained with vapors of methyl iodide for 4 h before embedding it in resin blocks. The resin block with embedded membrane was cut off with jewelry saw and glued with epoxy resin to aluminum rivet in such a way that a profile of the membrane cross section would be observed once the block face is trimmed with razor blade and ultra-microtome. To minimize charging, the lateral sides of the block face were coated with colloidal silver paint and the block face was coated with 5 nm gold inside a sputter coater. A Quanta 200 FEG SEM (FEI) equipped with the GATAN 3View door and backscattered electron detector was used for serial sectioning and imaging of the block face. The image stack of 50 nm slices was acquired in an automated fashion in low vacuum mode under the following conditions: 2.0 kV voltage, current of 43 pico Amp, resolution 1024x1024, pixel size 8 nm, pixel time 32 µ seconds, chamber pressure of 0.2239 Torr, magnification of 16,477 x. A set of 1000 slices was obtained.

4b.2.5 Segmentation method

3D reconstruction with detailed and quantitative information on pore size and porosity in different layers of the membrane requires first the segmentation of the microscopy slices images. Details of the segmentation method using the *Mumford-Shah Model* [31-34] and

an algorithm developed at KAUST for this purpose are described below.

Mumford-Shah Segmentation

The multi-label Mumford-Shah functional is in the form:

$$E(\{R_i, f_i\}_{i=1}^{N}) = \sum_{i=1}^{N} \int_{R_i} (I(x) - f_i(x))^2 \, \mathrm{d}x + \alpha \mathrm{Reg}(f_i) + \beta \mathrm{Len}(\partial R_i), \quad (1)$$

which is subjected to the constraint that R_i are mutually exclusive and the union is the entire domain Ω of the image. Here $I : \Omega \to \square^k$ is the image (with k-channels), $f_i : R_i \to \square^k$ are approximations of the image in the regions R_i, ∂R_i denotes the boundary of R_i. Discrepancy of the data $I(x)$ to $f_i(x)$ is measured through D (e.g., $D(I(x)), f_i(x)) = |I(x) - f_i(x)|^2$ for the original Mumford-Shah problem), $Reg(\cdot)$ will impose spatial regularity of f_i in the region R_i, one possible choice is

$$\mathrm{Re}\, g(f_i) = \int_{Ri} \left| \nabla f_i(x) \right|^2 dx \quad (2)$$

and the length penalty Len (·) is to ensure special regularity of the region R_i (since

Len (∂R_i) = $\int_{\Omega} \left| \nabla 1_{Ri}(x) \right| dx$, where 1_{R_i} indicates the characteristic function of R_i).

New Generative Model

The reason why these problems are difficult to optimize is the interdependence of each of the variables on the other in the optimization. Indeed, to define a function f_i, the region R_i must be known, but the region R_i is unknown. Similarly, if the functions f_i are known (i.e.,

the image reconstruction), then the discontinuities form the boundaries of the regions, and the regions can be defined, however the functions are unknown. Hence, there is a constraint that must be maintained between the function and the regions.

We wish to undue the dependence of the functions on the regions by considering a different underlying model for image formation. We illustrate the idea on the joint image denoising and segmentation problem, but it can be generalized in other Mumford-Shah (MS) problems. The underlying model in the original MS denoising/segmentation problem is

$$I(x) = f_i(x) + \eta(x), x \in R_i, f_i : R_i \to \mathbb{R}^k \tag{3}$$

$$p(f_i | R_i) \propto \exp(-\alpha \int_{R_i} |\nabla f_i(x)|^2 dx) \tag{4}$$

where η is a noise process, and the probability is the conditional prior probability of the function f_i. The generative model implies that the regions R_i must be first chosen according to a prior distribution, and the functions may then be chosen according to a conditional distribution (conditioned on the region). In the proposed formulation, we wish to remove this conditional dependence, while still maintaining the ability to generate all the images that the original model can generate. Our model is the following:

$$I(x) = f_i(x) + \eta(x), x \in R_i, f_i : \Omega \to \mathbb{R}^k \tag{5}$$

$$p(f_i) \propto \exp(-\alpha \int_{\Omega} |\nabla f_i(x)|^2 dx) \tag{6}$$

where we have defined the functions on the entire domain Ω (and defined the regularity on Ω) rather than R_i, and therefore, the prior probability of the functions is no longer

conditional on the regions. Hence to generate the image, the sampling of the regions and functions are done independently. The benefit of this deceivingly simple modification of the original model is that in optimization, the regions can be updated more globally than in the original model. The cost is a higher dimensional problem. However, the proposed formulation leads to a better local optimum, and is even faster to converge than the traditional model as we show in experiments.

Optimization Algorithm

The proposed model leads to the following regularity term in the energy:

$$\mathrm{Re}\, g(f_i) = \int_\Omega \left|\nabla f_i(x)\right|^2 dx \tag{7}$$

rather than (2), and the other terms in the energy (1) remain the same:

$$E(\{R_i, f_i\}_{i=1}^N) = \sum_{i=1}^N \int_{R_i} D(I(x), f_i(x))\,\mathrm{d}x + \alpha \int_\Omega |\nabla f_i(x)|^2\,\mathrm{d}x + \beta \mathrm{Len}(\partial R_i) \tag{8}$$

Since the conditional dependence of the function on the region is now removed, the update of the regions can be computed given the functions in a more global fashion, and the optimal update of the functions can be computed given the regions.

Given estimates of the functions $f_i : \Omega \to \square^k$, we describe how to obtain optimal estimates for the regions R_i. Notice that, unlike the standard model, when optimizing in R_i for a fixed f_i, the second term in (8) can be ignored, as it does not depend on the region. For the moment, setting $\beta = 0$, the globally optimal estimate is (given the functions f_i are fixed) is

$$R_i = \left\{ x : i = \arg_j \min D(I(x), f_j(x)) \right\} \tag{9}$$

The above optimum does not take into account the length term that implies spatial regularity of the regions, and thus we show how to integrate that next. We first approximate the length term with the following region integral:

$$\int_{R_i} W_{R_i}(x)\,dx \tag{10}$$

where $W_{R_i}(x) = \frac{1}{\sigma}\left(G_\sigma * 1_{R_i^c} \right)(x)$

and $G\sigma$ indicates a Gaussian smoothing kernel of standard deviation σ, and $1_{R_i^c}$ is the indicator function on R_i^c. It can be shown from the co-area formula and the Lebesgue differentiation theorem that the integral above converges to the length as $\sigma \to 0$. Therefore, when $\beta > 0$ we seek to optimize

$$\sum_{i=1}^{N} \int_{R_i} \left(D(I(x), f_i(x)) \right) + \beta W_{R_i}(x)\,dx \tag{11}$$

Note that we like to apply the same argument as before, and write the optimal solution as a simple thresholding step as in (9); however, part of the integrand depends on the region Ri (when $\beta \neq 0$), which is unknown. Fortunately, if one has an approximation of Ri , R_i' , then substituting WRi , with W_{R_i}' , and optimizing (11) with respect to Ri yields

$$R_i = \left\{ x : i = \arg_j \min D(I(x), f_j(x)) + \beta W_{R_j'}(x) \right\} \tag{12}$$

Notice this requires two parameters, β and σ; if desired to avoid an additional parameter, one can get similar results by simply replacing $D\ (I(x),\ fj(x)) + \beta\ W_{R_j'}\ (x)$ with $G\sigma * D(I(\cdot),fj(\cdot))$, i.e., enforce spatial regularity by smoothing the data term.

As an initial approximation, we choose R_i' to be (9). The equation (12) can then be iterated with the previous estimate replacing R_i'. In practice, the iteration is done only once, which yields an accurate segmentation, as we show. As $\sigma \to 0$ and D = 0, the iterative scheme was considered in [33] and approximates mean curvature flow, and thus minimizes the length of the boundary of the regions. In our numerical scheme, we consider a fixed σ and only one iteration, the effects of a large number of iterations are attained by a larger σ.

Also, given that regions *Ri* are fixed, we can compute a global minimum for the *fi* (in the case of a convex D). For the case that $D(x, y) = |x - y|^2$, we have that

$$-\alpha \Delta f_i(x) = \left(I(x) - f_i(x) \right) 1_{R_i}(x). \tag{13}$$

We now have the following simple iterative algorithm to obtain an approximate solution to the Mumford-Shah problem:

1. Initialize $\left\{ R_i \right\}_{i=1}^{N}$
2. Solve for the *fi*:

$$-\alpha \Delta f_i(x) = (I(x) - f_i(x))_{R_i}(x) \qquad x \in \text{int}(\Omega)$$

$$\frac{\partial f_i}{\partial N} = 0 \qquad x \in \partial\Omega$$

where N denotes the normal to the boundary (Neumann boundary conditions), and int(·) denotes interior. The equations can be solved efficiently with a conjugate gradient solver.

3. Compute $R_i^{'}$:

$$\left\{ x \in \Omega : i = \arg_j \min \left| I(x) - f_j(x) \right|^2 \right\},$$

4. Update R_i:

$$R_i = \left\{ x \in \Omega : i = \arg_j \min F_j(x) \right\},$$

where $F_j(x) = \left| I(x) - f_j(x) \right|^2 + \beta W_{R_j^{'}}(x).$

5. Repeat 2-4 until R_i converges

For segmentation, the image of the membrane consists of empty spaces (pores) and membrane matrix, which have to be automatically identified and separated from each other. The image intensity in different regions is spatially homogeneous. The membrane can be considered as consisting of several regions whose image intensity is described by smooth function plus additive noise. The goal of the segmentation algorithm is to determine the regions, in which the image intensities are smooth functions. Since both the functions and regions are initially unknown, the algorithm below estimates both simultaneously.

The problem described is a classical problem in computer vision, which is normally referred as Mumford-Shah Model [31-34]. Several numerical optimization methods have been proposed to solve this problem [35, 36], but the algorithms tend to be computationally

expensive, prone to local optima, and extremely sensitive to initialization. Therefore, we employ a recent technique [32], which is computationally efficient (compared to [35, 36]), less susceptible to local minima, insensitive to initialization, and therefore, may be employed in a fully automated scheme.

4b.3 Results and discussion

FIB has been recognized as a successful method for morphology investigation of different kinds of materials, but has been particularly well applied for nanofabrication in the semi conductor industry [37] or preparation of ceramic samples for transmission microscopy [38], which could not be easily cut by ultramicrotomy. More recently FIB/FESEM has been increasingly used for the characterization of biological samples [39]. The use of FIB for polymeric membranes has been much more restrict and a reason for that is the potential damage of the sample by exposure to the beam, if the conditions are not properly controlled. Boussu et al. [40] were one of the first to report the use of FIB for polymeric membrane characterization. However they used it only to expose cross-sections of different polymeric membranes for SEM investigation in an alternative way to the classical sample fracture. Our group was probably the pioneer in using FIB sectioning for 3D reconstruction of polymeric porous membranes, as reported 6 years ago [9]. Low beam currents and a protective Pt layer were applied to minimize damages. Our previous report used FIB for qualitative visualization purpose. Here we propose a method to quantify porosity in different membrane layers, demonstrating it for asymmetric porous membranes. Typical membrane slices 2D images obtained by FIB/FESEM are shown in Figure 4b.2.

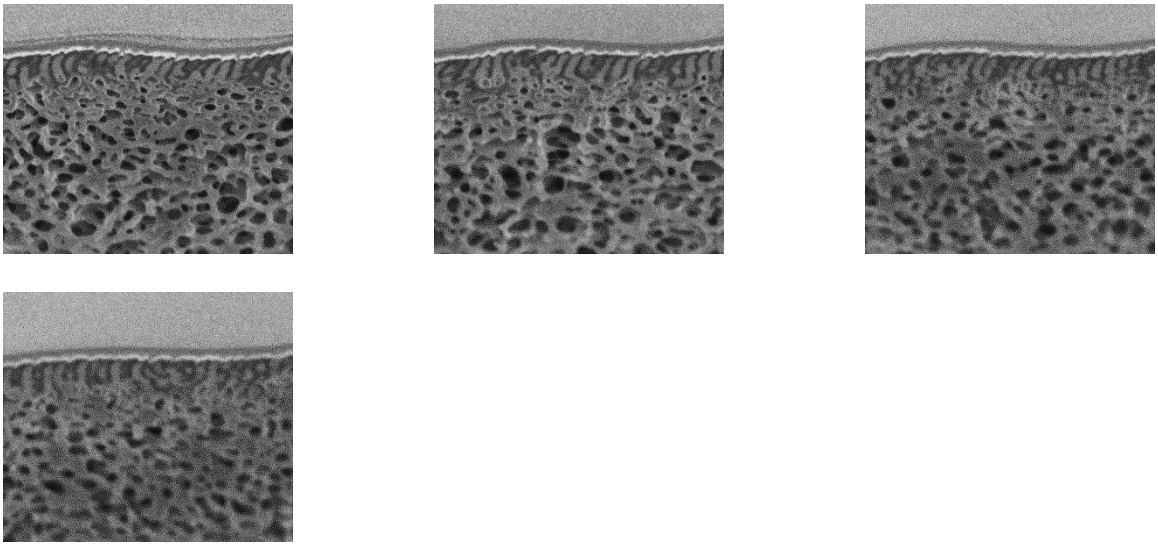

500 nm

Figure 4b.2 FIB/FESEM Membrane slices images to be segmented.

Figure 4b.3 shows the 3D reconstruction of the membrane from slices obtained by FIB/FESEM, similar to those depicted in Figure 4b.2. Figure 4b.3b represents the first step of segmentation.

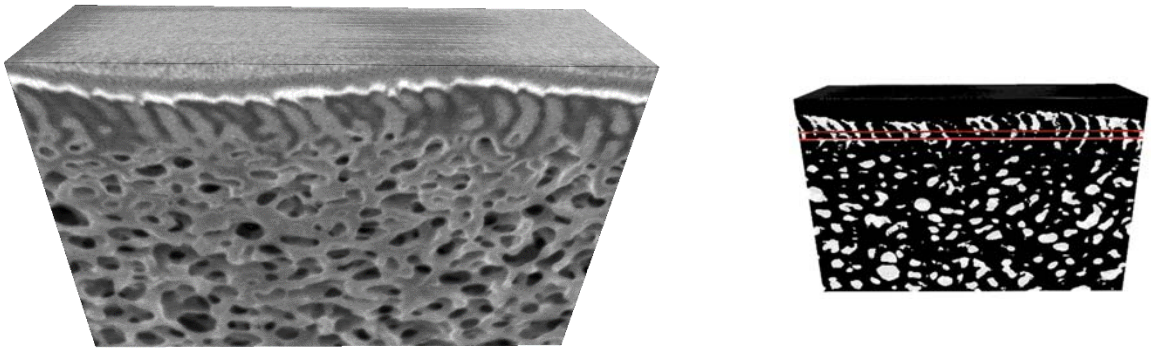

(a) (b)

Figure 4b.3. (a) 3D visualization of the membrane reconstructed from the set of slices obtained by FIB/FESEM and respective (b) segmentation.

FIB/FESEM allows the imaging of slices obtained orthogonal to the membrane surface. For practical reasons, slices parallel to the membrane surface can be hardly experimentally obtained. By 3D reconstruction and application of the developed algorithm, the porosity and pore average size in different layers parallel to the membrane surface can be now quantified, giving a complete picture of the membrane.

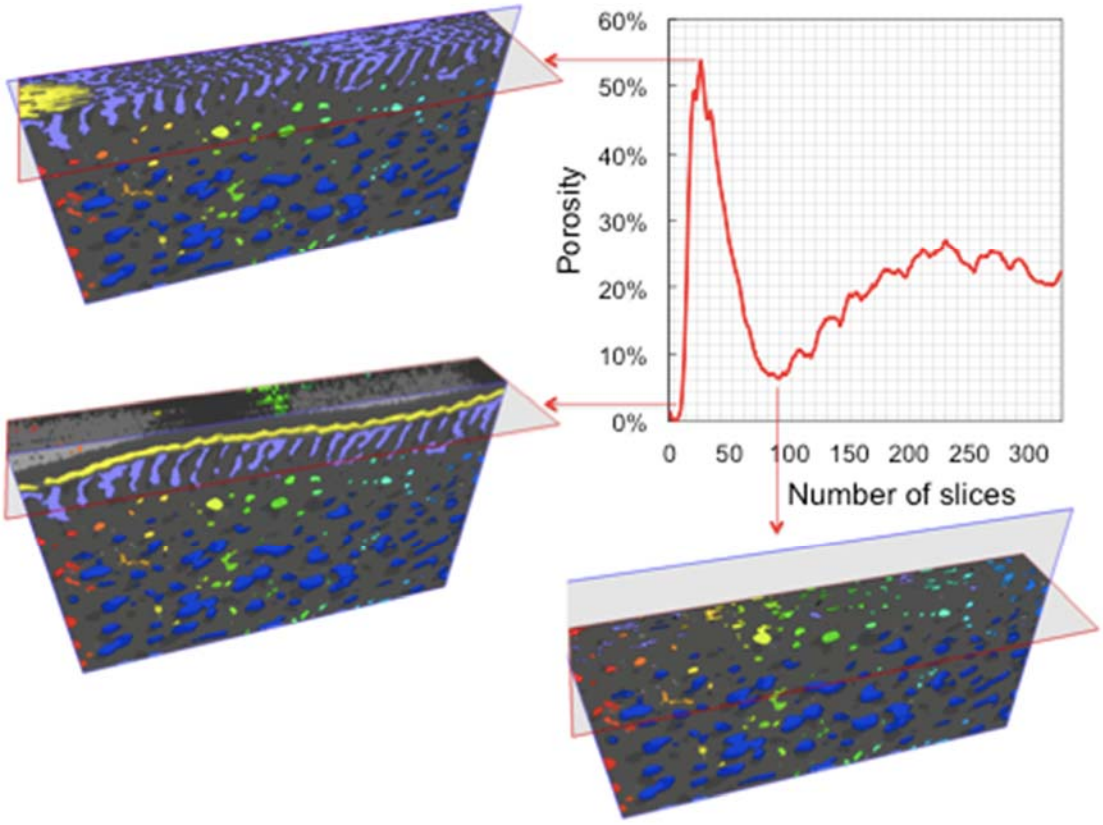

Figure 4b. 4 Porosity layer by layer, calculated for each virtual slice parallel to the membrane surface, each slice with thickness of 50 nm. Images obtained by FIB/FESEM.

Figure 4b. 4 shows the results of the porosity calculation using the algorithm, as well as the visualization of different cuts corresponding to layers of different porosity.

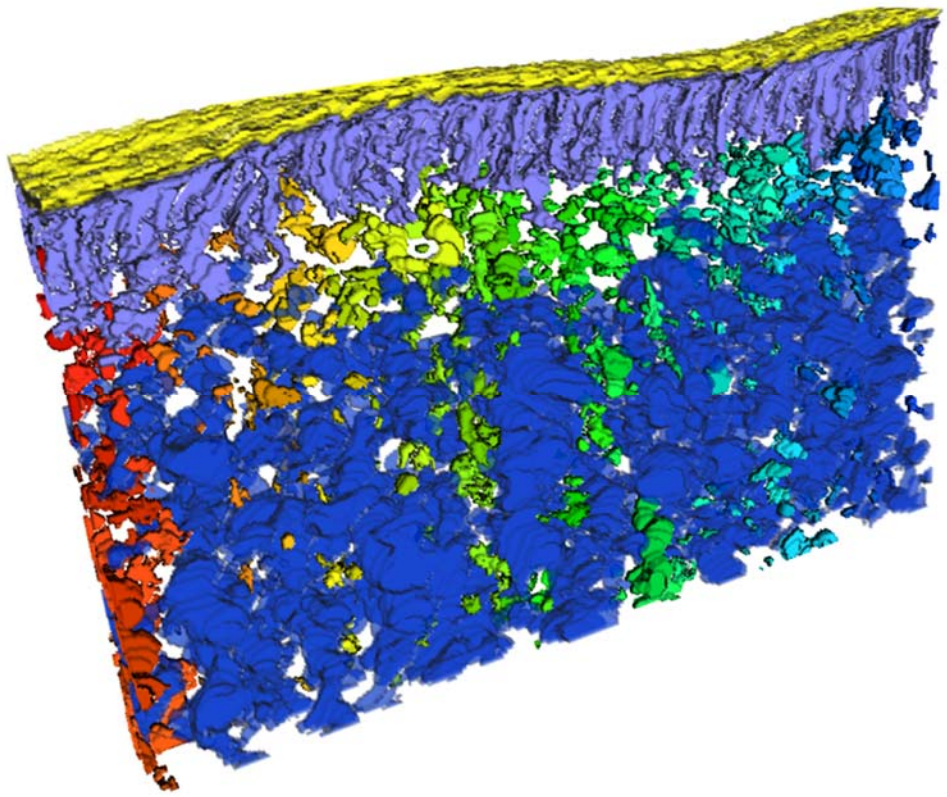

Figure 4b.5 3D-Reconstruction of the membrane, after segmentation and algorithm application. Each color represents pore regions with interconnectivity.

As a result of the segmentation it is possible also to distinguish the pore regions, which are highly interconnected. This is visualized in Figure 4b.5, with different colors representing regions with preferential inter-pore connectivity.

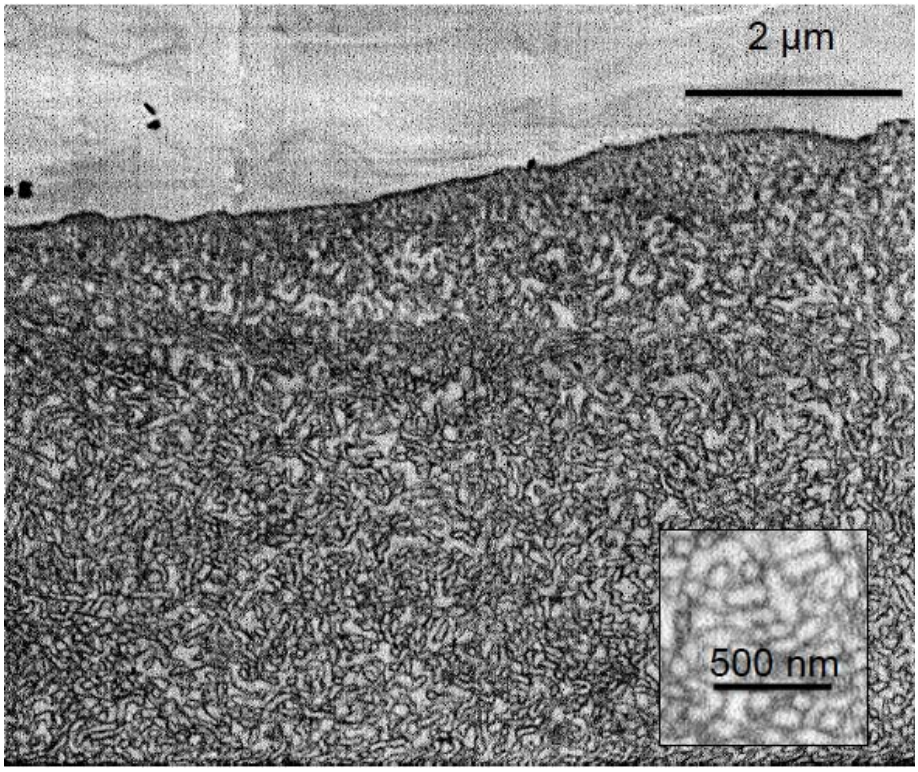

Figure 4b. 6 Membrane slice, obtained by SBF/SEM, after staining with CH_3I and gold.

Analogously to the imaging process by FIB/FESEM, membranes were characterized by SBF/SEM using the GATAN 3View system. A typical slice image can be seen in Figure 4b.6. Strong contrast was provided by staining the samples with CH_3I and gold. Since the image is formed using backscattered electrons detector, SBF/SEM is particularly suitable when the membrane is stained or when the morphology is decorated with nanoparticles. As for the FIB/FESEM slices, segmentation and 3D reconstruction were conducted for SBF/SEM images and the porosity was quantitatively analyzed and presented in Figure 4b.7. As in Figure 4b.5, different colors emphasize pore regions with high interconnectivity.

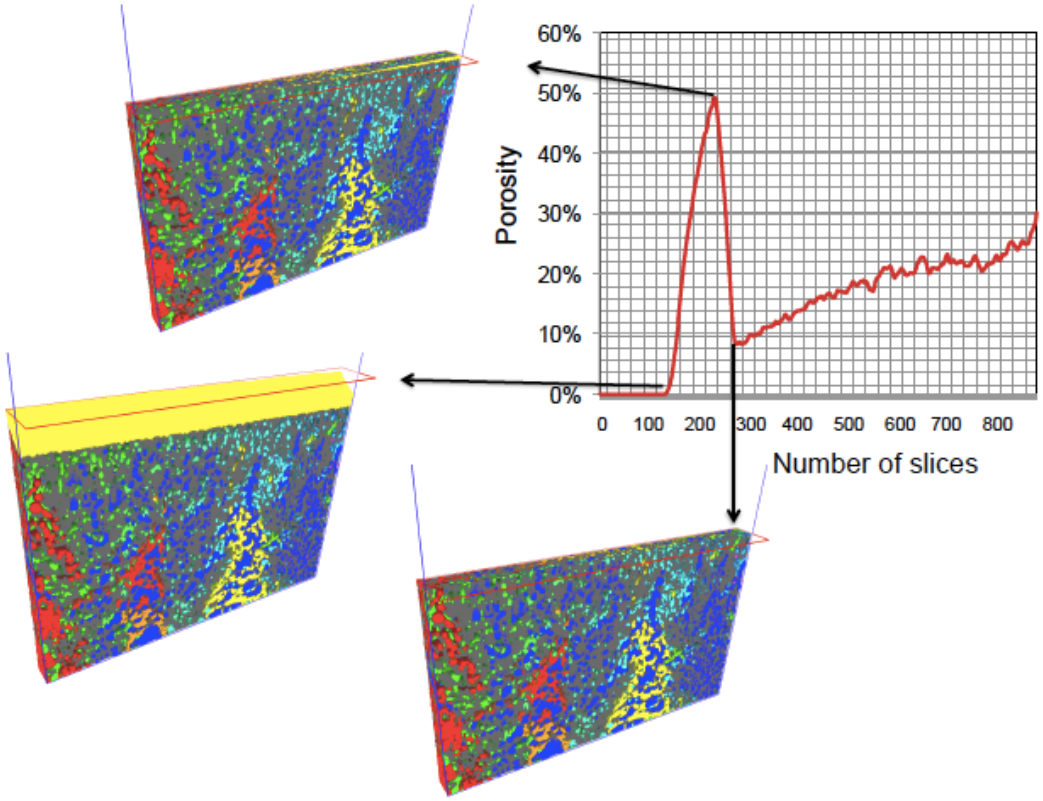

Figure 4b.7 Porosity layer by layer, calculated for each virtual slice parallel to the membrane surface, each slice with thickness of 50 nm. Images obtained by GATAN 3View.

Both imaging methodologies used in this work gave similar quantitative information on porosity. The convenience of using one or other depends on the characteristic of membrane being characterized, contrast for backscattering electrons and stability in the ion beam. Figure 4b.6 for SBF/SEM is closer to images obtained by TEM and takes advantage of analogous staining or intrinsic contrast provided by elements of higher electron density or different capacity of scattering electrons. A diamond knife is used as for TEM. The samples must be sliceable by the knife and properly prepared, including adequate

embedding in resin. SBF/SEM can in principle sample larger volumes in shorter times than FIB/FESEM, as claimed also for other materials [39, 41]. According to previous literature [39] for instance for biological samples, whose characteristics are not much different than that of polymeric membranes, FIB/FESEM is slightly superior in resolution and lower in terms of coverable volumes. FIB/FESEM would be the method of choice in the case of ceramic membranes of other hard materials, which should not be cut by diamond knifes. Both SBF/SEM and FIB/FESEM cover much larger volumes than TEM tomography. We have used TEM tomography before [22] for membrane characterization, which provides excellent resolution, but the imaged area is restricted. The possibility of imaging a large part of the membrane, typically with thickness of 20-50 micrometer or higher, can be very useful to have a complete understanding of transport. Both SBF/SEM and FIB/FESEM cover this range. The membranes investigated here have pores larger than 20 nm and for that the resolution of both methods is sufficient. This would be the case for most ultrafiltration membranes. When imaging smaller pores, the resolution of FIB/FESEM could be advantageous.

The results obtained by applying segmentation, 3D reconstruction and the developed algorithm allowed the quantification of porosity in any layer parallel to the surface going from one side to the other of the membrane. Also information on the pore interconnectivity in adjacent areas is provided. This is very useful in the field of synthetic membranes. Most commercial membranes for ultra- nanofiltration and reverse osmosis as well as gas separation are asymmetric membranes with complex morphology. Morphological characterization is essential as tool for membrane development and to take decisions on best choices for each application and process optimization. For fully understanding or

simulating transport in membranes the 3D reconstruction and analysis described in this paper can be much more useful than regular 2D images obtained by SEM or TEM, giving the complete view and quantitative information. We recently used 3D simulation for theoretical membrane reconstruction and demonstrated how it could help to predict membrane transport characteristics [24]. Here we provide experimental 3D images and we anticipate that this information could be used in combination with transport simulation tools similar to those used in Ref. [24] and additional methods under development for a much better transport and structure optimization in the near future.

4b.4 REFERENCES

1. Nunes, S.P., Peinemann, K.-V. Membrane technology: in the chemical industry, John Wiley & Sons, 2006.

2. Loeb, S. Titelman, L, Korngold, E., Freiman, J. *J. Membr. Sci.*, 1997, 129, 243-249.

3. Gruber, M., Johnson, C., Tang, C., Jensen, M. H., Yde, L. *J. Membr. Sci.*, 2011, 379, 488-495.

4. Li, W., Gao, Y., Tang, C.Y. *J. Membr. Sci.*, 2011, 379, 307-321.

5. Park, M., Lee, J. J., Lee, S., Kim, J. H. *J. Membr. Sci.*, 2011, 375 241-248.

6. Maab, H., Al Saadi, A., Francis, L., Livazovic, S., Ghafour, N., Amy, G. L., Nunes, S. P. *Ind. Eng. Chem. Res*., 2013, 52, 10425-10429.

7. Prehn, K., Adelung, R., Heinen, M., Nunes, S.P., Schulte, K., *J. Membr. Sci.*, 2008, 321, 123-130.

8. Tripathi, B. P., Schieda, M., Shahi, V. K., Nunes, S. P. *J. Power Sources*, 2011, 196, 911-919.

9. Nunes, S. P.; Sougrat, R.; Hooghan, B.; Anjum, D. H.; Behzad, A.R.; Zhao, L.; Pradeep, N.; Pinnau, I.; Vainio, U.; Peinemann, K. V. *Macromolecules* 2010, 43, 8079-8085.

10. Nunes, S. P.; Behzad, A. R.; Hooghan, B.; Sougrat, R.; Karunakaran, M.; Pradeep, N.; Vainio, U.; Peinemann, K. V. *ACS Nano* 2011, 5, 3516-3522..

11. Nunes, S. P.; Karunakaran, M.; Neelakanda, P.; Behzad, A. R.;Hooghan, B.; Sougrat, R; He, H.; Peinemann, K.-V. *Langmuir* 2011, 27, 10184-10190.

12. Nakao, S. *J. Membr. Sci.*, 1994, 96, 131-165.

13. Marques, D. S., Dorin, R. M., Wiesner, U., Smilgies, D. M., Behzad, A. R., Vainio, U., Peinemann, K. V., Nunes, S. P. *Polymer,* 2014, 55, 1327-1332.

14. Marques, D.S., Vainio, U., Chaparro, N. M., Calo, V. M., Bezahd, A.R., Pitera, J. W., Peinemann, K.V., Nunes, S. P., *Soft Matter*, 2013, 9, 5557-5564.

15.Mottern, M. L., Shqau, K., Shi, J., Yu, D., Verweij, H. *Int. J. Hydrogen Energy*, 2007, 32, 3713-3723.

16. Kyotani, T., Mizuno, T., Katakura, Y., Kakui, S., Shimotsuma, N., Saito, N., Nakane, T. *J. Membr. Sci.*, 2007, 296, 162-170.

17. Holzer, L., Indutnyi, F., Gasser, P., Münch, B., Wegmann, M. *J. Microscopy,* 2004, 216, 84-95.

18. Zils, S., Timpel, M., Arlt, T., Wolz, A., Manke, I., Roth, C. *Fuel Cells,* 2010, 10, 966.

19. Dai, S., Seol, Y., Wickramanayake, S., Hopkinson, D. *J. Membr. Sci.*, 2015, 492, 497-504.

20. Remigy, J. C., Meireles, M., Thibault, X. *J. Membr. Sci.*, 2007, 305, 27-35.

21.Tung, K.-L., Chang, K.-S., Wu, T.-T., Lin, N.-J., Lee, K.-R., Lai, J.-Y. Curr. Opin. Chem. Eng., 2014, 4, 121-127.

22. Madhavan, P., Sougrat, R., Behzad, A. R., Peinemann, K. V., Nunes, S. P. *J. Membr. Sci.*, 2015, 496, 568-577.

23. Pacheco, F., Sougrat, R., Reinhard, M., Leckie, J. O., Pinnau, I. *J. Membr. Sci.*,, 2016, 501, 33-44.

24. Shi, M., Printsypar, G., Iliev, O., Calo, V. M., Amy, G. L., Nunes, S. P. *J. Membr. Sci.*, 2015, 487, 19-31.

25. ElHadidy, A.M., Peldszus, S., Van Dyke, M. I. *J. Membr. Sci.*, 2013, 429, 373-383.

26. AlMarzooqi, F. A., Bilad, M., Mansoor, B., Arafat, H. A. *J. Mater. Sci.,* 2016, 51, 2017-2032.

27. Kazemi Pilehrood, M., Dilamian, M., Mirian, M., Sadeghi-Aliabadi, H., Maleknia, L., Nousiainen, P., Harlin, A. BioMed Res. Int., 2014, 2014, 1-9.

28. Snyder, M., Vlachos, D., Nikolakis, V. *J. Membr. Sci.*, 2007, 290, 1-18.

29. Reingruber, H., Zankel, A., Mayrhofer, C., Poelt, P. *J. Membr. Sci.*, 2011, 372, 66-74.

30. Hilke, R.; Pradeep, N.; Madhavan, P.; Vainio, U.; Behzad, A. R.; Sougrat, R.; Nunes, S. P.; Peinemann, K.-V. *ACS Appl. Mater. Interfaces* 2013, *5*, 7001-7006.

31. Blake, A., Zisserman, A. *Visual reconstruction*, MIT press Cambridge, 1987.

32. Hong, B- W., Lu, Z., Sundaramoorthi, G. 2013 *IEEE Conference on, IEEE*, 2013, pp. 1219-1226.

33. Merriman, B., Bence, J. K., Osher, S. Diffusion generated motion by mean curvature, Department of Mathematics, University of California, Los Angeles, 1992.

34. Mumford, D., Shah, J. *Communications on pure and applied mathematics*, 1989, 42, 577-685.

35. Tsai, A., Yezzi Jr, A., Willsky, A. S. *IEEE Transactions*, 2001, 10, 1169-1186.

36. Vese, L.A., Chan, T. F. *Int. J. Computer vision*, 2002, 50, 271-293.

37. Cooper, D., Rivallin, P., Guegan, G., Plantier, C., Robin, E., Guyot, F. *Semiconductor Science and Technology*, 2013, 28, 125013-125020.

38. Volkert, C. A., Minor, A. M. *MRS bulletin*, 2007, 32, 389-399.

39. Kizilyaprak, C., Daraspe, J., Humbel, B. *J. Microscopy*, 2014, 254, 109-114.

40. Boussu, K., De Baerdemaeker, J., Dauwe, C., Weber, M., Lynn, K.G., Depla, D., Aldea, S., Vankelecom, I.F., Vandecasteele, C., Van der Bruggen, B. *Chem. Phys. Chem*, 2007, 8, 370-379.

41 Müllner, T., Zankel, A., Svec, F., Tallarek, U. *Materials Today,* 2014, 17, 404-411.

CHAPTER 5

Silver-Enhanced Block Copolymer Membranes with Biocidal Activity

Summary

Silver nanoparticles were grown in the surface and pore walls of block copolymer membranes with highly ordered pore structure. Pyridine blocks constitute the pore surfaces, complexing silver ions and promoting a homogeneous distribution. Nanoparticles were then formed by reduction with sodium borohydride. The morphology varied with the preparation conditions (pH and silver ion concentration), as confirmed by field emission scanning and transmission electron microscopy. Silver has a strong biocide activity, which for membranes can bring the advantage of minimizing the growth of bacteria and formation of biofilm. The membranes with nanoparticles prepared under different pH values and ion concentrations were incubated with Pseudomonas aeruginosa and compared with the control. The strongest biocidal activity was achieved with membranes containing membranes prepared under pH 9. Under these conditions, the best distribution with small particle size was observed by microscopy.

This chapter was published as*: P. Madhavan, Pei-Ying Hong, Rachid Sougrat and Suzana.P.Nunes, Silver Enhanced Bock copolymer Membranes with Biocidal activity, ACS Applied Materials and Interfaces, 2014, 6(21), pp 18497-18501.

5. 1 Introduction

The combination of block copolymers self-assembly and phase inversion[1-7] has been demonstrated as a successful method to manufacture asymmetric membranes with high porosity, high water flux and very sharp pore size distribution. Water fluxes far above 1000 L m^{-2} h^{-1} bar^{-1} could be achieved with selectivity enough to separate proteins with very close molecular weight like bovine albumin (66 kDa) and hemoglobulin.(65 kDa).[7] This combination of flux/selectivity has not been possible before with polymeric phase inversion membranes and makes the new class of membranes unique with perspective of application in many fields varying from biomedical devices to separation of valuable products in aqueous media. Having a biocide activity can be advantageous in different applications for which bacteria growth has to be avoided. In water-based separations processes, biofouling is a common issue, which strongly affects the performance in operation. Even membranes with exceptional initial permeation characteristics can experience dramatic flux decrease after short time of operation due to surface adhesion of microorganisms, forming biofilms, which partially block the pores. The main goal of this work is to propose a strategy to minimize biofouling to be specifically applied to the new class of block copolymer membranes.

Biofouling can have serious consequences not only in membrane operation, but in fields varying from medicine, food industry to marine transportation.[8-19] The formation of biofilms occurs in different steps. The adhesion of bacteria on surfaces is a decisive primary phase, followed by microbial growth.[8,11] Microorganisms embedded in biofilm produce extracellular polymeric substances, which form the biofilm structure and assure its cohesion. Biofilm formation is a serious issue in water treatment, being evident in pipe

distribution networks. Membrane systems for water treatment have a growing market, but also in this field biofouling or biofilm formation on the membrane surface, with consequent reduction of operation performance, is a major problem with challenging control. Aggressive cleaning procedures are normally applied to recovery the membrane performance. Reducing biofilm formation has better chances of success if the first steps of microorganism adhesion can be avoided. Biocides can be an effective agent for that.

Silver is known for biocide in different fields. It has been widely used as biocide in traditional medicine, for treatment of wounds before the advent of modern antibiotics, in water sterilization aboard space stations and as disinfection additive for food.[8-15] The silver biocide activity is in part believed to depend on silver ions, which are released from silver particles and strongly bind to electron donor groups in biomolecules, causing defects in the cell walls, forming complexes with proteins and DNA, finally causing death of bacteria or hindering the reproduction.[12-15] The ion positive charge is reported to contribute to the attraction between ions and negative charged cells. But silver nanoparticles even partially negatively charged can accumulate and cause irregular pits in bacterial membranes. Formation of free radicals and radical-induced membrane damage has been also associated to the biocide mechanism.[14] How effective the silver ion release takes place depends on the particles morphology. Larger surface area facilitates the release. Well-dispersed nanoparticles are expected to be more effective than larger particles.[16-19]

Silver has been reported as biocide agent for membranes based on polylactic, acid,[16] polyamide,[17] polysulfone,[18] poly (vinylidene fluoride).[19] Immobilization is required to avoid excessive leaching out of silver during operation. Cao et al.[18] immobilized silver ions on polysufone (PES) membranes, by a multi-step process, first sulfonating PES and

blending it to the non-modified polymer to cast membranes. Silver ions were added to interact with the sulfonic group on the membrane surface and reduced to elementary silver particles. Shiffmann et al.[20] prepared first silver nanoparticles capped with poly (ethylene imine). Polysulfone electrospun nanofibers were treated with oxygen plasma to introduce functional groups, like –COOH to the surface and the PEI-capped particles were then attached to the functional groups. Polysulfone-Ag nanoparticles mats displayed a high bioactivity against *E. coli*, *S. aureus*, and *B. anthracis*.[20] Here our membrane is isoporous and pH responsive[2], manufactured from block copolymers of polystyrene and polyvinylpyridine. We describe the incorporation of silver nanoparticles and how it affects the membrane biocide capability. We take advantage of the complex formation between silver ions and pyridine[21] to assure homogeneous and stable metal distribution.

5.2 Experimental section

5.2.1 Materials

Polystyrene-*b*-poly (4-vinylpyridine) block copolymer P10900-S4VP (PS-*b*-P4VP 188,000-*b*-64,000 g/mol) was purchased from Polymer Source, Inc., Canada. Dimethyl formamide (DMF), 1,4 dioxane and acetone was supplied by Fisher Scientific. Silver nitrate ($AgN0_3$) (99%), sodium borohydride ($NaBH_4$), sodium hydroxide pellets (NaOH) and hydrochloric acid (HCl) 37% was purchased from Sigma Aldrich.

5.2.2 Membrane Preparation

Membranes were prepared with the block copolymer polystyrene-*b*-poly (4-vinyl pyridine) (PS-*b*-P4VP) (molecular weight 188,000-b-64,000 g/mol). A solution with 18 wt% block copolymer, 24 wt % DMF, 42 wt % dioxane (42%) and 16 % acetone was stirred at room

temperature for 24 hours and cast using a doctoral blade with a gap of 200 μm on a glass plate or on a polyester nonwoven. The solvent was evaporated during 10 s and the film was precipitated in de-ionised water. Finally the membranes were dried at room temperature. Pores are formed by a combination of micelle assembly and phase separation caused by the solvent-water exchange, as discussed before[3,4] and a regular morphology as shown in Figure 5.1a is obtained. The silver nanoparticles were generated and incorporated by first immersing the prepared membrane into 1.0 mM $AgNO_3$ and adjusting pH to the desired value by adding drops of 0.1N NaOH and/or 0.1 N HCl solutions. The membrane was rinsed with deioninsed water several times and then immersed in 2.0 mM $NaBH_4$. In a series of experiments the pH was set as 2.1, 4 and 9, keeping $AgNO_3$ 1.0 mM. In a second series the pH was kept neutral and the $AgNO_3$ concentration was varied from 1.0 mM to 0.5M.

5.2.3 Morphological Characterization

The morphology of the membranes was characterized by field emission scanning electron microscopy (FESEM) and transmission electron microscopy (TEM). The membranes were imaged with a Nova Nano 630 microscope using a voltage of 5 kV. Prior to imaging, the samples were sputtered with platinum using a K575X Emitech sputter coater. For TEM the membranes were cut in a LEICA EM UC6 cryo-ultramicrotome after being embedded in a low viscosity resin and imaged in a Titan FEI transmission electron microscope operating at 300 kV.

5.2.4 Bacterial counting

Cultures of *Pseudomonas aeruginosa* DSM1117 were diluted with 0.85% w/v NaCl to an $OD600_{nm}$ of 0.07. This corresponds to a cell concentration of approximately 1 x 10^8 cell/mL. The membranes with silver as well as the control membrane were individually immersed into 4 ml of diluted cell suspension, and incubated at 37º C in an orbital incubator shaker for 24, 48 and 72 h. After incubation, the cell suspension was then aliquot and diluted by 1000-fold with 0.85% w/v NaCl, and then stained with LIVE/DEAD® BacLight™ bacterial viability kit (Invitrogen, CA) for 10 min at 35 ºC prior to flow cytometry on Accuri C6 (BD Biosciences). 2 ml of 0.85% w/v NaCl were added to each of the remaining membranes, and ultrasonicated for 3 minutes by Q500 sonicator (Qsonica) at 25% amplitude to dislodge the attached bacteria into the suspension. The suspension is then stained with LIVE/DEAD® BacLight™ bacterial viability kit using protocols as above-mentioned. The leaching out of silver from the membrane was quantified by Inductively Coupled Plasma Mass Spectrometry ICP MS analysis.

5.3 Results and Discussion

5.3.1 Isoporous membrane and silver complexation

The isoporous membranes were manufactured from block copolymers with pyridine segments exposed to form the pore walls and membrane surface. As early reported[21], silver ions complex with pyridine. The incorporation of silver could be easily done by directly complexing silver ions and pyridine. This led to an excellent distribution of nanoparticles on the surface and inside the pores, without need for additional membrane modification. The method was chosen, by taking in account previous work we performed on pyridine-

metal complexation to induce and stabilize self-assembly (Cu and Co ions) and impart catalytic activity (Au ion).[1, 5] In an analogous approach we incorporate Ag ions into the pyridine blocks of highly ordered asymmetric copolymer membranes and tested their antibacterial activity.

5.3.2 Surface characterization

The FESEM images of the pure PS-*b*-P4VP membrane and those with silver nanoparticles at different pH are compared in Figure 5.1. Figure 5.1b shows nanoparticle aggregation on the membrane surface, when the deposition process was conducted at pH 2.1. The membranes with 1.0 mM $AgNO_3$ at pH 7 and 9 have uniform distributions of the nanoparticles unlike the membrane at pH 2.1.

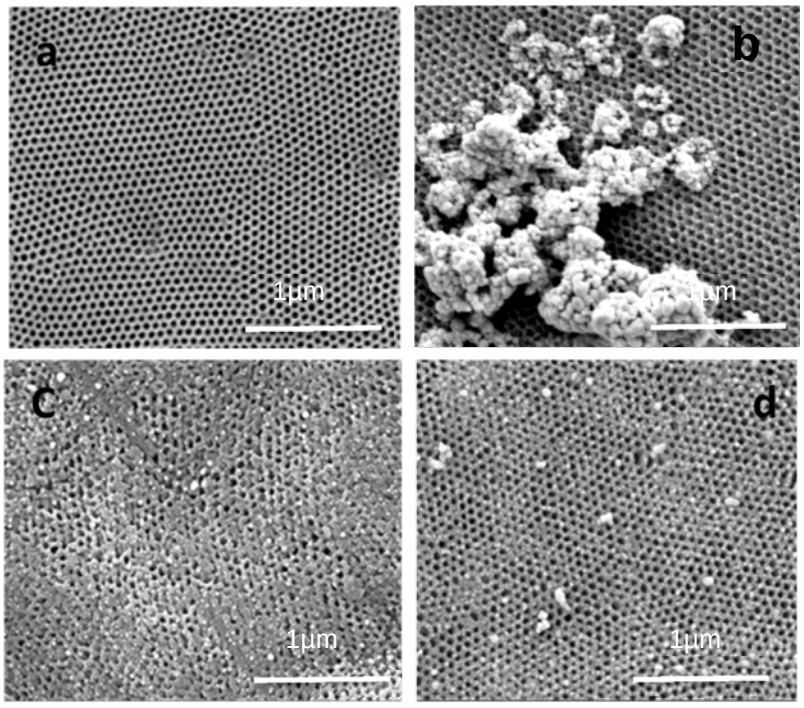

Figure 5.1 FESEM images of a (a) plain PS-*b*-P4VP membrane and membranes with Ag nanoparticles prepared at (b) pH 2.1, (c) pH 7 and (d) pH 9 with 1.0mM $AgNO_3$ solution.

The aggregation observed at pH 2.1 is probably due to the protonation of the pyridine group, which takes place a low pH.[2] When protonated, the membrane acquires a positive charge and the complexation of Ag^+ ions with pyridine is disturbed. Large part of the silver is reduced without being encapsulated by the copolymer segments and are localized as aggregate on the membrane surface. When $NaBH_4$ is added at high pH, merging of silver is hindered since the ions are embedded in the copolymer matrix, surrounded by pyridine.

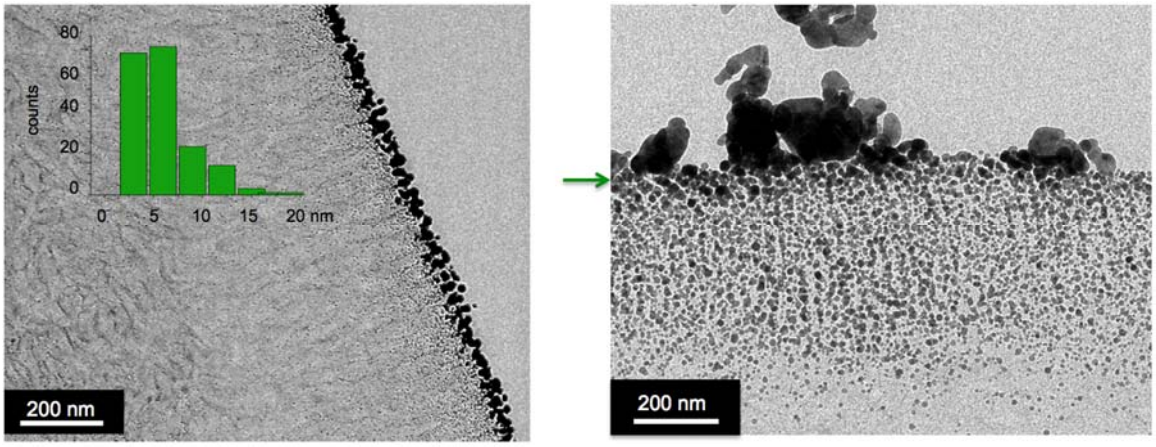

(a) **(b)**

Figure 5.2 TEM micrographs of PS-*b*-P4VP membrane cross sections with Ag nanoparticles (a) formed at pH 9 with 1.0mM $AgNO_3$ solution with the corresponding particle size distribution histogram (inset); (b) formed at pH 2.1. Arrows indicate the membrane surface.

To confirm the fine distribution of Ag in the membranes, transmission electron microscopy (TEM) images were obtained, after sectioning them in ultramicrotome. The TEM images of PS-*b*-P4VP membranes with Ag nanoparticles deposited at pH 9 and 2.1 are shown in Figure 5.2. The pores are orthogonally aligned close to the membrane surface and are disordered as it goes deeper. Larger particles are detected on the membrane surface, particularly in the case of pH 2.1, but a large number of smaller Ag nanoparticles (2-7 nm)

can be seen on the pore walls in the bulk of the membrane. Smaller particles usually exhibit higher antibacterial activities, mainly due to their larger specific area. Nanoparticles in the range of 1-10 nm attach to the surface of the cell membrane and disturb the functionality of the cell like permeability and respiration leading to the death of the cell ultimately.[22]

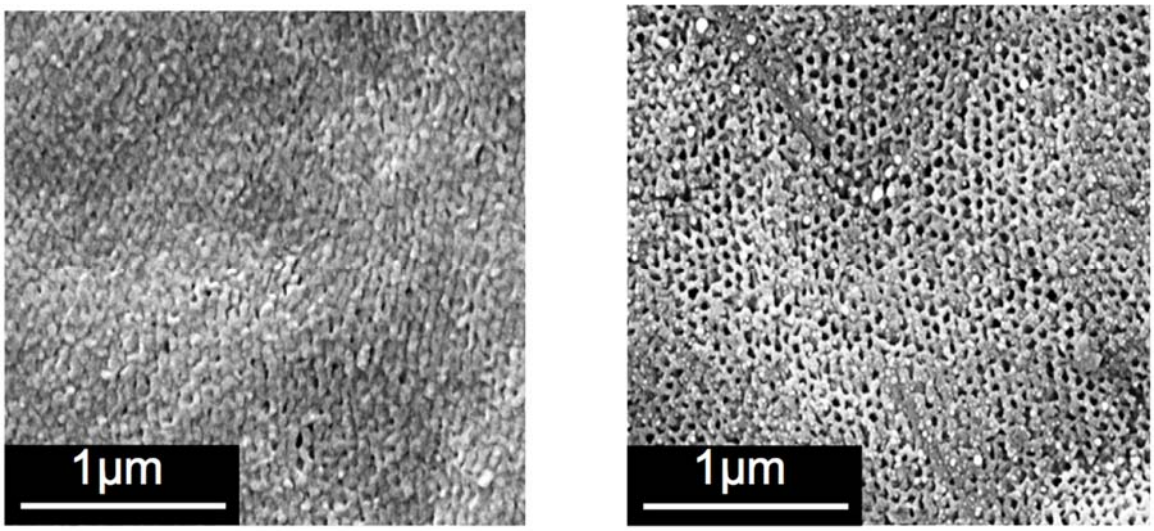

(a) **(b)**

Figure 5.3 FESEM micrograph of a PS-*b*-P4VP membrane with Ag nanoparticles formed at pH 7 with (a) 0.5M and (b) 1.0mM $AgNO_3$.

The PS-*b*-P4VP membranes are known to have a morphology switch around pH 4, closing the pores by protonation of pyridine blocks at lower pH and opening at high pH.[2,7] The water flux, measured above pH 4-5 without silver, was 1200 $Lm^{-2}\ h^{-1}\ bar^{-1}$. After silver incorporation the flux decreased to 147 $Lm^{-2}\ h^{-1}\ bar^{-1}$.The second set of preparation was carried out maintaining the pH neutral, above the switch pH, in which pyridine is not protonated, varying the concentration of $AgNO_3$. The plain membrane was prepared in the

same way as before. The membrane was then immersed in 0.5 M $AgNO_3$, at pH 7, rinsed with deionized water to remove uncomplexed silver particles, immersed in 1.0 M $NaBH_4$ and again rinsed with deionized water. The membrane turned brown immediately. Figure 5.3 shows FESEM micrographs of the membranes. With higher silver concentration the pores appears to be closed. With 1.0mM $AgNO_3$ a uniform porosity is still observed after the nanoparticle formation, which are evenly distributed around the pores.

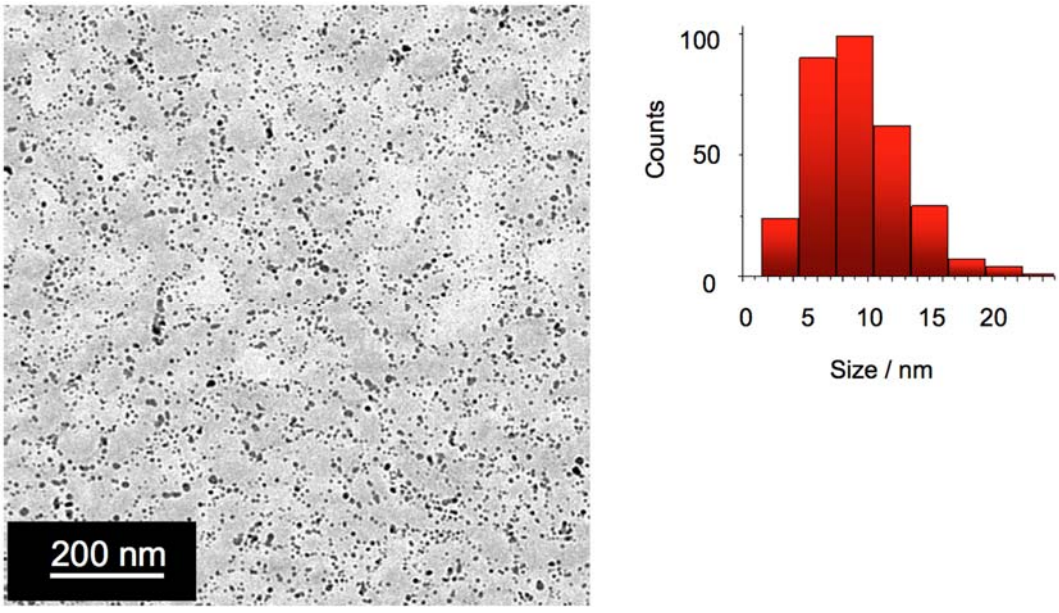

(a) **(b)**

Figure 5.4 (a) TEM image of PS-*b*-P4VP membrane bulk with Ag nanoparticles prepared from 1.0 mM $AgNO_3$ at pH 7 and (b) the corresponding size distribution histogram.

The TEM image of the membrane bulk with nanoparticles obtained from 1.0mM $AgNO_3$ solution at pH 7 is shown in Figure 5.4. The nanoparticles size is 6-10 nm. Also in this case the small particles size with large surface area are expected to promote a high biocide activity.

5.3.3 Bacterial counting

The antibacterial activity of the PS-*b*-P4VP membranes with Ag nanoparticles was evaluated with gram-negative *P. aeruginosa* DSM 1117 bacterium as a model system (Figure 5.5). The inactivation kinetics on both suspended *P. aeruginosa* cells and those attached on the membranes were observed to be different. For the same time of incubation the inactivation was more effective for suspended cells than for the attached ones forming the biofilms. This behavior is more evident in the first 24h of incubation and for samples prepared at pH 2.1 even at longer experiments.

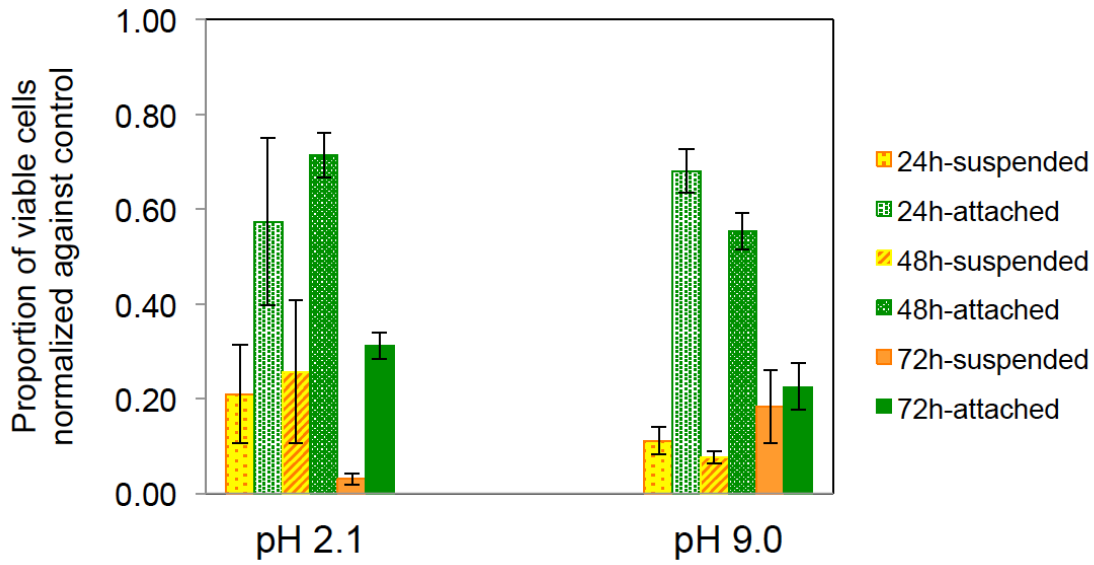

Figure 5.5 Flow cytometry incubation of *P. aeruginosa*: results for PS-*b*-P4VP membranes with Ag nanoparticles prepared at different pH values from 1.0mM $AgNO_3$ solutions.

The proportion of viable cells normalized against the control after 72h of incubation for membranes prepared at pH 2.1 was lower than 5%, demonstrating high efficiency. The proportion of attached viable cells for the same low pH was around 30%. For pH 9 the

proportion of attached viable cells after 72h was ca. 20% (more effective than pH 2.1). The inactivation of suspended cells was only slightly lower than for attached ones at high pH. The formation of extracellular polymeric substances within the biofilm matrix coating the silver nanoparticles and making the direct contact with the cells can be a likely reason to explain for the lower inactivation of attached biomass. Figure 5.1 and 5.2 shows that at high pH the silver nanoparticles are better and fine dispersed in the membrane pores and at low pH silver aggregates are present loosely attached to the membranes. During the incubation the aggregates might still be effective in deactivation the suspended cells, but the finely distributed silver nanoparticles seen at high pH are more adequate for the inactivation of attached cells.

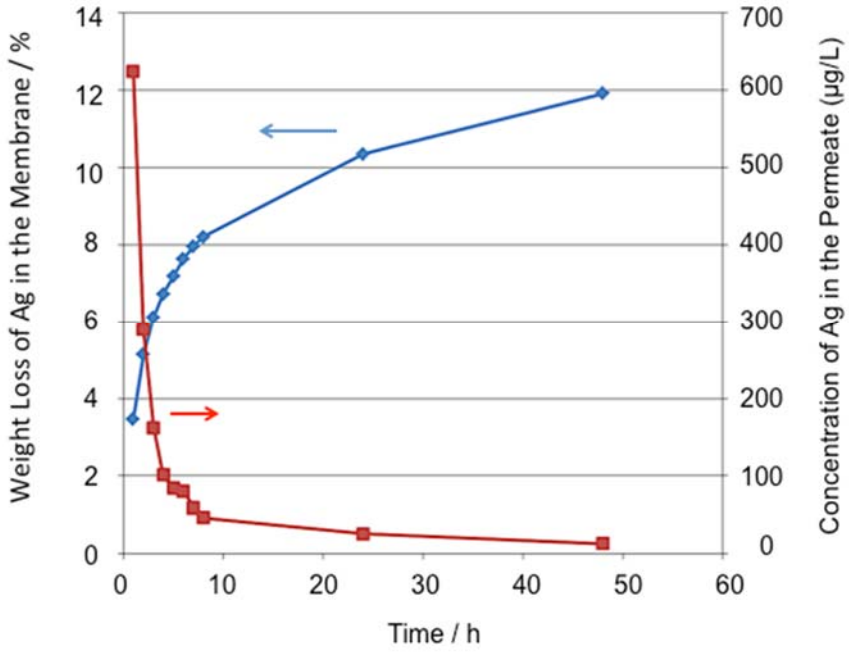

Figure 5.6 Leaching out of silver from the membrane (pH 9, 1.0mM $AgNO_3$) measured by ICP-MS.

From thermal gravimetric analysis an incorporation of 1.74 wt% of Ag related to the total membrane weight could be estimated. Figure 5.6 gives an idea of how much silver is leached out from the membrane after several hours in water. 7 % of the incorporated silver is extracted after the first 5 hours. After this first period only 100 μg/L of silver was detected in the permeate, indicating that the remaining silver is strongly connected to the membrane.

5.4 REFERENCES

1. Nunes, S. P.; Sougrat, R. ; Hooghan, B. ; Anjum, D.H. ; Behzad, A.R. ; Zhao, L. ; Pradeep, N.; Pinnau, I.; Vainio, U. and Peinemann, K-V. *Macromolecules* 2010*,* 43, 8079–8085.
2. Nunes, S. P.; Behzad, A. R. ; Hooghan, B. ; Sougrat, R. ; Karunakaran, M. ; Pradeep, N.; Vainio, U. and Peinemann, K-V. *ACS Nano* 2011, 5, 3516–3522.
3. Nunes, S. P. ; Karunakaran, M. ; Pradeep, N. ; Behzad, A. R.; Hooghan, B. ; Sougrat, R. ; He, H. and Peinemann, K-V. *Langmuir* 2011, 27, 10184–10190.
4. Marques, D.; Vainio, U.; Moreno Chaparro, N.; Calo, V.M.; Behzad, A.R., Pitera, J.; Peinemann, K-V. and Nunes, S. P. *Soft Matter* 2013, 9, 5503-5658. .
5. Hilke, R., Pradeep, N. , Madhavan, P. , Vainio, U. , Behzad, A. R. , Sougrat, R. , Nunes, S. P. and Peinemann, K.-V. *ACS Appl. Mater. Interfaces* 2013, 5, 7001-7006.
6. Madhavan, P., Peinemann, K.-V. and Nunes, S. P. *ACS Appl. Mater. Interfaces* 2013, 5, 7152-7159.
7. Qiu, X. ; Yu, H. ; Karunakaran, M.; Pradeep, N.; Nunes, S. P. and Peinemann, K.-V. *ACS Nano* 2013, 7, 768-776.
8. Faria, A. F.; Martinez, D. S. T.; Meira, S. M. M.; Moraes, A. C. M.; Brandelli, A.; Souza Filho, A. G. and Alves, O. L. *Colloids and Surfaces B: Biointerfaces* 2014, 113, 115–124.
9. Mah, T. F. C. and O'Toole, G. A. *Trends Microbiol*. 2001, 9, 34-39.
10. Callow, J. A. and Callow, M. E. *Nature Communications* 2011, 2, 1-10.

11. Flemming, H. C. and Wingender, J. *Nature Reviews Microbiology* 2010, 8, 623-633.

12. Gupta, A.; Matsui, K.; Lo, J.-F. and Silver, S. *Nature Medicine* 1999, 5, 183-188.

13. Monteiro, D. R.; Gorup, L. F.; Takamiya, A. S.; Ruvollo-Filho, A. C.; Camargo, E. R. and Barbosa, D. B. *Int. J. Antimicrobial Agents* 2009, 34, 103–110.

14. Kim, J. S.; Kuk, E.; Yu, K. N.; Kim, J.-H.; Park, S. J.; Lee, H. J.; Kim, S. H.; Park, Y. K.; Park, Y. H. ; Hwang, C.-Y. ; Kim, Y.-K.; Lee, Y.-S.; Jeong, D. H. ; Cho, M.-H. *Nanomedicine: Nanotechnology, Biology and Medicine* 2007, 3, 95–101.

15. Li, Q.; Mahendra, S. ; Lyon, D. Y.; Brunet, L. ; Liga, M. V. Li and D. Alvarez, P. J. J. *Water Research* 2008, 42, 4591–4602.

16. Dasari, A.; Quirós, J.; Herrero, B.; Boltes, K. ; García-Calvo, E. and Rosal, R. *J. Membrane Sci.* 2012, 405–406, 134–140.

17. Yang, H.-L. ; Chun-Te Lin, J. ; Huang, C. *Water Research* 2009, 43, 3777–3786.

18. Cao, X., Tang, M., Liu, F., Nie, Y.; Zhao, C. *Colloids and Surfaces B: Biointerfaces* 2010, 81, 555–562.

19. Park, S. Y.; Chung, J. W.; Chae, Y. K. and Kwak, S.-Y *ACS Appl. Mater. Interfaces* 2013, 5, 10705-10714.

20. Schiffmann, J. D.; Wang, Y.; Giannelis, E. P. and Elimelech, M. *Langmuir* 2011, 27, 13159-13164.

21. Vosburgh, W. C. and Cogswell, S. A. *J. Am. Chem. Soc.* 1943, 65, 2412-2413.

Wang, H., Liu, J., Wu, X., Tong, Z. and Deng, Z. *Nanotechnology* 2013, 24, 1-9.

CHAPTER 6

Photoresponsive Nanostructured Membranes Manufactured by Non-Solvent Induced Phase Separation Technique

Summary

Nanostructured stimuli-responsive membranes are of great interest to trigger specific separation. Change in pH and temperature have been more frequently investigated. In this work, we demonstrate the preparation of photoresponsive nanostructured triblock copolymer membranes. We used non-solvent induced phase inversion for the membrane manufacture. First, we optimized the membrane formation by using poly(styrene-b-anthracene methyl methacrylate-b-methylmethacrylate) (PS-b-PAnMMA-b-PMMA) copolymer, identifying the most suitable solvent, copolymer block length, and other parameters. The obtained final triblock copolymer membrane morphologies were characterized using atomic force and electron microscopy. The microscopic analysis reveals that the PS-b-PAnMMA-b-PMMA copolymer can form both lamellar and ordered hexagonal nanoporous structures on the membrane top layer in appropriate solvent compositions. The nanostructured membrane emits fluorescence due to the presence of the anthracene mid-block. In addition to fluorescence, on irradiation of light the PS-b-PAnMMA-b-PMMA copolymer membranes show stimuli-responsive behavior. Upon long-wave UV irradiation the anthracene group undergoes conformational changes by forming [4+4] cycloadducts. This alters the membranes water flux and solute retention.

6.1 Introduction

Stimuli-responsive materials change their physicochemical properties in response to environmental conditions such as, pH, temperature, irradiation with light, electric and magnetic fields. [1-5] Porous membranes promote separations mainly by size difference. The development of stimuli-responsive membranes with tunable properties provides opportunities in flux modulations, and separation selectivity control for various advanced applications, e. g. controlled drug release. [6-8] If stimuli responsive functional groups are part of the membrane material, [9-13] conformational changes might occur under the influence of external environmental conditions, leading to changes in the degree of swelling/deswellling of the membrane, in the membrane permeability and selectivity. Temperature and pH response have been more frequently investigated. We propose here a strategy to develop photoresponsive membranes with tunable properties and potential applications as optical gates for controlled delivery or water purification.

Highly ordered membranes were prepared by combining self-assembly of block copolymer and non-solvent induced phase separation (SNIPS).[14] SNIPS is a simple and fast technique for manufacturing nanostructured asymmetric membranes. Membranes with high water flux and good solute rejection have been previously prepared by this method, with excellent pH responsive behavior. [15-19] They mainly contained pyridine or polyacrylic acid blocks. Nanopores of PS-*b*-P4VP membrane were clearly demonstrated to close and open when subject to external pH conditions.[15] The nitrogen atom in the basic pyridine group protonates under acidic condition and swells the pore walls leading to pore closing of the PS-*b*-P4VP membranes and gets deprotonated under basic conditions, deswelling to a reversible opened pore walls. On the other hand PS-*b*-PAA copolymer porous structures

have close pores in basic pH and open at low pH. Our effort is targeted towards exploring response to light instead of pH, extending the possibilities of applications, keeping the high order and porosity. To achieve the light responsive behavior, we chose poly(styrene-*b*-anthracene methyl methacrylate-*b*-methylmethacrylate) (PS-*b*-PAnMMA-*b*-PMMA) triblock copolymer as membrane forming material. The amphiphilic character of the block copolymer led to an ordered self-assembled morphology and the anthracene methyl methacrylate block provided the light responsive behavior.

Anthracene and its derivatives have been widely used as organic optoelectronic materials due to their high fluorescence quantum yields. [20-22] Anthracene moiety can be transformed into photodimers upon long-wave UV irradiation (>350 nm) to give [4+4] cycloadducts and that the photodimer can be restored to original monomers upon exposure to shortwave UV light (254 nm). This photochromism has been studied extensively for many intermolecular and intramolecular processes. [23-25] For example, Zheng and co-workers[26] developed photoreversible PEG-anthracene based hydrogel through the photodimerization of anthracene groups. Rameshbabu et al. prepared photo patternable anthracene, covalently connected through a methylene bridge, which showed significantly higher fluorescence compared to monomeric anthracene.[27] Hargreaves et al., reported the synthesis of poly(9-anthrylmethyl methacrylate) polymers, which have a strong tendency to be photoreactive. The use of anthracene moieties as cross-linking sites to produce photoreversible organogels has been also reported.[28] To alter the membrane properties with response to light, a key strategy is to utilize the photochromism behavior of anthracene group as one of the blocks in the bulk block copolymer membrane. In the present study, we report the formation of lamella and ordered hexagonal nanopores, by using casting solutions in selective solvents,

using PS-b-PAnMMA-b-PMMA triblocks. We demonstrate the membrane light responsive behavior.

6.2 Experimental section

6.2.1 Materials

Poly(styrene-*b*-anthracene methylmethacrylate-*b*-methylmethacrylate) (PS-*b*-PAnMMA-*b*-PMMA) block copolymer with two different block length P4206 (44000-*b*-1200-*b*-45000) and P4205 (43000-*b*-1500-*b*-105000) were purchased from Polymer Source, Inc., Canada. Dimethyl formamide (DMF) acetonitrile, dimethylacetamide (DMAc), acetone, and tetrahydarafuran (THF) were purchased from Sigma Aldrich.

6.2.2 Membrane Preparation

Nanostructured membranes were mostly cast from polymer solutions containing 18 wt % PS-*b*-PAnMMA-*b*-PMMA block copolymer. The block copolymers with different solvent systems were stirred at room temperature for 24 h, before forming the nanostructured membranes. Then the block copolymer solutions were cast on a glass plate using a casting knife with 200 μm air gap. The solvent was allowed to evaporate for different time intervals and the films were immersed in de-ionized water at room temperature.

6.2.3 Field Emission Scanning Electron Microscopy (FESEM)

The surfaces of the membranes were imaged using FEI Quanta 600 Field Emission Scanning Electron Microscope. Imaging was carried out at 5 kV with a working distance of 10 mm. Then the membrane samples were sputter coated with 3nm iridium under argon

atmosphere and the membrane samples were mounted on aluminum stubs using aluminum tape.

6.2.4 Atomic Force Microscopy (AFM)

AFM analysis was performed using an Agilent microscope (Model 5400) in tapping mode. The tip was used with spring constant 3 Nm^{-1}, resonant frequency 76-263 kHz. Block copolymer membranes were imaged after drying.

6.2.5 Transmission Electron Microscopy (TEM)

The membrane crossection was examined using TEM. Images were obtained on a Tecnai 12 (FEI) operating at 120 keV. The membranes were embedded in a low-viscosity epoxy resin (Agar R1165) and cured at 60ºC for 24 h. Ultrathin sections (80 nm) were prepared with an ultramicrotome (Leica EM UC6) and placed on a carbon-coated copper grid. Membrane samples were exposed to RuO_4 vapors, which preferentially stain the aromatic blocks of the membrane before imaging. RuO_4 was prepared by the following procedure. [29] Sodium periodate (1.28 g) was dissolved in 100 ml of deionized water (25° C) and cooled to 1°C. Hydrated ruthenium dioxide (0.6g) was then added to the chilled aqueous solution of $NaIO_4$. As $RuO_2.xH_2O$ began to dissolve, golden yellow RuO_4 was formed.

6.2.6 Water Flux and Retention Measurement

The membranes were kept in water after manufacture. Pure water flux was measured using an Amicon dead end cell at 1 bar N_2 pressure. Membranes were cut into circular samples of about $5cm^2$. Before irradiation the membrane water flux was measured and then the wet membrane was kept in water bath and irradiated in the UV light (8 watt at a distance of 72 mm) at 365 nm for 24h. After irradiation the membrane water flux was measured again.

Then the irradiation procedure was repeated at 254 nm for 6h and the water flux was again determined. The permeance was calculated by using the following equation 1

$$J = \frac{v}{a.t.\Delta P} \qquad (1)$$

where *v* and *t* are the volume of the permeate and time to collect it respectively; *a* is the effective membrane area; ΔP is the transmembrane pressure. Afterward the feed solution was replaced by 1 mg/ml of bovine serum albumin solution to conduct protein filtration test. Then the membranes were washed with water and the γ-globulin solution was filtered. The rejection ratio R was calculated by using the following equation 2

$$R = \left(1 - \frac{C_p}{C_f}\right) * 100 \qquad (2)$$

where c_p and c_f are the protein concentrations of the permeate solutions and the bulk solutions in the feed side respectively. The concentration was determined by UV visible spectrophotometer (Shimadzu, UV 2550) at 278 nm.

6.2.7 Fluorescence measurement

Fluorescence micrographs of the nanostructured film were captured using epifluorescence optical microscope (Olympus B X61) with a filter at 495/520 nm. Photodimerization was carried out for the block copolymer membranes obtained by phase inversion method. The membranes were kept in water and irradiated upon UV lamp at λ= 365 nm for 24 h and then dried the membranes for fluorescence measurements. Fluorescence measurements for the solid film were carried out using a Cary Eclipse fluorescence spectrophotometer (FL0910M008) at the ambient temperature. The same procedure was repeated for the membranes irradiated at λ= 254 nm. For all measurements, the films were excited at λ_{ex}=

370 nm and their corresponding emission wavelength was monitored from λ_{ex}= 370 nm. Both excitation and emission slit width were 2.5 nm for all measurement.

6.3 Results and Discussion

6.3.1 Nanostructured membrane formation

PS-*b*-PAnMMA-*b*-PMMA triblock copolymer having two different molecular weights such as PS_{44K}-*b*-$PAnMMA_{1.2K}$-*b*-$PMMA_{45K}$ and PS_{43K}-*b*-$PAnMMA_{1.5K}$-*b*-$PMMA_{105K}$ were used for the preparation of nanostructured membranes by SNIPS. The key steps are (i) the self-assembly of block copolymers in solution prior to the membrane formation (ii) partial evaporation after casting the block copolymer solution on a substrate (a glass plate in this work) and (iii) immersion of the casting solution in a non-solvent (water in this case). The manufacture of highly ordered nanoporous membranes has been previously demonstrated by using the following block copolymers: PS-*b*-P_4VP,[17] PS-b-PEO,[30] PI-*b*-PS-*b*-PVP[19]. Here for the first time we used PS-*b*-PAnMMA-*b*-PMMA triblock copolymer for the preparation of self-assembled nanostructured membranes. The block copolymer micelle formation in selective solvent or solvent composition mainly determines the final membrane morphology. To attain a desirable morphology, the block copolymer micelle size and structure must be tuned by choosing appropriate solvents suitable for selective interaction with the copolymer blocks. This was also considered here for PS-*b*-PAnMMA-*b*-PMMA. The membrane casting solution contained 18 wt% of PS-*b*-PAnMMA-*b*-PMMA copolymer in different solvent mixture and was stirred for 24hr at 25^{o}C. The self-assembled copolymer solution was cast on glass, partially evaporated for a few seconds and immersed in water. Solvent-non-solvent exchange is immediately takes place leading to structure

immobilization and pore formation as discussed below. Then, the membrane was kept in water for 12h, and for characterization the membranes were removed from the water and air-dried. The membrane morphology was analyzed by FESEM, AFM and TEM. The effects of solvent, block copolymer length and evaporation conditions on the final membrane morphology are discussed below

6.3.2 Membrane Morphology

Figure 6.1 compares FESEM images of PS_{44K}-*b*-$PAnMMA_{1.2K}$-*b*-$PMMA_{45K}$ triblock copolymer membranes prepared by SNIPS, obtained with the same copolymer concentration (18 wt%) and different solvents or solvent mixtures. The solvents were chosen based on the Hansen solublility parameters given in Table 1. The solvents used to prepare the block copolymer solution are miscible with water to enable an effective solvent exchange and consequent phase separation to consolidate the pore formation. Figure 6.1a shows the FESEM images of triblock copolymer membranes prepared using single solvents: DMAc, THF and acetone. The solvents chosen here have solubility parameters (δ) values overall close to those of PS and PMMA blocks. By analyzing the individual contributions, particularly in terms of polarity and hydrogen bonds, all solvents are slightly better for the PMMA block than for PS. The FESEM images for membranes prepared using single solvents did not show any ordered morphology. This might indicates that the single solvents are not leading to a pronounced ordered self-assembly in solution. We previously recognized that even when micelles are formed but swollen are highly swollen by the solvent medium, they could be easily deformed and not lead to membranes with ordered porous structure. THF solubility parameters do not clearly favor one of the blocks and might not even stimulate micelle formation, leading to a surface without visible

morphological features. Acetone is the one with the most distinguished interaction with each block, being more favorable for PMMA, but no order was observed either. Figure 6.2 shows TEM images of micelles formed in diluted solutions in each of the single solvents. It is clearly seen that THF does not favor the formation of regular micelles. Only swollen aggregates could be observed. Acetone is the solvent with best-structured micelles, which are interconnected in arrays.

Table 6.1 Hansen solubility parameters for polymer and solvents

	δ_D	δ_P	δ_H	$\delta = (\delta_D^2+\delta_P^2+\delta_H^2)^{1/2}$
PS	18.6	1.0	4.1	19.1
PMMA	18.6	10.5	7.5	22.6
Water	15.6	16.0	42.3	47.8
DMAc	16.8	11.5	10.2	22.3
Acetone	15.5	10.4	7.0	19.9
THF	16.8	5.7	8.0	19.5
Acetonitrile	15.3	18.0	6.1	24.4

δD : Dispersion forces (van der Waals), δP: Polarity and δH: hydrogen bonding

Figure 6.1b shows the morphology obtained when binary solvents, DMAc/Acetone, DMAc/THF or THF/Acetone, are used. Some indication of lamellar morphology is seen for DMAc/THF. Globular structures are seen for DMAc/Acetone, without preferential order. DMAc/Acetone is probably the most selective combination, which might promote micelle formation with PS cores, but this is not enough to lead to regular surface morphology. When we used a ternary solvent mixture the membrane surface was highly

ordered with a lamellar structure or cylinders parallel to the surface. In opposite to most work we reported before on SNIPS membranes, this system is not expected to form crew cut micelles, since the predominant blocks are almost equal in length.

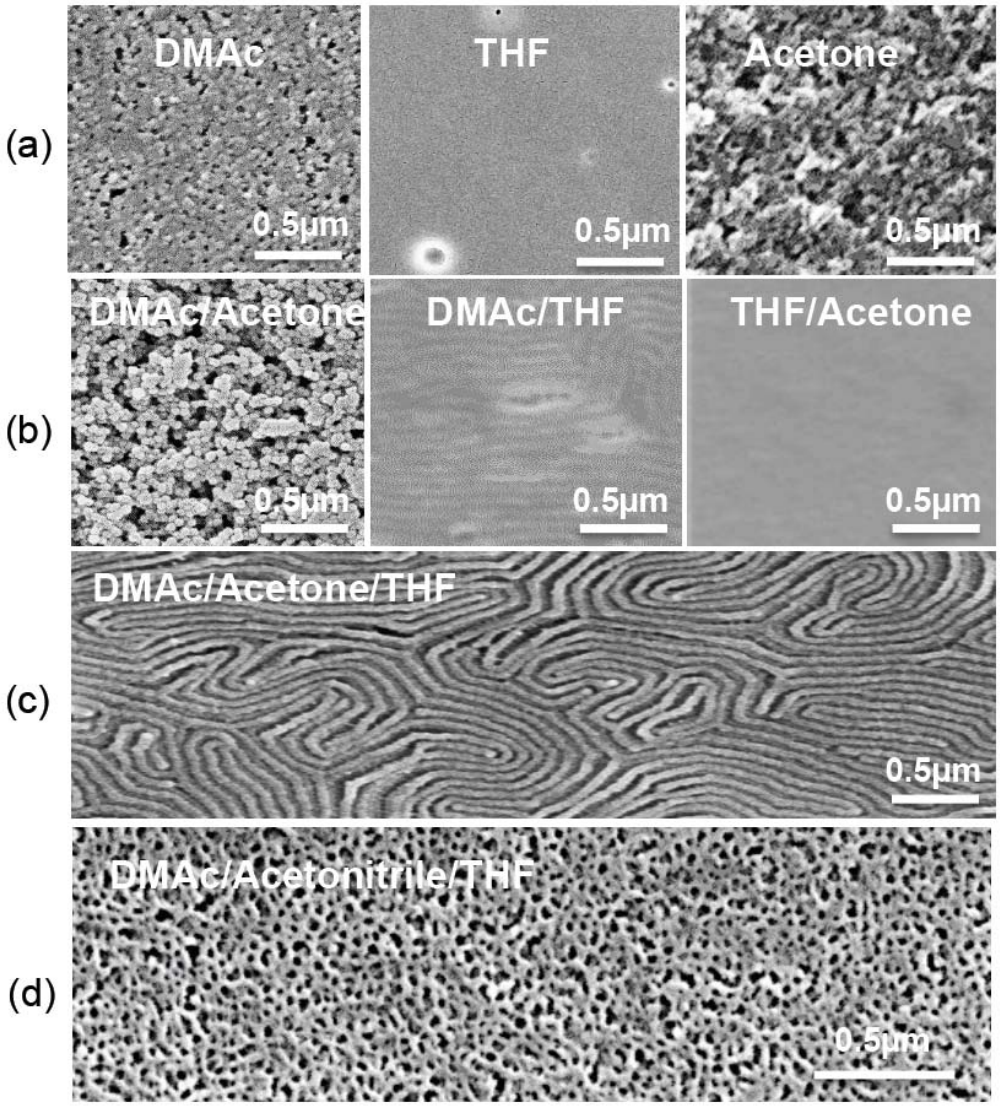

Figure 6.1 FESEM images of membranes surfaces cast from 18 wt% PS_{44K}-b-$PAnMMA_{1.2K}$-b-$PMMA_{45K}$ copolymer solutions in (a) DMAc, THF or Acetone; (b) 1/1 DMAc/Acetone, DMAc/THF or THF/Acetone; (c) 35/29/18 wt% DMAc/Acetone/THF with 10s evaporation time; (d) 35/29/18 wt% DMAc/Acetonitrile/THF with 20s evaporation time.

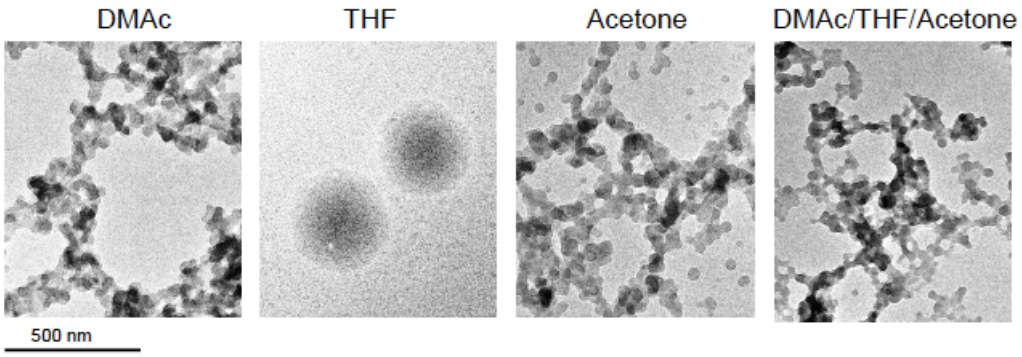

Figure 6.2 TEM images of PS_{44K}-b-$PAnMMA_{1.2K}$-b-$PMMA_{45K}$ diluted solutions in DMAc, THF and acetone as single solvents and a mixture of them with 35/29/18 wt% ratio.

The ternary solvent is expected to have a more favorable interaction with the PMMA block, which would be exposed as corona if cylinders are formed. Micelles formed in diluted solutions in the ternary solvent are more compact than in the single solvents. They are spherical, well-formed and interconnected forming strings. The ternary solvent system was then cast and subjected to different evaporation times before immersion in water. Figure 6.3 shows the results for evaporation times from 5 to 40s. No order is seen with 5s evaporation, whereas from 10 to 30s very ordered lamellae or cylinders are formed. Longer evaporation apparently starts to lead to less order. The boiling points of acetone, THF and DMAc, increase from 56, 66 to 165°C. Even short evaporation would lead to enrichment of DMAc in the cast solution, which is better for PMMA. We need to point out that solvent-block interaction in the bulk is important, but is not the only factor driving the morphology of the membrane top layer. Solution-air (or vapor) interfacial tension, the surface energy of each block and the block-block segregation strength are as relevant. The balance

between all these factors is sensitive and an ideal morphology control or prediction is challenging.

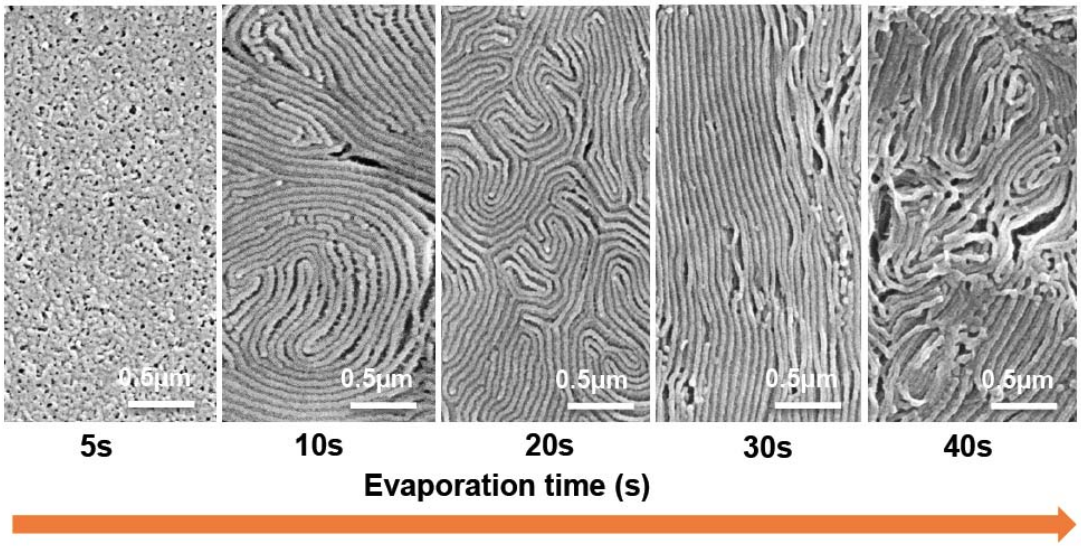

Figure 6.3 FESEM images of membranes surfaces cast from 18 wt % PS_{44K}-*b*-$PAnMMA_{1.2K}$-*b*-$PMMA_{45K}$ copolymer solution in 35/29/18 wt% DMAc/Acetone/THF with different evaporation times.

Blocks with lower surface energy tend to come to the surface, leading to preferential wetting. When cylindrical assemblies are formed in the bulk, they oft lay parallel to the surface instead of orthogonally. Changes in cylinders orientation can be promoted by exposing the solution to different vapors, a procedure, which affects the interfacial energy at the air/film interface. If the surface energies of the constituting blocks are not strongly different the largest block might tend to accumulate on the surface and an entropic balance will guide the placement of the smaller block. This might not only change cylinders orientation, but also change the predominant morphology from cylinders to lamellae or cylinders to perforated lamellae. Solvent annealing has been a successful tool to control

morphology, particularly in thin films. Approaches explored by different groups have been recently revised by Hamley[32] and Albert [33].

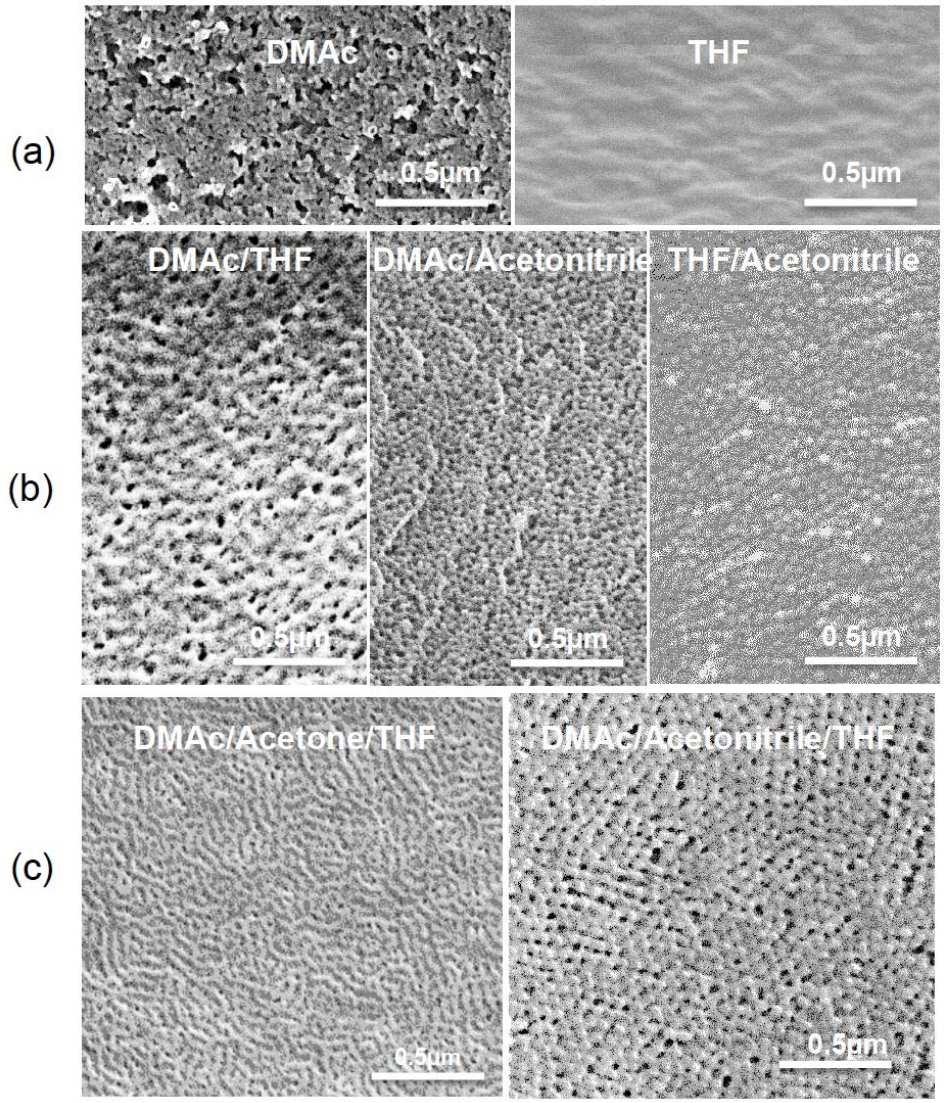

Figure 6.4 FESEM images of membranes surfaces cast from 18 wt% PS_{43K}-*b*-$PAnMMA_{1.5K}$-*b*-$PMMA_{105K}$ copolymer solutions in (a) DMAc or THF; (b) 1/1 DMAc/THF, DMAc/Acetonitrile or THF/Acetonitrile; (c, right) 35/29/18 DMAc/Acetonitrile/THF with 20s evaporation time and (c, left) DMAc/Acetone/THF with 10s evaporation time.

When solid thin films are annealed, the solvent plays an important role increasing the polymer mobility, kinetically enabling an energetically favorable transition. In our case we have morphology control in solution and mobility is already much higher than in a solid film. The solvent has the role of affecting the thermodynamically driven self-assembly in the bulk and the solution-air (vapor) interfacial energy. When immersed in water the previously driven morphology is kinetically trapped, with a fast sequence of solvent-water exchange, phase separation and vitrification, which stabilizes non-equilibrium morphologies. Changing the block length should affect the entropic constrains of block assembly organization on the surface. In order to investigate the effect of block length we kept the ternary solvent system (35/29/18 wt% DMAc/Acetone/THF), polymer concentration (18 wt%) and other optimized casting conditions, using now a copolymer with the double length of PMMA block: PS_{43K}-*b*-$PAnMMA_{1.5K}$-*b*-$PMMA_{105K}$.

From Figure 6.1c,d and 6.4c we can compare the morphologies of membranes cast from the two copolymers solutions under similar conditions using ternary solvent mixtures. While the lamellae or surface-aligned cylinders are clearly seen for the copolymer with shorter PMMA block in DMAc/Acetone/THF (Figure 6.1c), a different morphology is observed with the longer PMMA block in the same solvent mixture (Figure 6.4c, left). This indicates that the cylindrical/lamellar morphology is not the most favored in the bulk anymore or if present, the cylinder alignment on the surface is less thermodynamically favored.

We then replaced acetone by acetonitrile in the ternary solvent mixture for PS_{43K}-*b*-$PAnMMA_{1.5K}$-*b*-$PMMA_{105K}$ (higher PMMA content). Acetonitrile is a much more polar solvent. Spherical and very regular pores with hexagonal order were obtained with 20s

evaporation time, which was the best-optimized condition, as shown in Figure 6.4c. Single solvents and binary solvent mixtures were also investigated for PS_{43K}-*b*-$PAnMMA_{1.5K}$-*b*-$PMMA_{105K}$. The copolymer was not soluble in acetonitrile alone; the morphologies obtained for single and binary systems are also shown in Figure 6.4, confirming that ternary solvent is the most convenient one.

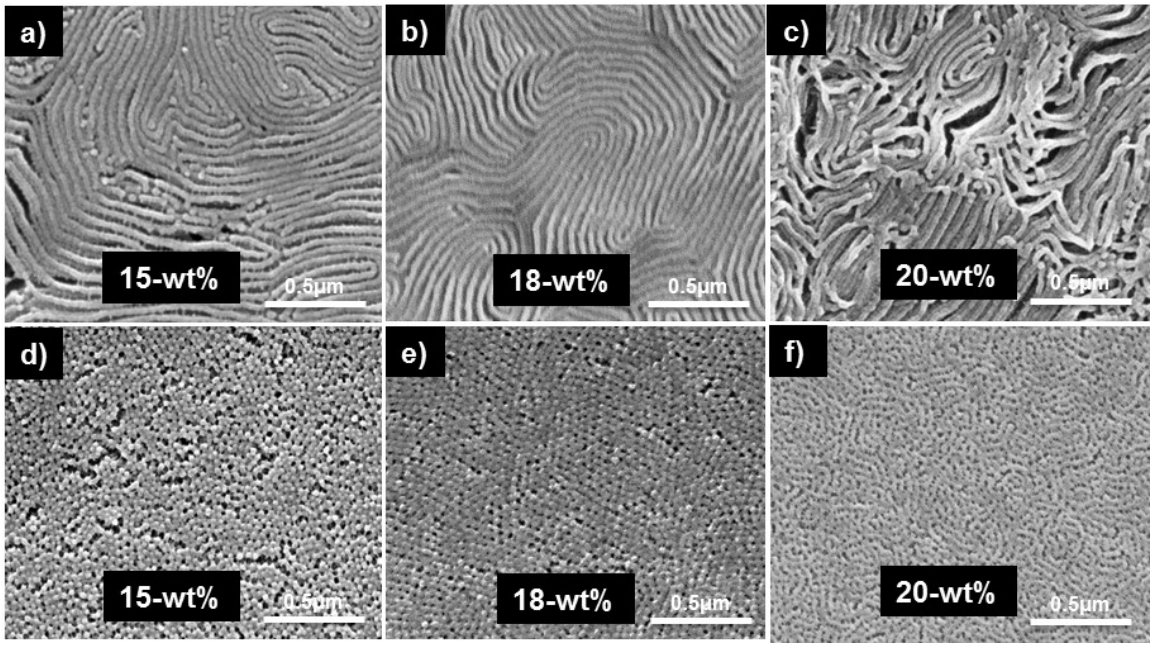

Figure 6.5: SEM images of membranes; a-c) PS_{44K}-b-$PAnMMA_{1.2K}$-b-$PMMA_{45K}$, DMAc-Acetone-THF at 10s evaporation time, and d-f) PS_{43K}-b-$PAnMMA_{1.5K}$-b-$PMMA_{105K}$, DMAc-Acetonitrile-THF at 20s evaporation time

Figure 6.1d shows the morphology of a PS_{44K}-*b*-$PAnMMA_{1.2K}$-*b*-$PMMA_{45K}$ triblock copolymer membrane cast from solution in DMAc/Acetonitrile/THF with 20s evaporation time. A highly porous structure was obtained but with low order than for the higher molecular weight copolymer in analogous conditions. Furthermore, we investigated the effect of polymer concentration on the selective ternary solvents. Only the polymer concentration was changed from 15 wt% to 20 wt% by maintaining the same solvent

systems as shown in Figure 6.5. Change in the polymer concentration for both polymers led to slightly less order. 18 wt% was the best-optimized concentration for both systems.

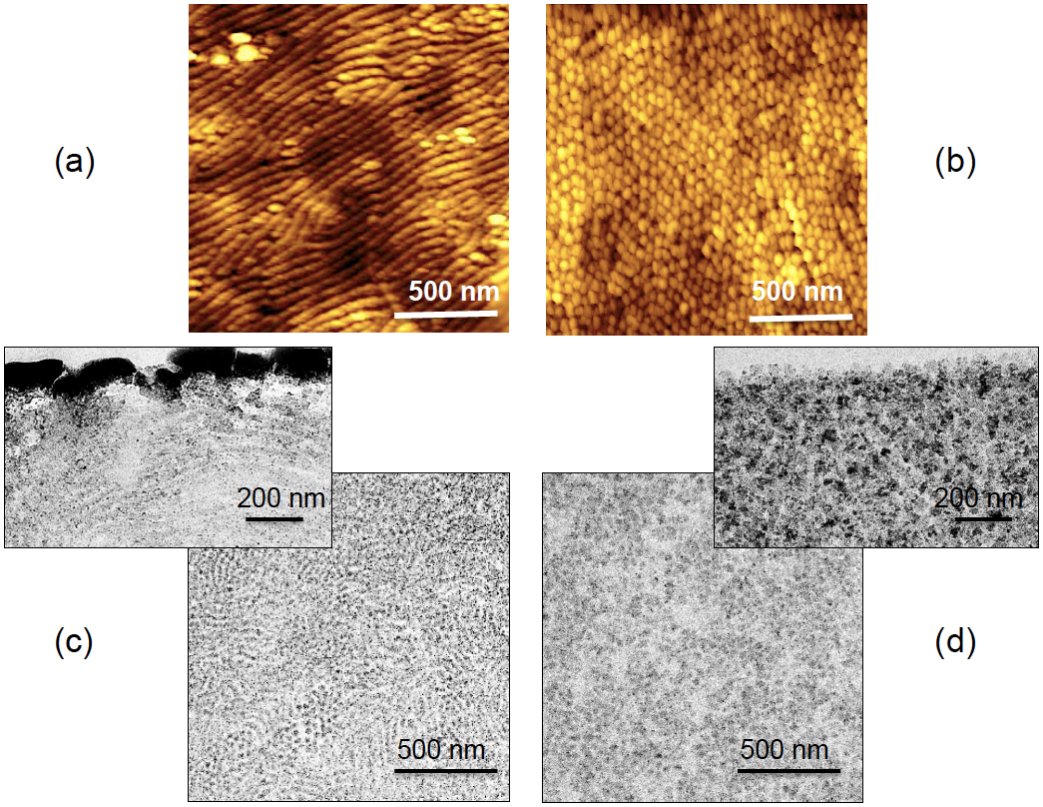

Figure 6.6 (a, b) Surface AFM images and (c, d) Cross-section TEM images of (a, c) PS_{43K}-*b*-$PAnMMA_{1.5K}$-*b*-$PMMA_{45K}$ and (b, d) PS_{44K}-*b*-$PAnMMA_{1.2K}$-*b*-$PMMA_{105K}$ membranes: images of the top layers immediately close to the surface and at deeper locations.

Figure 6.6 shows the surfaces of the best-optimized membranes imaged by AFM and the TEM cross section images of the corresponding membranes. This confirms the ordered surface structures previously observed by FESEM. The cross sections for PS_{44K}-*b*-$PAnMMA_{1.2K}$-*b*-$PMMA_{45K}$ membranes prepared from solution in DMAc/Acetone/THF show that cylinders lay parallel to the surface on the top layer. At positions far from the

surface a mixture of elongated structures and spherical assemblies is observed, indicating that cylinders (and not lamellae) are the predominant assembly geometry. For the PS_{43K}-*b*-$PAnMMA_{1.5K}$-b-$PMMA_{105K}$ membrane cast from solution in DMAc/Acetonitrile/THF spherical micelles are seen not only close to the surface but overall in the membrane structure. RuO_4 preferentially stains the blocks with aromatic rings, in this case PS and the short anthracene-containing blocks, which are probably forming the core.

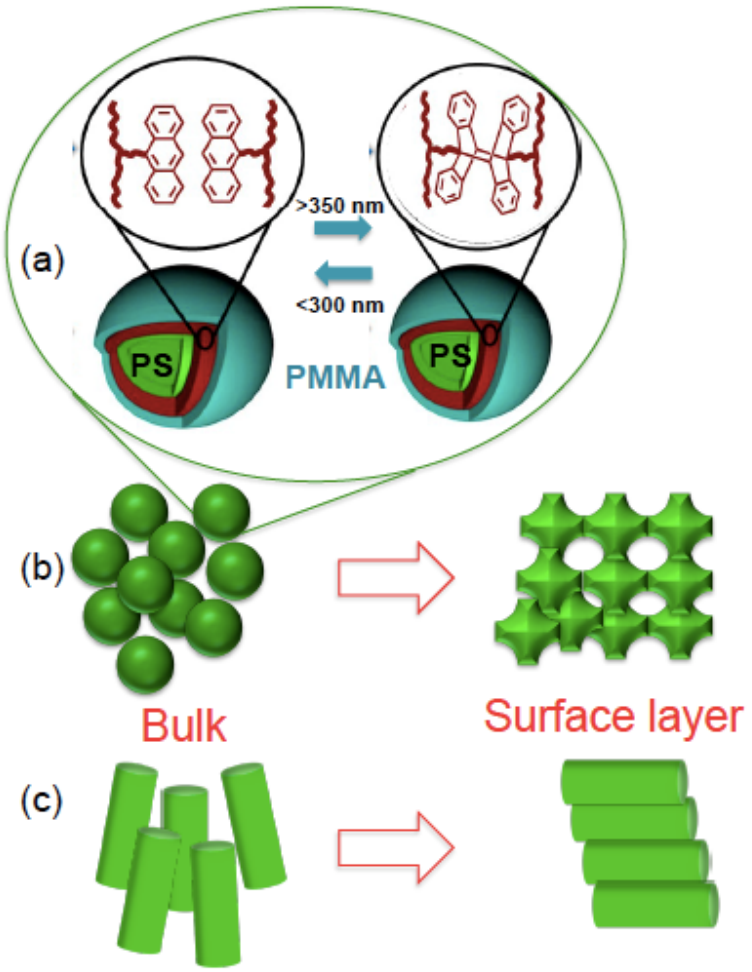

Figure 6.7 Self-assembly of PS-*b*-PAnMMA-*b*-PMMA copolymers: (a) anthracene block dimerization under irradiation; (b, c) organization from solution bulk to membrane surface as (b) spherical and (c) cylindrical micelles.

We have long recognized the importance of the micelle formation in solution to obtain a membrane with ordered isopores in hexagonal arrangement. [16] Additionally we believe that surface effects, analogous to what Scriven [34] proposed for microemulsions would contribute for the final surface structure formation. He claimed that structures with constant mean curvature could evolve from close packing of spheres, as shown in Figure 6.6, could prevail at least as metastable state if the right balance of surface energy and bulk arrangement and interactions are available. Periodic morphologies in block copolymers are strongly influenced by a competition between interface curvature and chain-packing conformation. [35]

A periodic morphology, which could be related to membrane formation using the high molecular weight copolymer, is perforated lamellae. [36-39] In copolymer systems with strong segregation this morphology is not favored, but surface interactions and solvent-blocks interactions could contribute for its occurrence. They are more frequent in thin films, which have large ratio of surface area to volume. Immersion in a non-solvent bath (water), in the final step of membranes preparation, induces immediate solvent exchange and kinetically trap even metastable morphologies. We believe that the final membrane surface morphology results from the interplay of assembly geometry and arrangement in the bulk, guided by the solvent block-block and solvent-block interaction, and the surface energy, which is also influenced by copolymer and solvent composition as well as by the curvature of the incipient assemblies on the surface. As depicted in Figure 6.7, the system with lower PMMA molecular weight probably assembles as micelle strings merged to cylinders already in solution. Higher PMMA molecular weight in ternary solvent favors spherical micelles, which are separated in the bulk and merge only after casting to form a periodic

structure driven by a complex balance of factors related to enthalpic interactions, entropic constrains, assembly curvature and surface energy.

6.3.3 Fluorescence and Photodimerization of membranes

Anthracene is a polycyclic aromatic hydrocarbon, which undergoes photodimerization on exposure to light or heat and is also able to emit fluorescence emission if properly excited.

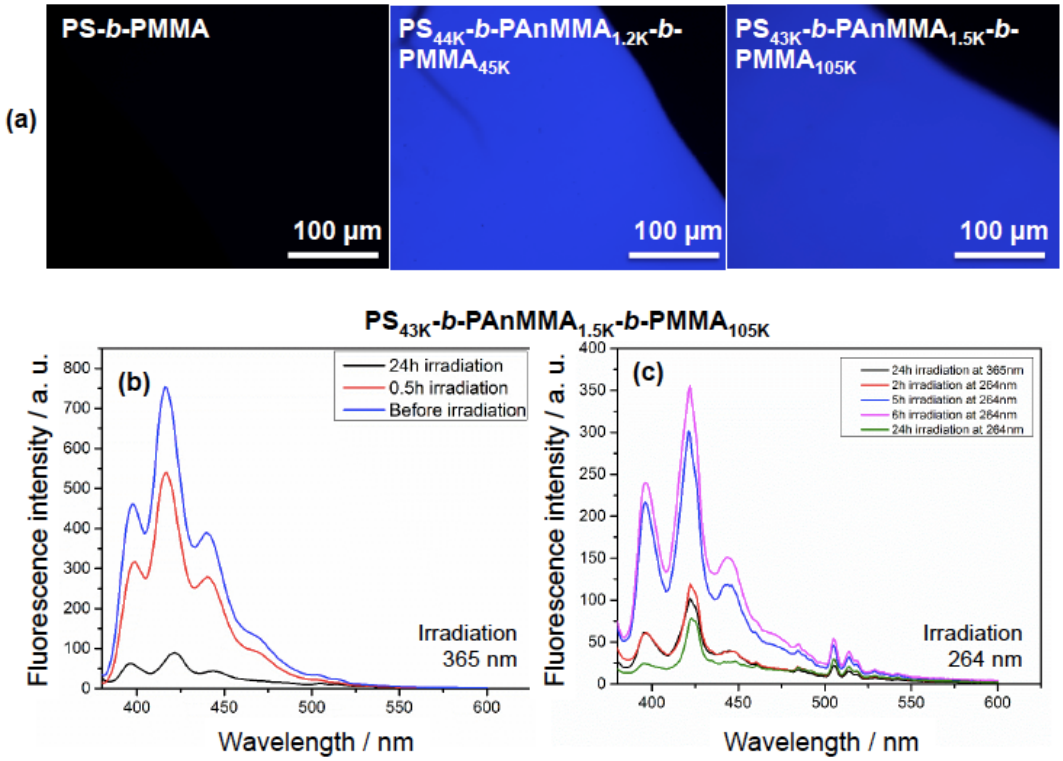

Figure 6.8 (a) Fluorescence micrograph of PS-*b*-PMMA, PS_{44K}-*b*-$PAnMMA_{1.2K}$-*b*-$PMMA_{45K}$ and PS_{43K}-*b*-$PAnMMA_{1.5K}$-*b*-$PMMA_{105K}$ membranes; (b, c) Fluorescence spectra of PS_{43K}-*b*-$PAnMMA_{1.5K}$-*b*-$PMMA_{105K}$ membranes with (b) 365 nm and (c) 264 nm irradiation.

Here in this work, the membranes were prepared by triblock copolymers containing anthracene moiety as one of the mid-block between PS and PMMA. Anthracene moieties attached to various polymers had excellent fluorescent properties [27-28, 40]. In this paper the

copolymer containing anthracene was chosen because of the possibility of fluorescence emission. To demonstrate this behavior, the membranes were imaged using a fluorescence microscope. Figure 6.8 shows the fluorescence micrographs of PS_{160K}-*b*-$PMMA_{160K}$ (no anthracene moiety), PS_{44K}-*b*-$PAnMMA_{1.2K}$-*b*-$PMMA_{45K}$, and PS_{43K}-*b*-$PAnMMA_{1.5K}$-*b*-$PMMA_{105K}$ membranes, prepared by phase inversion. The fluorescence micrographs of PS-*b*-PMMA did not show any blue emission because there is no fluorescent group. The other two images show homogeneous blue emission due to the fluorescence of anthracene present in the block copolymer.

In addition to the fluorescent properties of anthracene, it is well known that anthracene and its derivatives undergoes photochemical dimerization upon long wave length UV irradiation (>350 nm) to give [4+4] cycloadducts across the 9,10 positions of anthracene (Figure 6.7a). The dimerization reaction is reversible and the photodimers can be dissociated into the monomers after heating or further visible light irradiation. Photodimerization occurs both in solid and liquid state. It is obviously faster in liquid state and is highly dependent on the relative position and orientation of the monomers. [41] To trigger the dimerization we carried out the photodimerization reaction upon irradiating with UV light at 365nm. To carry out photodimerization the block copolymer membranes were kept in water and directly exposed to UV lamp at 365nm. Figure 6.8b and 6.8c show the fluorescence spectra obtained for PS_{43K}-*b*-$PAnMMA_{1.5K}$-*b*-$PMMA_{105K}$ at various irradiation times and their reversible switching behavior. The distinct fluorescence bands for anthracene have peaks at about 385, 405, 420 and 445 nm. After irradiation for 0.5 h at 365 nm the anthracene moiety present in the block copolymer converted into [4+4] cycloadducts and their intensity decreased to half compared to the original membrane. This

clearly shows that the photodimerization was fast even in the solid state. On further irradiation during 24 h at 365 nm the intensity completely reduced, confirming maximum dimerization. The dimerization process could be either intermolecular or intramolecular. The main requirement is that the anthracene groups should be in close proximity to react. To investigate the reversibility of the dimerization, the dimerized membranes were then irradiated with light at 254 nm. The reversible reaction (i.e., the conversion of cycloadduct to anthracene moiety) occurred after 2 h of irradiation at 264 nm. The conversion of cycloadduct to anthracene was maximum at 6 h of irradiation and further irradiation (24 h at 264 nm) led again to formation of cyloadduct. It was observed from Figure 6.8, that the reversible reaction occurred after 5 or 6 h of irradiation and the conversion was only 50 % achieved compared to the original non irradiated membrane, indicating that the anthracene moiety was not fully recovered on irradiation at 264nm.

6.3.4 Photoresponsive water flux

On irradiation the dimer formation and reaction reversibility indicates that there are conformational changes of the anthracene block in the membranes. We anticipated that these changes could affect also permeability and selectivity. Therefore, to investigate the light responsive behavior of this membrane the water flux and protein retention measurements were carried out for the irradiated and non-irradiated membranes. The water flux (Figure 6.9) for the PS_{44K}-*b*-$PAnMMA_{1.2K}$-*b*-$PMMA_{45K}$ membrane was 270 L m^{-2} h^{-1} bar^{-1} and for the PS_{43K}-*b*-$PAnMMA_{1.5K}$-*b*-$PMMA_{105K}$ membrane was 310 L m^{-2} h^{-1} bar^{-1}. The membranes irradiated for 24h at 365nm showed a decrease in water flux. This was observed for both copolymers. The water flux for the photodimerized membrane went down to 230 L m^{-2} h^{-1} bar^{-1} for PS_{44K}-*b*-$PAnMMA_{1.2K}$-*b*-$PMMA_{45K}$ and 250 L m^{-2} h^{-1} bar^{-1}

for PS_{43K}-*b*-$PAnMMA_{1.5K}$-*b*-$PMMA_{105K}$. The flux decline indicates that conformational changes affected the pore size. When the dimerization reaction takes place between different chains (Scheme 6a), it induces a slight membrane shrinkage and pore reduction. To check the reversibility, the photodimerized membranes were than irradiated at 264 nm for 6 h. The water flux recovery to 250 L m^{-2} h^{-1} bar^{-1} for PS_{44K}-*b*-$PAnMMA_{1.2K}$-*b*-$PMMA_{45K}$ and 280 L m^{-2} h^{-1} bar^{-1} for PS_{43K}-*b*-$PAnMMA_{1.5K}$-*b*-$PMMA_{105K}$, after 264 nm irradiation.

The membrane retention was measured using two different model proteins, Bovine Serum Albumin (BSA 66 kg/mol) and γ-globulin (IgG, 150 kg/mol). The rejection measurements were carried out and the concentrations of proteins were measured using UV visible spectroscopy. Both membranes (Figure 6.9) had more than 95% rejection of γ-globulin and the BSA rejection was 70% and 62% respectively. On irradiation at 365nm for 24h the membranes had slight increase of the BSA retention to 75% (low molecular weight) and 68% (high molecular weight). After reversible irradiation at 264 nm for 6 h similar BSA retention was observed.

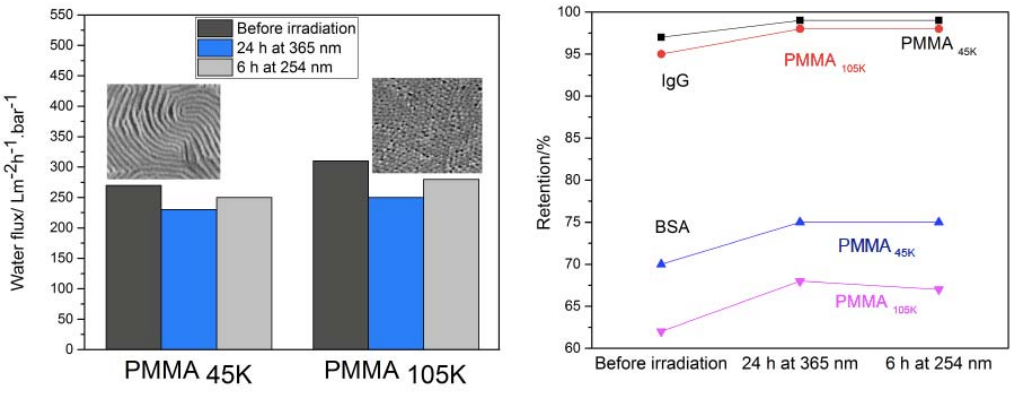

Figure 6.9 Water flux and retention measurements

A significant chemical change in the anthracene block was observed from the fluorescence spectra, however, the membrane flux and retention properties were not dramatically altered in response to light. We hypothesis that the photodimerization occurred in the inner middle core of the micelle sphere and the amount of anthracene group present in block copolymer membrane is high to close completely the pores. Larger blocks would be more effective but are currently not commercially available. By increasing the anthracene content and preparing the anthracene as end block in the block copolymer membrane larger effect in the membranes properties on irradiation with light is expected.

6.4 REFERENCES

1. Darvishmanesh, S.; Qian, X.; Wickramasinghe, S. R., *Curr. Opin. Chem. Eng.* 2015, *8*, 98-104.

2. Nicoletta, F. P.; Cupelli, D.; Formoso, P.; De Filpo, G.; Colella, V.; Gugliuzza, A., *Membranes* 2012, *2*, 134-197.

3. Lue, S. J.; Hsu, J.-J.; Chen, C.-H.; Chen, B.-C., *J. Membr. Sci.* 2007, *301*, 142-150.

4. Yang, Q.; Himstedt, H. H.; Ulbricht, M.; Qian, X.; Wickramasinghe, S. R., *J. Membr. Sci.* 2013, *430*, 70-78.

5. Baumann, L.; Schöller, K.; de Courten, D.; Marti, D.; Frenz, M.; Wolf, M.; Rossi, R. M.; Scherer, L. J. *RSC Advances* 2013, *3*, 23317-23326.

6. Wandera, D.; Wickramasinghe, S. R.; Husson, S. M., *J. Membr. Sci.* 2010, *357*, 6-35.

7. Liu, Z.; Wang, W.; Xie, R.; Ju, X.-J.; Chu, L.-Y., *Chem. Soc. Rev.* 2016.

8. Zhao, C.; Nie, S.; Tang, M.; Sun, S. *Prog. Polym. Sci.* 2011, *36*, 1499-1520.

9. Himstedt, H. H.; Du, H.; Marshall, K. M.; Wickramasinghe, S. R.; Qian, X., *Ind. Eng. Chem. Res.* 2013, *52*, 9259-9269.

10. Liu, N.; Dunphy, D. R.; Atanassov, P.; Bunge, S. D.; Chen, Z.; López, G. P.; Boyle, T. J.; Brinker, C. J. *Nano Lett.* 2004, *4*, 551-554.

11. Chu, L. Y.; Li, Y.; Zhu, J. H.; Chen, W. M., *Angew. Chem. Int. Ed.* 2005, *44*, 2124-2127.

12. He, D.; Susanto, H.; Ulbricht, M. *Prog. Polym. Sci.* 2009, *34*, 62-98.

13. Chu, L.-Y.; Li, Y.; Zhu, J.-H.; Wang, H.-D.; Liang, Y.-J. *J. Controlled Release* 2004, *97*, 43-53.

14. Peinemann, K.-V.; Abetz, V.; Simon, P. F., *Nat. Mater.* 2007, *6*, 992-996.

15. Nunes, S. P.; Karunakaran, M.; Pradeep, N.; Behzad, A. R.; Hooghan, B.; Sougrat, R.; He, H.; Peinemann, K.-V. *Langmuir* 2011, *27*, 10184-10190.

16. Nunes, S. P.; Behzad, A. R.; Hooghan, B.; Sougrat, R.; Karunakaran, M.; Pradeep, N.; Vainio, U.; Peinemann, K.-V. *ACS Nano* 2011, *5*, 3516-3522.

17. Schacher, F.; Ulbricht, M.; Müller, A. H., *Adv. Funct. Mater.* 2009, *19*, 1040-1045.

18. Phillip, W. A.; Mika Dorin, R.; Werner, J. r.; Hoek, E. M.; Wiesner, U.; *Nano Lett.* 2011, *11*, 2892-2900.

19. Shevate, R.; Karunakaran, M.; Kumar, M.; Peinemann, K.-V. *J. Membr. Sci.* 2016, *501*, 161-168.

20. Kim, Y.; Kwon, S.; Yoo, D.; Rubner, M. F.; Wrighton, M. S., *Chem. Mater.* 1997, *9*, 2699-2701.

21. Nakabayashi, K.; Inoue, S.; Abiko, Y.; Mori, H. *Macromolecules* 2013, *46*, 4790-4798.

22. Zhang, H.; Verboom, W.; Reinhoudt, D. N., 9-(Guanidinomethyl)-10-Vinylanthracene: *Tetrahedron Lett.* 2001, *42*, 4413-4416.

23. Wei, K. S.; Livingston, R., *Photochem. Photobiol.* 1967, *6*, 229-232.

24. Maturi, M. M.; Fukuhara, G.; Tanaka, K.; Kawanami, Y.; Mori, T.; Inoue, Y.; Bach, T., *Chem. Commun.* 2016, *52*, 1032-1035.

25. Breton, G. W.; Vang, X. *J. Chem. Educ.* 1998, *75*, 81.

26. Zheng, Y.; Micic, M.; Mello, S. V.; Mabrouki, M.; Andreopoulos, F. M.; Konka, V.; Pham, S. M.; Leblanc, R. M., *Macromolecules* 2002, *35*, 5228-5234.

27. Rameshbabu, K.; Kim, Y.; Kwon, T.; Yoo, J.; Kim, E., *Tetrahedron Lett.* 2007, *48*, 4755-4760.

28. Wang, C.; Zhang, D.; Xiang, J.; Zhu, D., *Langmuir* 2007, *23*, 9195-9200.

29. Trent, J. S. *Macromolecules* 1984, *17*, 2930-2931.

30. Karunakaran, M.; Nunes, S. P.; Qiu, X.; Yu, H.; Peinemann, K.-V. *J. Membr. Sci.* 2014, *453*, 471-477.

31. Hansen, C. M., *Hansen Solubility Parameters: A User's Handbook*. CRC press: 2007.

32. Hamley, I. *Prog. Polym. Sci.* 2009, *34*, 1161-1210.

33. Albert, J. N.; Epps, T. H., *Today* 2010, *13*, 24-33.

34. Scriven, L. *Nature* 1976, *263*, 123-125.

35. Gido, S. P.; Schwark, D. W.; Thomas, E. L.; do Carmo Goncalves, M., *Macromolecules* 1993, *26*, 2636-2640.

36. Knoll, A.; Horvat, A.; Lyakhova, K.; Krausch, G.; Sevink, G.; Zvelindovsky, A.; Magerle, R., *Phys. Rev. Lett.* 2002, *89*, 035501.

37. Knoll, A.; Magerle, R.; Krausch, G., *The Journal of chemical physics* 2004, *120*, 1105-1116.

38. Horvat, A.; Knoll, A.; Krausch, G.; Tsarkova, L.; Lyakhova, K.; Sevink, G.; Zvelindovsky, A.; Magerle, R., *Macromolecules* 2007, *40*, 6930-6939.

39. Ludwigs, S.; Böker, A.; Voronov, A.; Rehse, N.; Magerle, R.; Krausch, G. *Nat. Mater.* 2003, *2*, 744-747.

40. You, J.; Kim, Y.; Kim, E., *Mol. Cryst. Liq. Cryst.* 2010, *520*, 128/[404]-135/[411].

41. Zouev, I.; Cao, D.-K.; Sreevidya, T.; Telzhensky, M.; Botoshansky, M.; Kaftory, M., *CrystEngComm* 2011, *13*, 4376-4381.

CHAPTER 7

Conclusions

The main motivation of this dissertation research is to tune the nanostructure pore morphology of block copolymer membranes in a simpler way using various complexing agents and solvents. We conclude from chapter 2, by a systematic investigation that organic molecules containing mono-, di-, tri- and polyhydroxyl/acids functional groups strongly interact with the pyridine block of PS-*b*-P4VP, leading to morphology diversification and controlled membrane pore size. Hydrogen-bond formation between PS-b-P4VP block copolymer and –OH/ –COOH functionalized organic molecules was used to tune the morphology of asymmetric nanoporous membranes prepared by simultaneous self-assembly and non-solvent induced phase separation. The OH-functionalized organic molecules direct the morphology into hexagonal order. COOH-functionalized molecules led to both lamellar and hexagonal structures. The following series of additives led to pores with hexagonal order with increasing pore size: terephthalic acid (COOH-bifunctionalized) < rutin (OH-multifunctionalized) < 9-anthracenemethanol (OH-monofunctionalized) < 3,5-dihydroxybenzyl alcohol (OH-trifunctionalized). The pore sizes of membranes with hexagonal order increased, in the following series: plain BCP membrane < TPA < Ru < AM < DHBA. The lamellar structured BCP membranes such as PS-b-P4VP (MA) and PS-b-P4VP (Tris) had fluxes of 3000 and 1600 L m^{-2} h^{-1} bar^{-1}. Membranes with hexagonal order had water flux from 600 to 3200 L m^{-2} h^{-1} bar^{-1}. The light scattering data revealed that the sizes of BCP micelles radius formed in solution under the influence of OH group, bearing organic molecules, are around 8 nm. DLS measurements for BCP micelles formed in the presence of COOH-group were up to 3-fold larger than with OH-molecules. The

hydrogen bond formation between organic molecules and pyridine affects the solution viscosity and therefore also the membrane formation and final morphology. We conclude that a small amount of proton-donor organic molecules interferes with the supramolecular assembly of block copolymers in solution and changes the final membrane morphology.

From chapter 3, we conclude that ionic liquids can act as a self-assembly media for tuning the pore morphology of nanostructured block copolymer membranes, produced via self-assembly and water induced phase separation. The effect of ionic liquids on the morphology was investigated, by using polystyrene-b-poly(4-vinyl pyridine) (PS-b-PV4P) diblock as membrane copolymer matrix and imidazolium and pyridinium based ionic liquids. The effect of ionic liquid concentration and chemical composition was evident with particular interaction with P4VP blocks. Non-protic ionic liquids facilitate the formation of hexagonal nanoporous block copolymer structure, while protic ionic liquids led to a lamella-structured membrane. Both substituted pyridinium and imidazolium-based ionic liquids induce hexagonal cylindrical porous morphology. The highly protic ionic liquids preferentially solvate P4VP blocks and direct the micelle ordering during the membrane formation, forming lamellar structure. We observed that the [B3MIM][BF4] solutions had the largest viscosity. Beside the interaction between imidazolium, BF_4 and pyridine the high viscosity was explained by taking in account of steric effects. All the membranes have high water flux, ranging from 450 to 1800 L m^{-2} h^{-1} bar^{-1}. Ionic liquid/ block copolymer membranes having hexagonal pores structure have higher water flux than block copolymer membranes prepared withoutionic liquid. High water flux of these membranes reflects the high porosity. Particularly high order was observed for solutions with [B4MPy][BF4] by cryo microscopy, leading to porous membranes with hexagonal pore

distribution. The [B4MPy][BF4] solution had a strong gel-like behavior. Low water flux was observed for membranes prepared from protic [IM][TFSI]/block copolymer solutions, which have a lamellar structure with strong connection between lamellae. The [IM] [TFSI]/block copolymer membrane with lamellar structure and low porosity, has low water flux compared to other membranes and a molecular weight cut-off of 50 kg/mol with more than 95 % retention of 150 kg/mol polyethylene glycol (PEG). Membranes prepared without ionic liquid rejected 55 wt% of the same molecular weight PEG; membranes with other ionic liquids rejected 61-66 wt% 150 kg/mol PEG.

Furthermore, PS-b-P4VP isoporous membranes were complexed with gold metal ion, and the membrane catalytic activity was tested with the help of the model reaction of reduction of 4-nitrophenol to 4-aminophenol. We deposited gold nanoparticles on the outer hollow fiber surface and demonstrated the catalytic activity of the gold nanoparticle-enhanced hollow fiber membranes by the reduction of nitrophenol to aminophenol.

In chapter 4b we systematically investigated the pore morphology of isoporous PS-b-P4VP using 3D imaging technique. Two microscopy methods for 3D imaging visualization, FIB/FESEM and SBF/SEM, were applied to porous block copolymer membranes. Both methods offered high resolution for adequate pore analysis and covered sample volumes higher than normally possible by transmission electron microscopy tomography. With help of a new algorithm, the set of images obtained by both methods could be analyzed to provide a complete mapping of porosity and average pore size in different membrane layers. The 3D-visualization combining information gained by the image segmentation showed the pore connectivity in different membrane regions. We demonstrate here how effective the method is for asymmetric block copolymer membranes. The same analysis

using the proposed algorithm can be applied for any kind of membranes or porous materials. The imaging method to be chosen depends however on the mechanical properties, feasibility of slicing with diamond knife or ion beam, pore size and volume to be sampled. The method is particularly valuable for asymmetric membranes, which are used in many applications. It can help the development of new systems for forward osmosis and other applications for which not only the porosity of the top selective layer is relevant, but also that of the whole porous substrates.

Silver has a strong biocide activity, which for membranes can bring the advantage of minimizing the growth of bacteria and formation of biofilm. From chapter 5 we conclude silver nanoparticles were grown on the surface and pore walls of PS-b-P4VP block copolymer membranes with highly ordered pore structure. Well-distributed nanoparticles were obtained by promoting pyridine-silver ions interaction, followed by reaction with a reducing agent. It was found that Pyridine blocks constitute the pore surfaces aids in complexing silver ions and promoting a homogeneous distribution during the nanoparticle formation. Nanoparticles were then formed by reduction with sodium borohydride. The morphology varied with the preparation conditions (pH and silver ion concentration). The membranes with nanoparticles prepared under different pH values and ion concentrations were incubated with Pseudomonas aeruginosa and compared with the control. We then investigated the biocidal activity of the silver nanoparticles grown membranes. The strongest biocidal activity was achieved with membranes containing membranes prepared under pH 9. Under these conditions, the best distribution with small particle size was observed by microscopy. Flow cytometry measurements demonstrated that, after 72h incubation of the membrane systems (nanoparticle incorporation at pH 9) with *P.*

aeruginosa, the proportion of viable cells compared to the control (in absence of silver nanoparticles) was around 20 %.

From chapter 6, we conclude that a nanostructured triblock copolymer membranes with photoresponsive behavior were successfully developed by phase inversion. We showed the optimization conditions for the membrane formation by using poly(styrene-b-anthracene methyl methacrylate-b-methylmethacrylate) (PS-*b*-PAnMMA-*b*-PMMA) copolymer and identified the most suitable solvent, copolymer block length, and other parameters. The nanostructured membranes had cylinders parallel to the surface or hexagonally ordered spherical micelles on their top layer. The water flux for the PS_{44K}-*b*-$PAnMMA_{1.2K}$-*b*-$PMMA_{45K}$ membrane was 270 L m^{-2} h^{-1} bar^{-1} and for the PS_{43K}-*b*-$PAnMMA_{1.5K}$-*b*-$PMMA_{105K}$ membrane was 310 L m^{-2} h^{-1} bar^{-1}. Both membranes showed photoresponsive behavior on irradiation with light and their membrane flux and retention properties were altered on irradiating at longer wavelength (365 nm) and shorter wavelength (264 nm) of light. The anthracene moiety present in the PS-*b*-PAnMMA-*b*-PMMA block copolymer membranes, on exposure to UV at 365nm, converted into cyclic adduct in the solid state. Then the cyclic adduct was reversibly disrupted on irradiation with shorter wavelength of light (264 nm). The reversible photoresponsive conformational changes at the molecular level lead to changes in the final membrane flux properties.

Overall, we conclude that small organic molecule additives, ionic liquids and solvent system can be used to control the pore geometry and pore size of membranes from block copolymer via non solvent induced phase separation. We exploited PS-b-P4VP isoporous membranes in catalytic and biocidal applications. A new photo responsive nanostructured membranes were developed and in this work we reported the suitable membrane formation

condition and their photoresponsive behavior. Further work can be explored on the photoresponsive behavior membrane in finding appropriate biomedical application.

LIST OF PUBLICATIONS

1. R.Hilke, N. Pradeep, P.Madhavan ,U. Vainio, Ali Reza Behzad, Rachid Sougrat,Suzana.P. Nunes and Klaus-Viktor Peinemann,Block copolymer Hollow Fiber Membranes with catalytic activity and pH response, *ACS Applied materials and Interfaces*, 2013, 5(15), pp 7001-7006.
2. P.Madhavan, K.V.Peinemann and S.P. Nunes, Complexation Tailored Morphology of Asymmetric Block Copolymer Membranes, *ACS Applied Materials and Interfaces*,2013, 5(15), pp 7152-7159.
3. P. Madhavan, Pei-Ying Hong, Rachid Sougrat and Suzana.P.Nunes, Silver Enhanced Bock copolymer Membranes with Biocidal activity, *ACS Applied Materials and Interfaces* , 2014,6(21), pp 18497-18501.
4. P.Madhavan, Rachid Sougrat, Ali Reza Behzad, Klaus-Viktor Peinemann and Suzana.P.Nunes, Ionic liquids As Self-Assembly Guide for the Formation of Nanostructured Block Copolymer Membranes, *Journal of Membrane Science*, 2015, 498, pp. 568-577
5. Ganesh Sundaramoorthi, Markus Hadwiger, Mohamed Ben-Romdhane, Ali R. Behzad, Poornima Madhavan, and Suzana P. Nunes, 3D Membrane Imaging and Porosity Visualization, *Ind. Eng. Chem. Res.,* 2016, 55 (12), pp 3689–3695.
6. P. Madhavan, R. Sougrat, B. Sutisna and S. P. Nunes, Photoresponsive Nanostructured Membranes, *(Submitted)*